

Modeling the Impact of Structural Deviations in Lithium-Ion Batteries

Zur Erlangung des akademischen Grades eines
Doktors der Ingenieurwissenschaften (Dr.-Ing.)
von der KIT-Fakultät für Elektrotechnik und Informationstechnik des
Karlsruher Instituts für Technologie (KIT)

angenommene
Dissertation
von

Oke Matthias Schmidt, M.Sc.

Tag der mündlichen Prüfung: 19. September 2022
Hauptreferentin: Prof. Dr.-Ing. Ulrike Krewer
Korreferent: Prof. Dr.-Ing. Fridolin Röder

Kurzfassung

Die Lithium-Ionen-Batterie wird heutzutage in der mobilen Kommunikation, der stationären Energiespeicherung sowie der Elektromobilität eingesetzt. Die stark steigende Nachfrage führt zu einem hohen Interesse an der Herstellung und deren Auswirkung auf die Leistungsmerkmale. Es ist notwendig, Produktionsanlagen zu schaffen, die die Nachfrage nach hochwertigen Batterien bedienen können. Dafür ist es erforderlich zu untersuchen, wie sich Abweichungen in den Produkteigenschaften, z. B. von strukturellen Merkmalen, auf die Qualität auswirken. Dies trägt langfristig dazu bei, die Ausschussrate zu reduzieren und damit die Qualität und Nachhaltigkeit zu verbessern.

Im Rahmen der Dissertation wird untersucht, wie sich Unsicherheiten, die in der Produktion entstehen, auf die Elektrodenstruktur und die elektrochemischen Eigenschaften auswirken. Mit Hilfe von mathematischer Modellierung wird analysiert, wie sich verschiedene Arten von Schwankungen über die verketteten Herstellungsprozesse fortpflanzen, entwickeln und die elektrochemischen Eigenschaften der Batterie beeinflussen. Ziel ist es, sensitive Prozesse und Strukturparameter zu identifizieren. Darüber hinaus werden robuste Elektrodenstrukturen identifiziert, die aufgrund ihrer spezifischen Struktur zu geringeren Abweichungen führen.

Im ersten Teil wird untersucht, wie sich Schwankungen in den Produktionsprozessen auf die Leistungsmerkmale von Lithium-Ionen-Batterien auswirken. Um dies zu analysieren, wird eine modellbasierte Beschreibung der Fertigungsprozesse mit einem elektrochemischen Batteriemodell gekoppelt. Das erlaubt die kontinuierliche Beschreibung von Abhängigkeiten zwischen Produktionsprozessen, Elektrodenstruktur und elektrochemischen Eigenschaften. Die dadurch entwickelte Plattform wird in einer Fallstudie angewendet, um zu untersuchen, wie sich Schwankungen in der Elektrodenproduktion ausbreiten und die Leistung beeinflussen. Für die analysierten Szenarien zeigt sich, dass der Beschichtungsprozess den höchsten Einfluss auf die Leistungseigenschaften hat. In diesem Prozess wird die Beladung der Elektroden mit Aktivmaterial eingestellt und damit auch die Leistung der Elektrode beeinflusst. Die Plattform ermöglicht ebenso die Untersuchung von Wechselwirkungen zwischen Produktionsschritten. So kommt es zwischen dem Beschichten und Kalandrieren zu relevanten Wechselwirkungen, da in beiden Prozessen die gleichen Strukturparameter verändert werden. Im Anschluss an die Fallstudie wird untersucht, wie die Elektrodenstruktur angepasst werden muss, damit die Leistungseigenschaften von Kathoden robust gegen Schwankungen in der Struktur reagieren. Es zeigt sich, dass Elektroden mit hoher Schichtdicke und geringer Porosität in Betriebspunkten, in denen der

Massentransport im Elektrolyten der begrenzende Faktor ist, zu hohen Leistungsabweichungen neigen. Durch den Einsatz von robuster Optimierung wird die volumetrische Energiedichte leicht verringert, ohne dass es zu einem limitierenden Massentransport im Elektrolyten kommt. Dadurch wird ein deutliches Absinken der Leistung bei Schwankungen in der Struktur verhindert. Infolgedessen sinkt die Standardabweichung und die Ausschussrate in der Herstellung kann deutlich reduziert werden.

Im zweiten Teil der Arbeit wird die Mikrostruktur der Elektrode untersucht. Der Schwerpunkt liegt auf der Struktur der Leitruß-Binder-Matrix. Trotz gleicher Volumenanteile kann allein eine veränderte Netzwerkstruktur der Matrix zu deutlichen Unterschieden in der Leistung und der Alterung führen. Es werden unterschiedliche elektrische Netzwerkstrukturen untersucht und robuste und bevorzugte Strukturen identifiziert, um geringere Schwankungen der volumetrischen Energiedichte und Degradation zu erzielen.

Zusammenfassend tragen die Ergebnisse der Dissertation dazu bei, ein wissensbasiertes Verständnis darüber aufzubauen, wie sich Unsicherheiten im Bereich der Produktion und der Elektrodenstruktur auf die elektrochemischen Eigenschaften von Lithium-Ionen-Batterien auswirken. Es werden Modelle entwickelt, welche eine Beschreibung der notwendigen Zusammenhänge ermöglichen. Basierend auf den Modellen werden verschiedene Untersuchungen durchgeführt, die es erlauben, Schwankungen zu verringern und die Produktqualität der Batterien zu verbessern. Weiterhin wird die robuste Optimierung eingesetzt, um gezielt den Ausschuss im Bereich der Produktion zu verringern. Dadurch wird die Nachhaltigkeit von Lithium-Ionen-Batterien verbessert, da es zu weniger Materialverbrauch im Bereich der Produktion kommt.

Abstract

Nowadays, lithium-ion batteries are applied in mobile communications, stationary energy storage, and electromobility. The great demand for batteries results in an increased interest in production and its impact on performance characteristics. It is necessary to establish production facilities capable of meeting the demand for high-quality batteries. Therefore, it is mandatory to investigate how deviations in product characteristics, e.g., structural features, affect quality measures. In the long term, this will help to reduce the scrap rates and thus improve the sustainability and quality of lithium-ion batteries.

The dissertation studies how uncertainties induced by the production processes affect the electrode structure and the electrochemical properties. Mathematical models are used to analyze how different types of deviations propagate and evolve along with the production processes and affect the electrochemical properties of the battery. The goal is to identify sensitive production processes and structural parameters. In addition, robust electrode structures are identified, resulting in reduced deviations based on their specific design.

The first part discusses how deviations caused by the production affect the performance of lithium-ion batteries. For analyzing that, models describing the single production processes are coupled with an electrochemical battery model. The approach allows the continuous description of the relationships between the process parameters, the electrode structure, and the electrochemical properties. The resulting platform is applied in a case study to investigate how deviations in production propagate and consequently affect performance. It is shown, that the electrode coating process is the most sensitive process for the analyzed settings. That process defines the loading of the electrode with active material and thus also the performance. The approach further enables studying interactions between production steps. It is identified that interactions occur between the coating and calendaring process since the same structural parameters are affected. Following the case study, a robust optimization is implemented on an electrochemical battery model. The goal is to identify cathode structures that provide consistent performance even when the structure is affected by deviations. It is observed that high-energy electrodes with high layer thickness and low porosity tend to have high deviations in performance at operating points where mass transport in the electrolyte is the limiting factor. By applying robust optimization, the volumetric energy density is slightly reduced, and limitations in mass transport in the electrolyte are avoided. That prevents a drop in performance. Consequently, the standard deviation is decreased, and the scrap rate in production is significantly reduced.

In the second part of the work, the microstructure of the electrode is studied in detail. The focus is on the structure of the carbon black-binder matrix. Despite identical volume fractions, a changing network structure of the matrix can result in deviations in performance and aging. Different electrical network structures are investigated, and robust and preferred ones are identified to achieve low deviations.

In summary, the results of the dissertation contribute to building a knowledge-based understanding of how uncertainties in production and electrode structure affect the electrochemical properties of lithium-ion batteries. Models are developed which enable representing the relevant relationships. Based on the models, investigations are carried out, enabling a reduction of deviations and improving product quality. Furthermore, robust optimization is used to reduce scrap in production. That improves the sustainability of lithium-ion batteries, as there will be less material consumption in the production area.

Acknowledgments

Research is rarely done by a single person. That also applies to my dissertation. At this point, I would like to thank all people who contributed to this work and supported me during the last few years.

First of all, I would like to thank my supervisor Prof. Dr.-Ing. Ulrike Krewer, for the guidance, the constant support, and for challenging me to improve my results and work.

Many thanks to Prof. Dr.-Ing. Fridolin Röder, who contributed to this work with his ideas, creativity, and support. Additionally, I would like to thank him for being my second referee. Thanks also to Prof. Dr.-Ing. Michael Heizmann for chairing my examination board and to Tenure-Track-Prof. Dr. Ulrich Wilhelm Paetzold and Prof. Dr. rer. nat. Wilhelm Stork for being part of my examination board.

Special thanks to my colleagues from InES. The scientific and non-scientific discussions, the great working atmosphere, the cookies, and some very nice moments, have contributed that not only this work has been improved, but at the same time, the fun and motivation have not been lost. Here I would like to mention in particular: Maximilian Röhe, Vincent Laue, Walter Cistjakov, Fridolin Röder, Fabian Kubannek, Florian Baakes, Lars Bläubaum, Marco Heinrich, Nicolas Wolff, Wilfried Jansen, Nina Harting, Ina Schunke, and Horst Müller.

I am also thankful to the members of my research projects. Especially Matthias Thomitzek, with whom I worked on both projects and published several articles. Thank you, Matthias, for the great and successful teamwork in Sim2Pro and Sim4Pro.

Finally, I would like to thank my family, starting with my parents and brothers. Special thanks to my wife Caroline, who supported me even when nights and weekends were blocked by this work. Thanks also to my little Frieda, who had a smile for me whenever I needed it in the last months.

Braunschweig, im Juni 2023

Oke Matthias Schmidt

Contents

Kurzfassung	i
Abstract	iii
Acknowledgments	v
1 Introduction	1
1.1 Motivation	1
1.2 Scope	2
1.3 Outline	3
2 Fundamentals	5
2.1 Lithium-ion battery	5
2.1.1 Structure, operation and materials	5
2.1.2 Porous electrode microstructure	8
2.1.3 Degradation and aging	10
2.2 Production of lithium-ion batteries	12
2.2.1 Electrode preparation	12
2.2.2 Cell assembly	15
2.2.3 Formation	15
2.2.4 Quality in battery production	16
2.3 Modeling in context of lithium-ion batteries	17
2.3.1 Modeling operation of lithium-ion batteries	17
2.3.2 Homogeneous electrochemical model	19
2.4 Uncertainty quantification	22
2.4.1 Polynomial chaos expansion	23
2.4.2 Sensitivity analysis	25

Part 1 - Uncertainties from Electrode Production	29
3 Modeling Process-Product Interdependencies in Battery Production	31
3.1 Introduction	31
3.2 Computational methods: The framework	32
3.2.1 Process chain model	34
3.2.2 Battery cell model	35
3.2.3 Analysis module	36
3.3 Concluding remarks	36
4 Impact of Production Induced Uncertainties on Battery Performance . . .	39
4.1 Introduction	39
4.2 Computational methods	40
4.2.1 Process chain model	41
4.3 Model parameterization	43
4.3.1 Process chain model	44
4.3.2 Battery cell model	44
4.4 Definition of the case study	46
4.5 Discussion of the simulation results	48
4.5.1 Production impact on structural parameters	48
4.5.2 Battery performance	51
4.6 Concluding remarks	59
5 Robust Design of Lithium-Ion Battery Cathodes	61
5.1 Introduction	61
5.2 Experimental cell setup	63
5.3 Electrochemical model	63
5.4 Impact of mass loading and coating density	66
5.5 Deterministic optimization of the cathode design	71
5.5.1 Implementation	72
5.5.2 Simulation results	72
5.6 Influence of uncertainties on optimal cathode design	75
5.6.1 Implementation	75
5.6.2 Simulation results	75
5.7 Robust design optimization of the cathode design	79
5.7.1 Implementation	79
5.7.2 Simulation results	80
5.8 Concluding remarks	84

Part 2 - Uncertainties from Electrode Microstructure	87
6 Uncertainty of Heterogeneous Conductive Networks	89
6.1 Introduction	89
6.2 Computational methods	91
6.2.1 Hybrid model	92
6.2.2 Electrical network model	93
6.3 Results	99
6.3.1 Structural network properties	100
6.3.2 Electrical network properties	102
6.3.3 Influence of percolation on electrical conductivity	105
6.3.4 Estimation of uncertainties in the cell performance	105
6.3.5 Degradation of the electrical network and cell failure	109
6.4 Concluding remarks	114
7 Conclusion	117
7.1 Summary	117
7.2 Future challenges	120
Bibliography	121
List of Figures	135
List of Tables	139
List of Symbols and Abbreviations	141
A Parameter and Model Validation	147
A.1 Data for Chapter 4	147
A.2 Data for Chapter 5	149
A.3 Data for Chapter 6	152
B Estimation of Structural Data of Electrodes	155
C Comparison of Degradation of Electrical Networks	157

1 Introduction

1.1 Motivation

Climate change caused by human-induced emissions is one of the biggest challenges of our time, whereas still the global energy consumption and emission of greenhouse gases are steadily increasing [1]. That is critical, as drastic reductions in CO₂ emissions are needed to comply with the Paris Agreement, whose goal is to limit global warming to well below 2 °C. Hence, technology is needed that covers the global energy demand and simultaneously pollutes and stresses the environment less to enable sustainable growth. For enabling renewable energy, carbon-free mobility, and mobile communication, the critical issue of energy storage must be solved. Here, electrochemical systems provide promising and sustainable solutions [2]. Especially the lithium-ion battery (LIB) is currently the most industrialized and advanced electrochemical system due to its high energy density and relatively low production costs [3].

Despite its success in recent years, the LIB needs further improvement. The main challenges are increasing the energy and power density, prolonging the lifetime, improving safety, and reducing the environmental impact [4]. Tackling these points is commonly done by adapting the cell design, optimizing the electrode structure, or changing the materials [5–7]. Besides, mass production of large-format LIBs is crucial for providing large volumes of batteries. The growth rates in electric mobility result in a sharp increase in the demand for high-quality batteries [8]. Hence, improving the production process is important for producing highly optimized LIBs with consistent quality [9]. That is especially of interest when assembling single battery cells into large battery packs consisting of hundreds of cells. Strong performance deviations between the individual cells electrically coupled within the battery pack are known to result in decreased lifetimes. The current distribution within the pack becomes strongly inhomogeneous, and balancing the cells is more advanced [10, 11]. Hence, it is necessary to generate electrode structures that react robust against deviations and provide consistent performance. Thereby, the scrap rate in the production is reduced. Consequently, the amount of waste decreases and the sustainability of battery production is improved and costs are lowered.

To improve the quality of LIBs it is crucial to understand how deviations occur, how they are influenced, and, most importantly, how to adjust them through targeted optimization. Experimental studies have analyzed and quantified how deviations in electrode structure result in performance

deviations between single cells. That is referred to as cell-to-cell deviations. The impact of structural features like electrode thickness, porosity, electrode mass, and density was studied [12–14]. Besides cell-to-cell deviations, also the impact of local heterogeneities within the electrode structure is of interest. Here, two electrodes have the same averaged structural features, but varying local microscopic structures lead to deviations in performance [14, 15]. The presented analyses provide an overview of how deviations in battery production can be related to structural features of the LIB. However, they are limited in correlating the deviations in structure with the internal physical processes of the LIB.

Enabling that is possible by implementing electrochemical models describing the physical processes based on material and structural parameters. Analyzing the effect of uncertainties was already done by applying methods of uncertainty quantification to these models to identify the most sensitive parameters and to predict deviations in performance [15, 16]. These model-based studies focus on correlating the impact of structural and material parameters on electrochemical performance. Detailed analysis of how deviations in production and electrode structure evolve and how they affect the physical processes within the battery does currently not exist. Additionally, the studies lack performing knowledge-driven optimization of the LIB to reduce the deviation of battery performance.

1.2 Scope

The scope of the thesis is on developing model approaches and methods able to estimate robust electrode designs. Thereby, deviations in quality are reduced because uncertainties in structure have a minor impact on performance. Therefore, approaches are developed focusing on mapping the impact of different types of deviations and their effect on the internal physical processes and performance. As already discussed in the motivation, two types of deviations are distinguished. Considering both types is done by dividing the thesis into two parts and providing individual modeling approaches.

The first part focuses on cell-to-cell deviations arising in the production process. Here, coupled modeling of production and operation of a LIB enables knowledge-driven analysis of uncertainties and optimization of the production process and electrode structure. Sensitive process parameters and robust design points are identified.

In the second part, the impact of local heterogeneity in the electrode microstructure is studied. In this study, the focus is solely on the structure of the electrical network. A model is established able to represent the effect of a varying network structure and analyze the impact on uncertainties in performance and degradation. Thus, robust electrical network structures are identified.

By addressing these two topics, the impact of structural deviations on battery quality is studied,

and the robustness of the electrode microstructure is improved. That includes considering uncertainties between homogeneous electrodes (Part 1) and deviations arising from heterogeneities within the electrode (Part 2).

1.3 Outline

Identifying robust electrode structures requires a detailed understanding of LIBs as a system. That allows correlating uncertainties in electrode microstructure to physical processes and performance. A brief overview of relevant aspects of this work is provided in the fundamentals. First, the operation, porous microstructure, degradation, and production processes of LIBs are discussed. Furthermore, a physical-based modeling approach is presented, and mathematical methods regarding uncertainty quantification, meta modeling, and sensitivity analysis are provided. Studying two different types of uncertainties is done in two separate parts in this work.

In Part 1, the focus is on process-induced uncertainties in the production process and estimating robust electrode structures. In Chapter 3, a coupled model approach is presented that combines a process chain model and a battery cell model in a digitalization platform. This framework enables studying the correlations between the process, structure, and electrochemical performance properties. In Chapter 4, the framework is applied to analyze the propagation of uncertainties along the production process and rate the impact on the electrochemical performance. A case study following a Monte-Carlo-based approach is conducted. This enables identifying sensitive process parameters regarding their effect on electrochemical performance. In Chapter 5, the design of cathodes is optimized under consideration of uncertainty. The aim is to identify electrode designs whose performance is robust against deviations in the structure. Consequently, the scrap rate in production is reduced.

In Part 2, the focus is on heterogeneous electrode microstructures and the resulting uncertainties. The heterogeneous structure of the carbon black-binder matrix is studied in-depth, and the effect on electrochemical performance and degradation is studied. This includes studying uncertainties arising from different network structures. In the end, robust structures are identified in terms of reduced uncertainties in energy density and a more robust degradation.

The obtained results improve the understanding of correlations between process, structure, and properties by physical-based modeling approaches. The generated knowledge is used to optimize the design of LIBs. Methods are applied and established to study the effect of various uncertainties and heterogeneities. The methods are applied to improve the quality of produced LIBs.

2 Fundamentals

This chapter provides an overview of LIBs and topics relevant to this thesis. It covers the fundamentals of structure, operation, aging, and production of LIBs. These topics are of interest because the thesis aims to improve understanding of how they are related and interact. That is to be achieved by model-based approaches. Therefore, in the following, models are presented, focusing on the physical processes and operation of the LIB. Finally, mathematical methods for sensitivity analysis and meta modeling are presented.

2.1 Lithium-ion battery

Here, basic information is provided necessary to understand the LIB as an electrochemical system. First, the structure, components, and materials are briefly introduced. The porous microstructure of the electrode has a significant impact on the physical processes occurring in the battery and is established and affected in production. Evaluating and optimizing this structure is the focus of this work, and hence it is discussed in detail. In addition to the initial electrochemical performance at the beginning of the lifetime, the degradation is analyzed in the second part of this work. For better understanding, an overview of the aging and degradation mechanisms of LIBs is provided.

2.1.1 Structure, operation and materials

The lithium-ion battery is an electrochemical system converting chemical energy directly into electrical energy via electrochemical reactions. The oxidation and reduction occur spatially separated by an electrolyte and separator but electrically connected via an external conductor. The physical processes are reversible, making the battery rechargeable. Thus it belongs to the group of secondary batteries [17].

The LIB consists of a positive and negative intercalation electrode storing and releasing lithium ions, the electrolyte enables ionic transport between the two electrodes, and the separator prevents physical and electrical contact of the electrodes while allowing ionic transport. The cell structure is illustrated in Figure 2.1. The single components are discussed in the following.

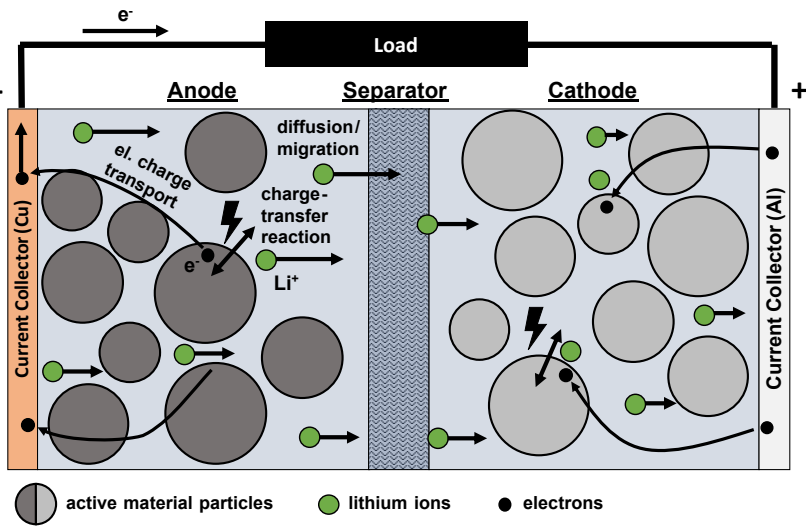


Figure 2.1: Structure of the lithium-ion battery (LIB) with its four main components (anode, separator, cathode, and electrolyte). The most relevant physical processes are indicated. The light blue background represents the liquid electrolyte and the spheres the active material (AM) particles in the respective electrode.

The separator is a porous membrane placed between the two electrodes. It is commonly made of polymers or a composite of polymers and ceramics. The separator should not involve in any cell reactions and thus needs to be chemically and electrochemically stable. Due to temperature changes in the battery, it also needs to be thermally stable. Detailed information about requirements, properties, and materials can be taken from Lee et al. [18]. The porous electrodes and the separator are flooded with the liquid electrolyte. Commonly, it is a lithium salt, e.g., $LiPF_6$, dissolved in a solvent, e.g., ethylene carbonate (EC). The composition of the electrolyte affects the formation of the solid electrolyte interface (SEI) at the surface of the anode active material particles. For more information about the SEI it is referred to Chapter 2.1.3. Additives in the electrolyte can be used to tune the SEI in terms of uniformity and stability. That is beneficial in terms of internal resistance and aging. An overview and perspectives concerning electrolytes and additives are provided by Haregewoin et al. [19]. The lithium ions transported in the electrolyte are stored and released by the crystal host structure of the active material (AM) in the electrodes. That process is called intercalation and deintercalation of the ions. The major structural features of the host are not affected by this process. An overview of the mechanisms and relevant intercalation materials is provided by Winter et al. [20]. Commonly, the AM at the anode is graphite, and at the cathode, a lithium metal oxide (LMO) or phosphate is used. The AM defines the storage capacity of the LIB and thus highly affects the electrochemical performance. Due to its impact, conventional AMs are discussed at the end of this section in detail. For enabling electrochemical reactions and thus the intercalation/deintercalation, sufficient electron supply must be ensured by the electrode. The AM is coated on a current collector for electrically connecting the

coating to the external circuit and enabling electron transport. Usually, the current collector at the cathode is made of aluminum, and copper is used at the anode. The different metals are used due to the local electric potentials at the two electrodes and the electrochemical stability of the materials.

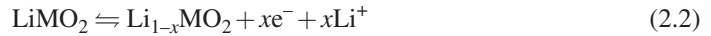
At this point, the structure and components of the battery are defined. However, the physical processes occurring during operation were only briefly mentioned and not explained. That is the focus in the following.

The operation of the LIB is characterized by the kinetics of the electrochemical reactions and transport processes. They run simultaneously and interact with each other. The most important physical processes are indicated in Figure 2.1.

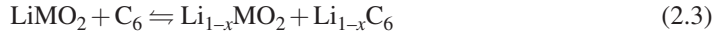
For initiating the electrochemical reactions, a potential difference must be present between the two electrodes. In a LIB with graphite at the anode and lithium metal oxide at the cathode the overall reactions at the surfaces of the AM particles can be summarized as



for the anode,



for the cathode, and



for the full cell. Focusing on the discharge process of the LIB, oxidation occurs at the surface of the graphite particles in the anode. During the charge-transfer reaction, lithium ions enter the electrolyte and free electrons are released into the conductive solid phase (see eq. 2.1). The concentration and potential gradient in the electrolyte enable ionic transport. Hence, lithium ions are transported from the anode to the cathode due to diffusion and migration. Simultaneously, electrons pass through an external electrical circuit and can be used to power electronic devices. At the surface of the cathode AM, the lithium ions enter the crystal structure by counterbalancing their charge with an electron from the solid phase (see eq. 2.2). In both AM particles, lithium is transported by diffusion from the center to the surface or vice versa depending on the concentration gradient. Charging the battery leads to a reversal of the physical processes by applying an external electrical power source and adapting the electrical potential. The described physical processes define the electrochemical performance of the battery.

The two main quantities evaluating the performance of a battery are the battery cell capacity and voltage. The capacity is defined by the utilizable concentration difference in the respective intercalation materials and the voltage by the potential difference between the electrodes. Additionally, the battery needs reasonable charge/discharge rate capability, consistent and low aging rates, and safety must be ensured. The battery cell capacity is the most important characteristic and is mainly affected by the selected active material. Therefore, different AMs are discussed in

detail in the following.

Extensive research was already carried out on suitable electrode materials to increase the capacity and voltage of the lithium-ion battery. The most common materials at the cathode are, for example, lithium cobalt oxide (LiCoO_2 , LCO), lithium iron phosphate (LiFePO_4 , LFP), or the mixed nickel-manganese-cobalt dioxide ($\text{LiNi}_{1-y-z}\text{Mn}_y\text{Co}_z\text{O}_2$, NMC). In particular, NMC is widely used, with changing proportions of the individual metallic components, the trend is towards higher nickel proportions and lower proportions of cobalt and manganese. Detailed information about these materials can be taken from Whittingham [21]. More recent advances in terms of positive electrode materials are summarized by Ellis et al. [22]. Here, additionally, materials for recent developments in lithium-ion batteries and next-generation batteries, e.g., lithium-sulfur or lithium-air cells, are reviewed. At the anode, alloy negative electrodes are of interest to increase the theoretical capacity and the rate capability, especially for fast charging applications. Here, Si-C (silicon-carbon) is already used, but different materials are possible. A detailed review of negative alloy electrodes is provided by Obrovac et al. [23].

The active material in the electrode defines the theoretical capacity and equilibrium potential of the LIB by its intrinsic thermodynamic limits [22, 23]. The porous electrode structure, on the other hand, needs to be designed to achieve the highest possible utilization and efficiency by favorable kinetics. The electrode structure needs to be designed suitable for the respective operating conditions. In the following this porous electrode structure is discussed in detail, especially concerning its effect on the kinetics.

2.1.2 Porous electrode microstructure

In industrial applications of electrochemical storage devices, porous electrodes are widely used. Compared to plane electrodes, the porous microstructure strongly affects the dynamic characteristics [24]. The reason for this is that the structure has a direct impact on electrical and ionic transport pathways and the active surface area, being reactive interfaces. Hence, it has a significant impact on the kinetic processes characterizing the electrochemical performance of the LIB [25–27]. That's why it is of interest to study the porous microstructure in-depth.

In Figure 2.2, the complex porous microstructure is simplified in a schematic representation and the kinetic processes are indicated. Understanding the correlations between porous microstructure, reaction kinetics, and transport properties are essential to produce batteries of high and consistent quality, reaching the theoretical potential of the AM [28]. In this chapter, the microstructure of anode and cathode is treated similarly, even though the materials and compositions might vary, the overall effects are comparable.

The porous microstructure in lithium-ion batteries consists of two phases in the same volume: the liquid and solid phase. The liquid phase is defined by porosity (void volume fraction) that is filled with liquid electrolyte [24]. The solid phase provides the porous matrix and consists of

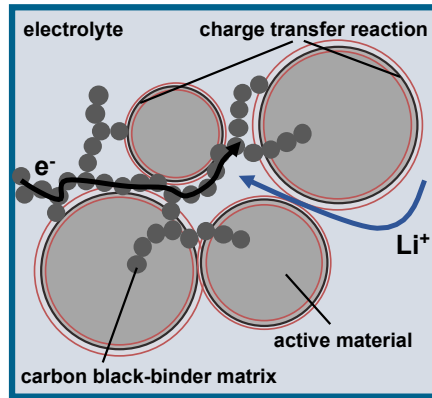


Figure 2.2: The different components and processes are shown schematically. The active material (AM) and the carbon black-binder matrix (CBM) form the porous microstructure. Pores are filled with electrolyte. The electrolyte enables a flow of lithium ions and the CBM provides the electron transport. At the surface of the AM particles the charge transfer reaction occurs.

the active and inactive components. Detailed information about common AMs is provided in Chapter 2.1.1. The inactive materials are binder and conductive additives. The binder enables the mechanical integrity of the composite structure and the conductive additives allow electrical charge transport. In both electrodes, polyvinylidene fluoride (PVDF) is used as a binder. Due to environmental issues and processing costs, manufacturers start to replace PVDF. Especially, at the anode, aqueous base materials, e.g., styrene-butadiene rubber (SBR), are used. The conductive additives are commonly a carbon black (CB) or conductive graphite [29].

The porous structure is mainly established to increase the active surface area and compensate for the overall sluggish reaction kinetics [24]. Furthermore, the electrochemical reactions are evenly distributed through the electrode volume rather than being focused at the cross-sectional reaction-front facing the counter electrode. Thus, the local current density is reduced and kinetic bottlenecks and high local concentrations of reactants are avoided. This is beneficial in terms of the reversibility, coulombic efficiency, and cycle life [30]. At the same time, however, the microstructure affects the species and charge transport in the liquid and solid phase. Especially the ionic diffusion and migration in the liquid phase are hindered by the solid phase matrix, blocking direct transport paths [31, 32]. The length of these paths is increased due to the porous structure, that is quantified by the tortuosity. Limitations occur and affect the performance and lifetime of the battery. The electrical charge transport in the solid phase is mainly provided by a matrix consisting of CB and binder, i.e., the carbon black-binder matrix (CBM). This matrix has a complex three-dimensional structure that needs to be taken into account when describing the physical transport processes within the electrode. Furthermore, the CBM affects the reaction kinetics by reducing the active surface area [26, 33].

To sum up, the microstructure affects the transport processes and the electrochemical reactions. That has to be considered in the design process. The microstructure requires to be designed to

enable fast reactions but non-limiting transport. Due to its importance, the design and optimization of the electrode microstructure are the subjects of various experimental and model-based scientific research studies. [34, 35]. However, universal optimization is not possible because the design is highly dependent on the field of application. For example, lithium-ion batteries with high energy densities usually have increased layer thicknesses and therefore a distinct decrease in capacity and voltage is already noticeable at moderate discharge rates [36]. Here, e.g., special structuring of the electrodes is conceivable [37]. The complexity of lithium-ion battery electrode optimization is discussed by Witt et al. [38], as they distinguish between special requirements for charging and discharging. Hence, the design issues for batteries are multifaceted. This leads to different challenges that have to be taken into account during design and manufacturing of electrodes and battery cells.

2.1.3 Degradation and aging

A consistent and low aging rate was mentioned previously as an important quality aspect for LIBs. Batteries need to be durable, especially for being a viable alternative in terms of sustainability. Hence, long-term cycling and a consistent storage capacity are of interest. Different aging mechanisms occur reducing the lifetime of the battery. In general, aging can be classified into calendaric and cyclic aging. Calendaric aging happens during storage. Cyclic aging occurs during operation and thus charge and discharge of the battery. Here, the focus is on cyclic aging. For detailed information about calendaric aging, it is referred to Broussely et al. [39].

Aging in lithium-ion batteries and thus capacity decrease and energy fade do not originate from a single cause, but various processes interact with each other. The aging effects and processes differ between anode and cathode. In the following the main aging mechanisms for both electrodes are briefly reviewed based on the work of Vetter et al. [40] and Barré et al. [41]. In Figure 2.3, the different aging mechanisms are summarized and visualized.

At the graphite anode, aging is driven by changes at the electrode/electrolyte interface. The anode operates at potentials outside of the electrochemical stability of the electrolyte components. In the charged state, i.e., at low potential, a reductive decomposition of the electrolyte accompanied by irreversible loss of lithium ions occurs at the electrode/electrolyte interface. The decomposition products form a layer at the surface of the AM particles, the SEI [43]. It is permeable for lithium cations but rather impermeable for the electrolyte components and electrons. Hence, the layer mainly forms at the beginning of the battery utilization. During further cycling of the battery, the SEI protects the electrolyte components from further reduction and the charged electrode from corrosion. However, the electrolyte decomposition is still an ongoing process throughout the entire battery life but compared to the first cycles to a lower extent [43]. Comparable to SEI formation, lithium plating appears at the graphite anode when a high diffusion

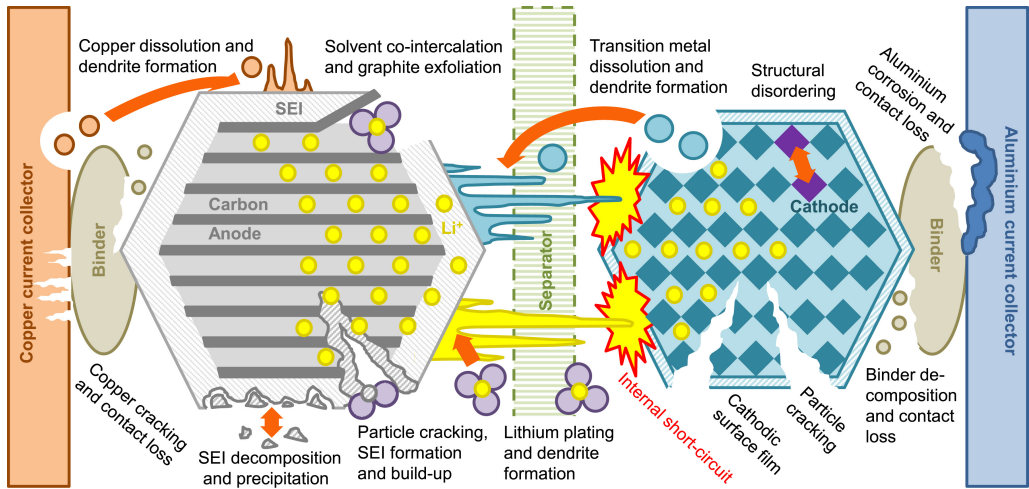


Figure 2.3: Degradation mechanisms in lithium-ion battery cells. Taken from Birkel et al. [42] (CC BY 4.0).

resistance occurs, e.g., due to low temperature. Hence, the potential is close to lithium metal and metallic lithium plating, and lithium dendrites can grow. This can induce, or accelerate aging and can lead to critical safety issues [44]. In the anode, only minor changes occur for the AM. The volume change during intercalation and deintercalation is with approx. 10 % relatively low. Still, graphite exfoliation and graphite particle cracking will lead to degradation and aging. However, using alloy anode materials with silicon makes this aspect more relevant, since a significantly higher volume expansion of up to 300 % is observed for silicon [45]. The mechanical stability of the microstructure can be affected by different degradation effects. Contact loss between the different components can occur due to disintegration. The SEI and the volume change of the AM affect the porosity and thus the ionic diffusion and conductivity. Corrosion can occur at the current collector and result in loss of electrical contact between the porous electrode coating and the metallic current collector. [40, 41]

At the cathode, the electrode/electrolyte interface is not critical due to the electrochemical stability of the electrolyte at the respective potential. However, at very high potentials a decomposition of the electrolyte can occur at the cathode and form the cathode electrolyte interface (CEI) [46]. Aging in the cathode can be distinguished between inactive and active components. The AM can be aged due to structural disordering, phase transitions, and metal dissolution. Structural disordering occurs when transition metal replaces lithium ions in the structural sites. Phase transition occurs during lithiation and delithiation of the AMs. This leads to a distortion of the crystal lattice, resulting in mechanical stresses and particle cracking. Parts of the metallic host structure at the cathode dissolve into the electrolyte and are transported to the negative electrode. This results in side reactions and aging. The inactive materials in the microstructure can also be affected by aging. Binder decomposition leads to a disintegration of the porous electrode structure

and the electrical transport paths. The conductive agents can be affected by oxidation and the current collector can be degraded by corrosion. Both processes result in a loss of contact and a rise in impedance. Hence, the performance of the battery reduces. With higher disintegration/degradation of the inactive materials (CBM), the electrical charge transport to the reaction sites can be affected, and thus also the capacity can decrease due to isolated AMs [42]. [40, 41]

The discussed aspects concerning structure, operation, porous microstructure, and degradation of the LIB elucidate that the electrochemical system has high complexity. It is mandatory to achieve good interaction between the micro kinetics of the charge-transfer reaction at the surface of the AM particles and the macro kinetics, transporting the charges and species to the desired locations. For production of the battery cell, the established materials and structures must be carefully designed to be robust against deviation in performance, mechanical disintegration, side reactions, and electrolyte decomposition.

2.2 Production of lithium-ion batteries

In the previous section, the impact of material and microstructure on electrochemical performance and degradation was discussed. For production of LIBs, it is of interest to generate the desired structure defined in the development process with sufficient accuracy to achieve high performance and long cycle life.

The production process of LIBs is divided into three parts: electrode preparation, cell assembly, and formation. An overview of the production process is provided in Figure 2.4. The single steps are discussed in the following. The focus is on electrode preparation, as it mainly defines the discharge capacity of the battery by defining the mass loading of the active material and the microstructure. Cell assembly and formation are introduced for completeness. Additionally, a short discussion about battery quality is added. The following review is based on the work of Kwade et al. [9] and Liu et al. [47].

2.2.1 Electrode preparation

State-of-the-art electrode preparation is based on liquid suspension and web coating. In the beginning, the individual components are weighted according to the recipe. Commonly, the electrode slurry consists of AM, conductive additives, polymer binder, and solvent. The formulation of the electrode suspension starts with the mixing process (see Figure 2.4). Here, wet mixing is mandatory, while additional dry mixing is optional. The dry mixing is used to blend and structure the AM with the conductive additives and the binder. The premixed dry components and the

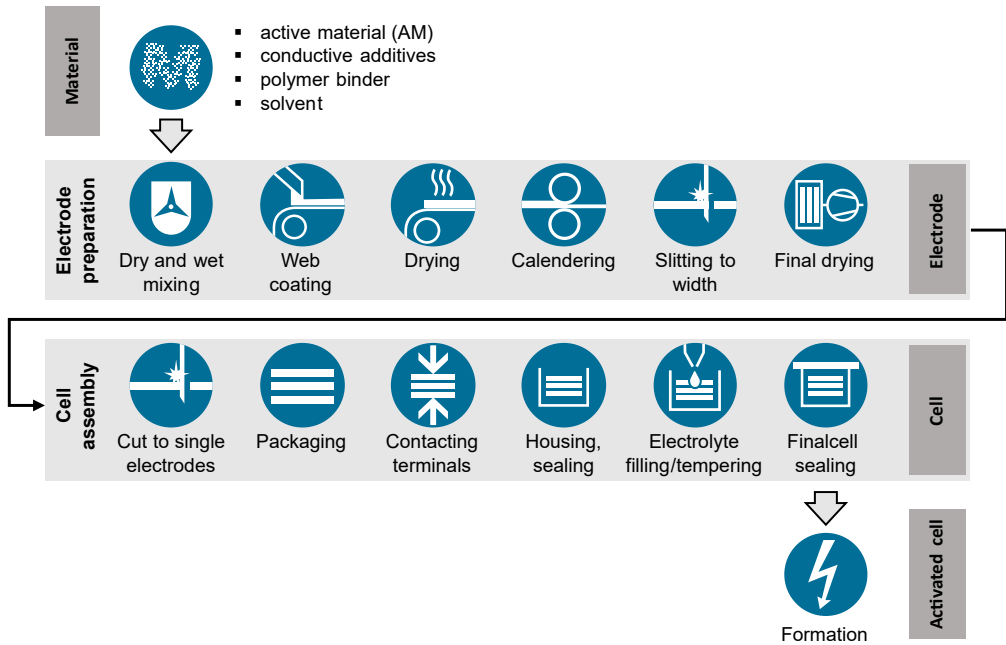


Figure 2.4: Overview of the manufacturing processes for conventional lithium-ion batteries. The figure is reproduced and simplified based on Kwade et al. [9].

solvent are fed into a batch process for the wet mixing. Therefore a planetary mixer or a different type of high-intensity mixer is used. The conductive additives are structured and homogeneously dispersed in the suspension. The intensity used in the two mixing processes must be set to obtain defined product quality, i.e., particle size distribution and slurry homogeneity. In the end, the suspension is degassed and filtered to achieve a stable, homogeneous suspension free of gas and agglomerates. Rating the quality of the suspension is done by rheological properties, e.g., density and viscosity. These properties are also of interest for a matching coating process as its parameters are affected and defined based on the mixing process. The performance of the lithium-ion battery is directly affected by the mixing process. The active surface area and the electrical and ionic pathways in the electrode microstructure are defined dependent on the amount and structure of the established agglomerates consisting of binder and conductive additives [48, 49]. [9, 47]

The suspension is applied in a slot die coating process on both sides of the current collector in consecutive process steps. The coating can be conducted continuously or in patterns, i.e., intermittently in single or multiple strips. The type of coating depends on the electrode, current collector and targeted cell geometry, throughput, calendering technology, and minimization of the scrap rate. The last points are especially of interest due to interactions between coating and calendering, e.g., wrinkling of the electrode may occur [9]. The coating speed is commonly in the range of 25–50 m/min. Increasing the speed is possible, but then the coupled drying process

must be adjusted. The length of the dryer must be increased, resulting in a higher number of process parameters that then need to be controlled. The dryer usually operates based on convective principles. Inside the dryer, a dry air or nitrogen environment is created. Minimal dwell times (1–2 min), high throughput, and favorable microstructure are achieved by adjusting the drying rate. Solvent recovery and closed-loop handling are required for N-Methyl-2-Pyrrolidone (NMP) based cathodes to reduce the environmental impact. The structure of the dry electrode is defined by mass loading, porosity, and tortuosity. Here, mass loading is directly linked to electrode thickness. Furthermore, it is of interest to prevent binder migration during drying. This can result in reduced mechanical stability and affect electrical and ionic transport properties due to blocking of the electrode surface and a gradient of conductive additives [31, 36]. The structural features affected by the coating and drying process are of interest for optimizing battery performance. The interaction between electrode thickness, porosity, and tortuosity is of interest for multiple optimization problems and needs to be defined in detail depending on the application of the lithium-ion battery. [9, 47]

In the following process step, the dry electrode is compressed in a two-roller calender at line speeds of 30–100 m/min to increase the volumetric energy density and enhance other physical properties. Especially, porosity, tortuosity, adhesion, and electrical conductivity are affected by the compression of the electrode. Besides the line speed, the line loading with approx. 500 N/m for graphite anodes and 1000 N/m for NMC cathodes is important. Improving the quality can be achieved by heating the rolls and thus wrinkling of the electrodes can be reduced. The structure of the compressed electrode is described by the coating density, i.e., the ratio of the electrode coating mass and volume (neglecting the current collector). The calendaring process is of special interest as multiple features of the electrode microstructure are affected simultaneously. The thickness, porosity, and tortuosity are defined and thus the reaction kinetics and the transport of species and charges are affected. The lithium-ion battery performance strongly depends on these processes and thus the calendaring is of high relevance [27, 32]. [9, 47]

After calendaring, the electrodes are slit to length and width and again dried before they are transported to the clean and dry room where the cell assembly is done. This final drying step is important to limit and adjust the moisture of the cell and thus minimize the effect of water on the lifetime due to unwanted side reactions[50]. [9, 47]

At the end of the electrode preparation, different quantities can be used to rate the manufactured electrode. Here, structural parameters, mechanical properties, and electrical properties are of interest. The thickness of the electrode needs to be consistent, the edge geometry of the slitted electrodes needs to be exact, low porosity and tortuosity should be achieved, high adhesion to the substrate, no defects, sufficient mechanical coating stability, low electrical resistance, and impedance are important. [9]

These processes represent the current and industrialized state of electrode preparation. They are constantly adapted, and new processes are investigated. The focus is on improving the electrochemical performance of the battery, reducing the environmental impact, and lowering costs.

One example for improving battery production is using an extruder in the mixing process. It enables a continuous process and lowers the solvent content [51]. Furthermore, dry coating is also investigated where the solvent is completely removed. This reduces the environmental impact and lowers energy consumption by removing the drying process [52, 53]. These promising new technologies could help to reduce energy consumption and improve sustainability in production.

2.2.2 Cell assembly

The cell assembly is performed in a dry room (ambient temperature around 20 °C, dew point usually -40 to -60 °C) to prevent moistening of the electrode. The main steps in cell assembly are defined by the desired cell format (round wound, prismatic wound, stacked, Z-folded) and thus the structure of the electrode-separator assemble (ESA). Three prevailing processes are currently used to generate the ESA. The first is winding, which is commonly used for small cell formats. In this process, the electrode format and the energy density are limited. Bending stress in the electrodes causes formation of cracks and increasing the electrode thickness supports this issue. The second process is stacking. Compared to winding thicker electrodes are possible due to reduced stress while handling of the electrodes and thus the achieved energy density of the assembled cell is increased. In comparison to winding, it is difficult to achieve the same level of productivity and precision. The third process is Z-folding where discrete electrode sheets are inserted into a zigzag folded endless separator. This process provides improved safety and increased energy density. [9]

In the following, the assembled ESA is contacted internally at the tabs. That is commonly done by ultrasonic or laser welding. The ESA is then inserted into the housing which can either be a hard case or pouch bag. The electrolyte is filled into the housing under a weak vacuum and in extremely dry conditions. In the filling process, metering precision, foaming, and the proportion of electrolyte evaporation have to be considered. Following the filling process the housing is sealed. The battery is now closed and electrochemically active. The batteries are stored under temperature-controlled conditions to ensure wetting and gas diffusion. [9]

2.2.3 Formation

The production process of the LIB is completed by the formation. In the formation process, an electrical current is applied for the first time on the battery. In these first cycling steps, the pristine surface of the graphite particles is covered with the SEI layer due to electrolyte decomposition at the electrochemically active surfaces [43]. Information about causes and processes of the SEI growth can be taken from Chapter 2.1.3. Concerning the formation process, it is again highlighted that the surface of the AM particles in the anode is passivated. The SEI is permeable

to lithium ions but impermeable for electrons and electrolyte components and thus the further decomposition of the electrolyte is hindered. Hence, the formation process is crucial for the product quality, because it has a significant impact on aging and thus on the lifetime of the battery. However, due to the formation process approx. 10 % of the reversible lithium is consumed and consequently the cell capacity is reduced [54]. In comparison, the protective mechanism of the SEI is more important and it is of interest to generate homogeneous and stable layers in the first cycling steps. This is mainly achieved by low current densities in the first cycling steps and defined environmental conditions. The process control of the formation is discussed in various scientific papers, as still many physical effects are not clear and achieving a fast and reliable process is challenging [55, 56].

2.2.4 Quality in battery production

Following the formation, the quality of the produced LIB is evaluated. That is done in end-of-line testing and includes, e.g., measuring the cell capacity, the internal resistance, and the aging behavior within a reasonable and defined time (1-2 weeks). Battery cells that do not provide the desired quality within certain boundaries are defined as scrap. They are disposed of or given into the recycling to partially recover the used raw materials. Gaines et al. [57] stated scrap rates depending on the technical maturity level of the production of up to 30 %. A high scrap rate results in increased costs and has a negative impact on the sustainability of the battery production.

Deviations in the quality of the battery are influenced by various factors. They can be caused by the raw materials, or the environment during the production (e.g., moisture) [58]. The main reason, however, is process-induced deviations. Tolerances within the production processes result in non-distinct product properties. Consequently, these deviations affect the performance characteristics. In the coating process, for example, the electrode thickness cannot be set distinctly by the slot die coating [59], and in the drying, the binder migration affects the performance [60]. The line load in the calendaring is not constant, and as a result, the thickness and porosity of the electrode microstructure are not equal for all electrodes [59]. In cell assembly, the stacking accuracy is limited, resulting in reduced positioning accuracy of the electrode sheets [61]. All these exemplary deviations affect the battery performance. Hence, the question is how strong the impact of the single deviations is.

In summary, improving the quality of batteries requires a detailed understanding of how materials, process, structure, and performance correlate and interact. It is important to study the correlations between process and product in detail. That is possible by modeling approaches. There, the complexity is reduced by focusing on the main processes and interactions. That can generate a basic understanding.

2.3 Modeling in context of lithium-ion batteries

Summarizing the up to this point gathered information concerning the operation and production of LIBs, it is of interest to analyze correlations between material, process, structure, and application. Therefore, it is necessary to describe the impact of structure and material on the internal physical processes and consequently on the performance characteristics of the LIB. In addition to using experiments, mathematical models can provide fundamental insights. They enable studying individual physicochemical processes, and by coupling these, the operation of the LIB can be described. Detailed analysis of the processes greatly increases the understanding of the battery. In addition, models can be used to study physical processes that cannot be resolved by experiments. The execution of model studies and various optimizations will further contribute to reducing the number of experiments through a more targeted approach.

In the following, an overview of models focusing on the performance evaluation of LIBs is provided. The models are discussed regarding the implemented physical processes and their varying complexity and predictability. In the end, a homogeneous electrochemical model is introduced that is implemented and adapted throughout this thesis.

2.3.1 Modeling operation of lithium-ion batteries

Modeling the operation of LIBs is challenging, due to various physical processes interacting on multiple lengths and timescales. Depending on the desired scope, it is of interest to select a model suitable in terms of physical detail and computational costs. The model has to describe the most relevant physical processes for addressing the raised research question, but non-sensitive processes should be neglected to keep the model simple and reliable.

In general, models describing the LIB can be divided into three categories: (I) lumped electrochemical models, (II) homogenized continuum models, and (III) multiphysics models [62]. The models are listed according to increasing complexity. Adjusting and extending the models can change the predictability and level of physical detail, e.g., creating a multiscale model can help predict film formation during operation. Figure 2.5 shows an overview and classification of the different models. Extending the predictability and thus the complexity of the homogenized continuum models and multiphysics models by, e.g., multi-scale modeling, is indicated.

The lumped electrochemical models (I) are non-discretized models without direct consideration of the physicochemical processes. Commonly, they are described as empirical models or equivalent circuit models. They enable fast calculation but are based on the fitting of experimental data. Hence, the prediction for varying battery design and operation is comparably poor. They are commonly applied for battery management and control of battery systems, e.g., for fast charging protocols [62–64].

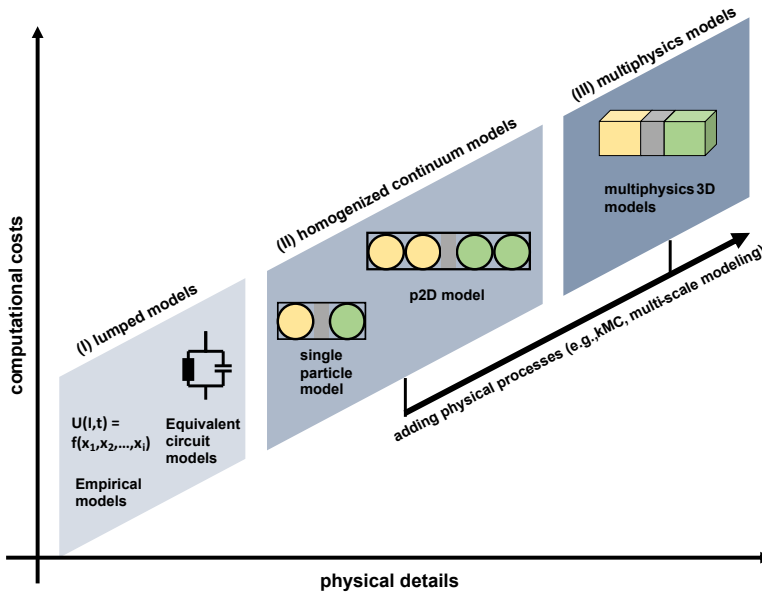


Figure 2.5: Ranking of different models, describing the operation of LIBs. Physical detail and computational costs are displayed for the model types. Adding physical processes and thus increasing model complexity results in improved predictability and higher computational costs.

The most well known homogenized continuum model (II) is the p2D model, established by Doyle, Fuller, and Newman [65–67]. The model considers discretized mass and charge transport in one linear coordinate in the electrolyte/electrode and mass transport in one radial coordinate in the AM particles. Micro kinetics are incorporated in the model. Direct consideration of various physical processes results in more accurate predictions in terms of battery operation. Thus, they enable design optimization of the battery. However, homogenization of the electrode volume simplifies the processes and local effects, e.g., lithium-plating can hardly be resolved. The p2D model is applied for various research questions and several extensions are available for increased model prediction [26, 27, 68]. Due to its high relevance and the application in this work, the homogeneous p2D model is described in Chapter 2.3.2.

The multiphysics models (III) may consider the three-dimensional and heterogeneous porous electrode microstructure in detail [69, 70]. This structure is either artificial, i.e., generated by a stochastic approach, or a reconstruction based on, e.g., micro-CT or FIB-SEM images. The model considers spatial current distribution and the impact of the local microstructure on physical processes can be displayed [69]. Furthermore, multiphysics model can also couple a homogenized 1D electrochemical model with a 3D thermal-electric model to analyze the impact and interaction of electrochemical, thermal and electrical processes for large-format pouch cells [71]. Especially, when studying film formation related to SEI or lithium plating, the incorporation of kinetic Monte-Carlo (kMC) models is an advanced method. In kMC models, the movement,

adsorption, and desorption of reactants at the surface of the AM particles are modeled based on stochastic principles and effects. Coupling these models to p2D or 3D models results in multi-scale modeling approaches where information from the macroscopic continuum models describing the operation of the LIB is used to model film formation. The coupling results in increased complexity and computational costs. [72]

2.3.2 Homogeneous electrochemical model¹

The homogeneous physicochemical battery model implemented here is based on the work of Doyle, Fuller, and Newman [65, 66]. In the classical model, a homogenized pseudo 1D+1D (p2D) approach is used to describe the reaction kinetics and transport processes by a set of coupled partial differential equations (PDE). In Figure 2.6, the considered processes and spatial dimensions for the classical model approach are displayed. Discretization is implemented in the x-direction from anode to cathode and in the radial direction in the AM particles from center to surface.

In this work, the classical model and a higher discretized model are used. In the case of the latter one, the electrode is discretized in three dimensions (x, y, z), resulting in a 3D+1D (p4D) representation. In the following, the equations for the p4D approach are introduced. The considered physical processes, and thus the solved PDEs are similar to the classical model, but the spatial discretization differs. The model equations are not derived, but only briefly introduced. For detailed information about the model approach, readers can refer to [67, 74].

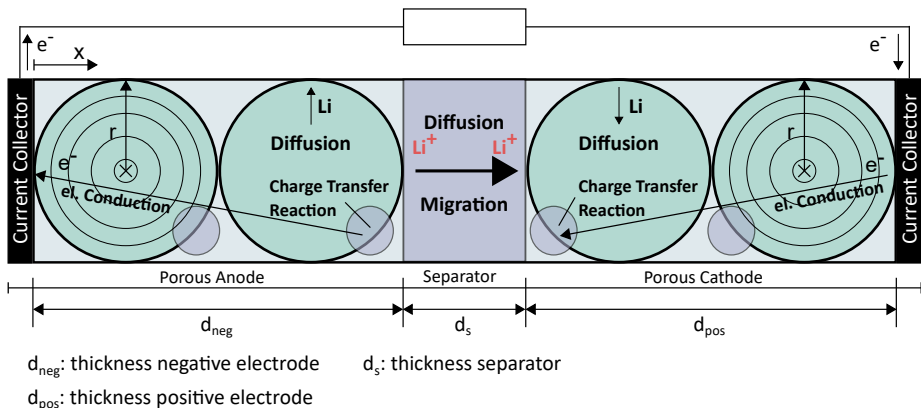


Figure 2.6: Pseudo 1D+1D model for a lithium-ion battery.

¹ Part of this chapter has been published in (Schmidt et al., ACS Appl. Energy Mater. 2021, 4, 5, 4845–4860, 2021 [73])

The main governing model equations are summarized in Table 2.1. The equations are classified concerning the macro kinetics by eqs. 2.4-2.7 and the micro kinetics are given by eqs. 2.8-2.9. Further relevant equations and the respective boundary conditions are listed in eqs. 2.10-2.18. Solving the coupled PDE system enables to estimate the time-dependent state variables for the ionic concentration in the electrolyte c_e , the lithium concentration in AM particles c_s , the potential of the electrolyte phase ϕ_e and the solid phase potential ϕ_s . In the following the physical relationship of these variables is briefly explained and further necessary quantities and equations are introduced.

In the model, a dual intercalation cell is implemented with the following reaction at both electrodes (detailed half-cell reactions are listed in Chapter 2.1.1):



with Li_s as intercalated lithium and Θ_s as an intercalation vacancy at the surface of the solid particles. The electron e_s^- is in the electrical conducting phase of the electrode [74].

The volume rate of the charge-transfer reaction j^{Li} is modeled with the Butler-Volmer equation, see eq. 2.8 in Table 2.1. The exchange current density i_0 is calculated based on eq. 2.9. It considers the reaction rate constant and the total number of sites available in the AM particles and the electrolyte, by evaluating the respective concentrations [74]. Furthermore, the volume rate of the reaction is driven by the local overpotentials defined as

$$\eta = (\phi_s - \phi_e) - E^{\text{eq}}, \quad (2.20)$$

where E^{eq} is the equilibrium potential that depends on the intercalated lithium concentration at the surface of the AM particles [74]. The active surface area a_s in the electrode is described by a volume-averaged effective value defined as [67]:

$$a_s = \frac{3 \cdot (1 - \varepsilon_e)}{R_p}, \quad (2.21)$$

with the particle size R_p and the porosity ε of the electrode microstructure.

The estimated reaction fluxes j^{Li} at the surface of the particles serve as the boundary condition for the mass transport in the AM, described in eq. 2.13 and as source term in eq. 2.6 for the ionic mass transport in the electrolyte. At the AM particle surface a double layer is considered, see eq. 2.10 and 2.11 [67].

The mass and charge conservation in the solid and liquid phases is ensured by eqs. 2.4-2.7. In the liquid phase, the mass and charge transport is represented by homogenized transport coefficients defined as

$$D_{e,\text{eff}} = \frac{\varepsilon_e}{\tau} D_e \quad (2.22)$$

Table 2.1: Governing equations for 3D+1D (P4D) electrochemical model. [67, 74]

Equations

Macro Kinetics:

$$\frac{\partial c_s}{\partial t} = \frac{1}{r^2} \cdot \frac{\partial}{\partial r} \left(D_s \cdot r^2 \cdot \frac{\partial c_s}{\partial r} \right) \quad (2.4)$$

$$j^{\text{tot}} = \nabla \cdot (\kappa_{s,\text{eff}} \cdot \nabla \phi_s) \quad (2.5)$$

$$\epsilon_e \frac{\partial c_e}{\partial t} = \nabla \cdot (D_{e,\text{eff}} \nabla c_e) + (1 - t_p) \cdot \frac{j^{\text{Li}}}{F} \quad (2.6)$$

$$j^{\text{tot}} = -\nabla \cdot \left(\kappa_{e,\text{eff}} \nabla \phi_e - 2 \frac{RT}{F} (t_p - 1) \cdot \kappa_{e,\text{eff}} \cdot \nabla \ln c_e \right) \quad (2.7)$$

Micro Kinetics:

$$j^{\text{Li}} = a_s i_0 \left(\exp \left(\alpha \frac{\eta F}{RT} \right) - \exp \left((1 - \alpha) \frac{\eta F}{RT} \right) \right) \quad (2.8)$$

$$i_0 = k_{\text{ct}} F (c_e)^\alpha (c_{s,\text{max}} - c_s)^\alpha (c_s)^{(1-\alpha)} \quad (2.9)$$

Further Equations:

$$j^{\text{tot}} = j^{\text{DL}} + j^{\text{Li}} \quad (2.10)$$

$$\frac{\partial (\phi_s - \phi_e)}{\partial t} = \frac{j^{\text{DL}}}{a_s C_{\text{DL}}} \quad (2.11)$$

$$U_{\text{cell}} = \phi_s(L) - \phi_s(0) \quad (2.12)$$

Boundary Conditions

Solid Phase:

$$\frac{\partial c_s}{\partial r} = \frac{j^{\text{Li}}}{a_s F}, \quad r = R_p \quad (2.13)$$

$$\frac{\partial c_s}{\partial r} = 0, \quad r = 0 \quad (2.14)$$

$$\frac{\partial \phi_s}{\partial x} = \frac{-i_{\text{cell}}}{\kappa_{s,\text{eff}}}, \quad x = \{0, L_{\text{cell}}\} \quad (2.15)$$

$$\frac{\partial \phi_s}{\partial x} = 0, \quad x = \{d_{\text{neg}}, L_{\text{cell}} - d_{\text{pos}}\} \quad (2.16)$$

Liquid Phase:

$$\frac{\partial c_e}{\partial x} = 0, \quad x = \{0, L_{\text{cell}}\} \quad (2.17)$$

$$\frac{\partial \phi_e}{\partial x} = 0, \quad x = \{0, L_{\text{cell}}\} \quad (2.18)$$

and

$$\kappa_{e,\text{eff}} = \frac{\varepsilon_e}{\tau} \kappa_e, \quad (2.23)$$

with D_e being the diffusion coefficient and κ_e the ionic conductivity of the liquid electrolyte. The impact of the porous electrode structure is considered with the Bruggeman relation by taking the porosity ε and tortuosity τ of the electrode structure into account. The electrical charge transport in the solid phase is described by Ohm's law and the porous structure is considered with the effective electrical bulk conductivity written as

$$\kappa_{s,\text{eff}} = \varepsilon_s \cdot \kappa_s. \quad (2.24)$$

Based on the solid-state potentials at the current collector of the electrodes, the cell voltage during the charge/discharge process can be derived by eq. 2.12. The energy density of the battery cell is estimated by integrating the product of current and voltage over the discharge time.

2.4 Uncertainty quantification

In the fundamentals, interactions between manufacturing, electrode structure, and electrochemical performance were already discussed. In reality, it must be taken into account that the manufacturing process is subject to deviations, as tolerances in the processes affect the battery structure and do not allow a discrete product [14, 59]. The arising uncertainties propagate and affect the electrochemical performance and the aging behavior. Applying methods regarding uncertainty quantification (UQ) to physical battery models allows studying the impact of product uncertainties, which is in the scope of this dissertation.

Methods of UQ have been applied successfully for a wide range of computational models. For example, it has been applied in chemical engineering [75, 76]. Applications related to chemical engineering are of special interest here, due to its proximity in terms of manufacturing and operation of LIBs. In the field of chemical process models, methods of uncertainty quantification have been used to efficiently determine parameter sensitivities and, based on this, perform robust process optimization in pharmaceutical manufacturing [77, 78]. In the context of lithium-ion battery modeling, UQ has been used to determine parameter sensitivities, by implementing point estimate methods and polynomial chaos expansion [15, 16, 79].

The homogeneous electrochemical p2D model was derived for discrete input parameters. If the propagation of uncertainties is to be analyzed these parameters must be represented by a random vector described by a probability density function (PDF). The challenge is to evaluate the effect of these uncertain parameters and estimate the parametric sensitivities. In this work, two different methods are applied: (I) the Monte-Carlo (MC) approach and (II) the polynomial chaos

expansion (PCE). The MC method is sample-based and rather simple. The parameter space is mapped with random samples and every sample point is calculated individually in the model. Hence, the computational costs are high due to an excessive number of model calls [80]. In contrast, the PCE is a fast-to-evaluate polynomial surrogate model mapping the model output. The number of model calls for generating the PCE is reduced compared to the MC approach. The polynomial nature of these surrogates results in low calculation times for evaluation. Hence, the PCE is of particular interest for optimization. In the following, the generation of the PCE is discussed. Then Sobol' indices are introduced as a measure of parametric sensitivity.

In this work, uncertainty quantification is implemented with UQLab, an open-source MATLAB-based software framework for uncertainty quantification with a focus on academic research [81]. The fundamentals are briefly summarized based on the manuals available for the UQLab framework [82, 83]. This ensures the introduction of later implemented and used methods. The fundamentals are slightly extended with relevant literature.

2.4.1 Polynomial chaos expansion

The PCE was introduced in the 1930s by Wiener et al. [84]. The method was defined for solving stochastic finite element problems in various engineering applications. The classical approach was constructed for standard normal variables but has since then been generalized for other standard random variables, e.g., uniform or beta distributions. The goal is to replace the expensive-to-evaluate computation model with inexpensive-to-evaluate surrogates and thus provide an efficient tool for estimating stochastic problems. The metamodel provides a functional approximation of the computational model through a spectral representation on a suitably built basis of polynomial functions. In the following it is briefly described how the basis and the coefficients of the PCE are estimated. For detailed information it is referred to the previously mentioned technical reports of UQLab [82], Sudret et al. [80], Xie et al. [75], and Wiener et al. [84], all providing the information summarized here.

We assume a random vector with independent components $\mathbf{X} \in \mathbb{R}^M$ described by a probability density function (PDF) f_X and a finite variance computational model $H(\mathbf{X})$. The PCE of this mathematical model is defined as:

$$Y = H(\mathbf{X}) = \sum_{\alpha \in \mathbb{N}^M} y_\alpha \psi_\alpha(\mathbf{X}) \quad (2.25)$$

where $\psi_\alpha(\mathbf{X})$ are multivariate polynomials, $\alpha \in \mathbb{N}^M$ is an index identifying the number of components of the polynomials, and y_α are the corresponding coefficients of infinite degree. The

multivariate polynomials $\psi_\alpha(\mathbf{X})$ are constructed by a set of univariate orthonormal polynomials $\xi_k^{(i)}(x_i)$ which satisfy the definition of orthonormal polynomials defined as:

$$\langle \xi_j^{(i)}(x_i), \xi_k^{(i)}(x_i) \rangle = \int_{\mathcal{D}_{X_i}} \xi_j^{(i)}(x_i) \xi_k^{(i)}(x_i) f_{X_i}(x_i) dx_i = \delta_{jk} \quad (2.26)$$

here i describes the input variable, j and k the polynomial degree, $f_{X_i}(x_i)$ is the i^{th} -input marginal distribution and δ_{jk} is the Kronecker delta. It is equal to 1 if j and k have identical values and 0 otherwise.

The multivariate polynomials $\psi_\alpha(\mathbf{X})$ are defined by the product of the univariate parts:

$$\psi_\alpha(\mathbf{x}) = \prod_{i=1}^M \xi_{\alpha_i}^{(i)}(x_i) \quad (2.27)$$

The orthonormality of the univariate polynomials results in also orthonormal multivariate polynomials.

The probability distribution of the random variables defines the families of univariate orthonormal polynomials. For example, Gaussian random variables are mapped with Hermite polynomials. As stated above, the PCE has been extended in the recent years to also map other types of statistical distributions. The Beta distribution, for example, can be represented by Jacobi polynomials. If the input random variables are not independent, or no standard polynomials are defined for their distribution, the PCE can be adapted by performing an isoprobabilistic transform, or computation of a custom set of polynomials. However, this is not discussed in detail here.

For realistic applications, the sum in eq. 2.25 needs to be reduced to a finite sum to approximate the random variables

$$Y = H(\mathbf{X}) \approx \sum_{\alpha=0}^{P-1} y_\alpha \psi_\alpha(\mathbf{X}) \quad (2.28)$$

here P is the dimension of the polynomial basis and it depends on the maximum order p_{max} and the dimension of the input variable ($n_{\mathbf{X}}$). The optimal solution of the order is a trade-off between the lowest possible value providing a target accuracy.

Beside the definition of the multivariate polynomials, the estimation of the coefficients y_α is essential for the PCE. This is mostly done by methods that can be divided into two groups: (I) intrusive methods and (II) non-intrusive methods. The intrusive methods, e.g., Galerkin projection, are characterized by high accuracy but the computational model needs to be adapted and this can be challenging for complex models solving a system of PDEs. In comparison, the non-intrusive methods estimate the coefficients based on post-processing of the model evaluations and can thus be applied for models of different complexity. In this work, only non-intrusive methods based on regression are applied. More specific, only the least angle regression (LAR) is used in this work. The LAR is suggested as stable and efficient solution and was applied in the context of PCE by Blatman et al. [85]. It is a linear regression tool and based on least-square

minimization but modified by adding a penalty term. However, different methods are possible and may have certain advantages for different scopes.

By defining the polynomial basis and the coefficients the PCE is able to represent the output of the computational methods with a defined set of polynomials.

2.4.2 Sensitivity analysis

The sensitivity analysis (SA) aims to describe how the variability of the model response $Y = H(\mathbf{X})$ is affected by the variability of the single input variables or a combination of these. The SA is especially of interest to rank the parameters according to their importance and the information can, e.g., be used to reduce the dimension of the model. The SA treats the model as a black box and sensitivity is only evaluated based on the model response for a certain sample of inputs. In general, sensitivity methods aim to reduce the number of model evaluations by implementing efficient approaches. In the following, a brief introduction concerning SA and methods for estimation of sensitivity indices are presented. The following information is taken from the literature. Detailed description of the methods can be taken from the technical report of UQLab, and Xie et al. [75, 83].

In general, SA can be divided into: (I) local sensitivity analysis, and (II) global sensitivity analysis. In local SA the sensitivity is evaluated based on the derivative at the nominal value and only small step changes close to this nominal value are considered. This allows simple implementation and interpretation and a reduced number of model evaluations. However, only a single parameter point is considered and information concerning the entire parameter space and parameter interactions are neglected. The global SA considers the entire parameter space and this allows for more rigorous definition and capability of describing influence from parameter interactions. In this work the global SA is applied for analyzing the effect of manufacturing induced uncertainties on the electrochemical performance. This allows to screen a wide parameter range and consider parameter interactions. More precisely, the Sobol' sensitivity analysis is implemented and applied in this thesis. Basic information concerning this method is provided in the following.

The Sobol method is a variance-based approach and the estimation of the Sobol' indices is based on the idea of defining the expansion of the computational model into summands of increasing dimension. Hence, the total variance of the model is described in terms of the sum of the variances of the summands. This method is referred to as ANOVA (ANalysis Of VAriance) and assumes independent input variables.

The stochastic version of a model is represented as

$$Y = H(\mathbf{X}), \quad (2.29)$$

the model input \mathbf{X} is a random vector, characterized by a joint probability density function. The Sobol' decomposition of this model $H(\mathbf{X})$ is given by

$$H(\mathbf{X}) = H_0 + \sum_{i=1}^M H_i(x_i) + \sum_{1 \leq i < j \leq M} H_{ij}(x_i, x_j) + \cdots + H_{1,2,\dots,M}(x_1, \dots, x_M). \quad (2.30)$$

Based on this decomposition the total variance of function $H(\mathbf{X})$ can be deduced and is written as

$$\text{Var}(Y) = \sum_{i=1}^M V_i + \sum_{1 \leq i < j \leq M} V_{ij} + \cdots + V_{1,2,\dots,n}. \quad (2.31)$$

$\text{Var}(Y)$ is the total variance of function $H(\mathbf{X})$ and V_i , V_{ij} , and $V_{1,2,\dots,n}$ are partial variances related on the effects of individual parameters or parameter interactions on $\text{Var}(Y)$.

The first-order Sobol' index represents the relative contribution of each group of variables and is defined as the ratio of the partial variance to the total variance. This is shown in eq. 2.32.

$$S_i = \frac{V_i}{\text{Var}(Y)} \quad (2.32)$$

The index is estimated for one input variable x_i and only represent the effect of this variable. The higher-order Sobol' indices S_{ij} represent the effect of multiple-term indices, e.g., $S_{i,j}$, $i \neq j$ and are defined by

$$S_{ij} = \frac{V_{ij}}{\text{Var}(Y)}. \quad (2.33)$$

The higher order indices consider the interaction of the variables x_i and x_j and they cannot be decomposed into the contribution of those variables separately.

The total Sobol' index of the input variable x_i is defined as the sum of all Sobol' indices including contributions of the single variables and their interactions and is denoted as S_i^T

$$S_{Ti} = \frac{V_i + V_{ij} + \cdots + V_{1\dots i\dots M}}{\text{Var}(Y)}. \quad (2.34)$$

The Sobol' indices can be calculated based on various methods. The most common is the Monte Carlo-based estimation. It creates random values dependent on a given stochastic distribution. The estimation requires a cumbersome amount of model calls and evaluations. The PCE presented in Section 2.4.1 is also capable to estimate the Sobol' indices. The advantage here is that the computational effort is less, since the Sobol decomposition can be estimated analytically based on the PCE coefficients. Due to the focus in this work on the PCE, the estimation of the Sobol indices for this method is briefly discussed in the following.

Continuing from the equations presented in Section 2.4.1 concerning the PCE, now a truncated PCE with a random variable \mathbf{X} is assumed

$$H_{\mathbf{u}}(\mathbf{X}_{\mathbf{u}}) \approx \sum_{\alpha \in A_{\mathbf{u}}} y_{\alpha} \psi_{\alpha}(\mathbf{x}), \quad (2.35)$$

where $A_{\mathbf{u}} \subset A$ and is defined as:

$$A_{\mathbf{u}} = \{\alpha \in A : \alpha_i \neq 0 \leftrightarrow i \in \mathbf{u}, i = 1, \dots, M\}. \quad (2.36)$$

The mean and variance of the function $H(\mathbf{X})$ can be directly obtained from the coefficients of the PCE:

$$E_{Y,A} = y_0 \quad (2.37)$$

$$V_{Y,A} = \sum_{\alpha \in A, \alpha \neq 0} y_{\alpha}^2 \quad (2.38)$$

Following this representation, the Sobol sensitivity indices can easily be calculated with:

$$S_{\mathbf{u}} = \frac{1}{V_{Y,A}} \sum_{\alpha \in A_{\mathbf{u}}} y_{\alpha}^2, \quad (2.39)$$

where $S_{\mathbf{u}}$ is either the first order sensitivity if \mathbf{u} contains only one element, or an interaction sensitivity if it contains more than one. The total sensitivity indices can be calculated with:

$$S_{T_i} = \frac{1}{V_{Y,A}} \sum_{\alpha \in A_i} y_{\alpha}^2, \quad (2.40)$$

where $A_i \subset A$ and includes all basis polynomials related to x_i :

$$A_i = \{\alpha \in A \mid \alpha_i \neq 0\} \quad (2.41)$$

Part 1 - Uncertainties from Electrode Production

3 Modeling Process-Product Interdependencies in Battery Production²

3.1 Introduction

The production aims to establish the electrode and cell design defined in the development. The challenge is to meet the specified structural parameters with high accuracy and reduced deviations to ensure the desired cell performance within a defined uncertainty range [9]. Understanding relationships between the individual production processes, electrode structure, and electrochemical performance is critical for producing batteries with high and consistent quality [88].

It is necessary to understand cause-effect relations within single process steps and along the consecutive production chain. The processes reveal strong interactions as the intermediate product is continuously transferred and adapted. Changes in one process might affect the following [88]. That could be a direct interaction of consecutive processes, e.g., the coating process is affected by the rheological properties of the slurry generated in the mixing process [9, 89]. Furthermore, interactions can occur between processes not directly coupled. The electrolyte filling is affected by the electrode microstructure and thus by the drying and calendaring process [90, 91]. The correlations between the applied process parameters and the resulting structural parameters are important to describe and evaluate the production process. However, the LIB is not fully characterized by design but rather by electrochemical performance. Hence, improving the production process is only reasonable if the impact of the cell design on the performance is considered. In particular, evaluating uncertainties that arise in the process steps is only sufficient if it can be determined how the resulting structural deviations affect the electrochemical performance.

It follows that the holistic consideration of the process-structure-property relation enables knowledge-driven production optimization [88]. That holds the potential to lower costs, improve cell quality,

² Part of this chapter has been published in: Thomitzek, Schmidt, Röder, Krewer, Herrmann, Tiede, *Procedia CIRP*, 2018 [86], and Thomitzek, Schmidt, Silva, Karaki, Lippke, Krewer, Schröder, Kwade, Herrmann, *Sustainability*, vol. 14, no. 3, 2022 [87]

and reduce scrap rates. Solely, experimental-based analyses are not feasible to estimate the effects of all parameter correlations. Due to the large number of parameters being considered, multiple experiments on single process levels and the coupled process chain would be necessary. Establishing a platform that integrates mechanistic models for every production step can contribute to storing the currently known correlations and identifying white spots. Furthermore, model-based analysis enables studying various parameter sets in a reduced amount of time and at lower costs. Consequently, there is a demand for a model-based framework that allows a non-invasive improvement of the battery cell and its production chain to further continue the emergence of a battery-driven mobility and energy sector by strengthening sustainability and cost-effectiveness.

Establishing a platform that considers both the process-structure and structure-property relations requires coupling modeling approaches from the field of process engineering with that of electrochemical systems. In literature, examples for coupling these two approaches already exist. Ngandjong et al. [92] applied a multiscale simulation platform to understand the formation of various electrode structures and to enable a detailed prediction of the electrochemical performance. Further, Chouchane et al. [93] used the platform to investigate the impact of carbon-binder spatial location on the electrochemical performance properties. In both works, the focus is on highly resolved model approaches for studying selected physical effects of the electrode microstructure in detail, and the impact of the process parameters on the structural parameters is not studied in detail.

In this work, a coupled model approach is introduced as a framework integrating mechanistic models for every production step and the operation of LIBs. That holistic approach is later referred to as the digitalization platform. The complexity of the implemented models can be adapted depending on the scope being addressed. The approach enables a virtual representation able to determine the effect of production on battery cell performance. Thus, the framework can analyze correlations along with the production. It allows rating the impact of production processes and structural parameters on the electrochemical performance of the LIB. In this chapter, the approach is introduced by defining assumptions and requirements for the consisting models. In Chapters 4 and 5, the framework is applied and used to analyze the impact of production uncertainties and subsequently to establish a knowledge-driven optimization approach to estimate a robust electrode design while considering the effect of uncertainties.

3.2 Computational methods: The framework

The digitalization platform is a flexible framework enabling one to understand, visualize and analyze correlations concerning the production process and its impact on the product performance.

That includes correlations within the production chain and correlations between the production process and the electrochemical performance of the product. To map these, the platform consists of three parts: (I) the process chain model, (II) the battery cell model, and (III) the analysis module. In Figure 3.1, the structure is visualized. The coupled framework [86, 87] was jointly developed with Matthias Thomitzek (IWF, TU Braunschweig), with the process chain model being established and implemented by Thomitzek and the battery cell model by me. For better understanding, also the process chain model will be introduced in the following pages.

The platform is based on the process-structure-property relation established by Bockholt et al. [88]. The process-structure dependency is modeled based on mechanistic cause-effect relations within (I) the process chain model. The approach of a process chain model for battery production is taken from Schönemann et al. [94]. The estimated structural parameters are forwarded to (II) the battery cell model for evaluating the structure-property relation. Coupling the two approaches covers the whole process-structure-property relation. Here, the structural parameters also contain information regarding the materials.

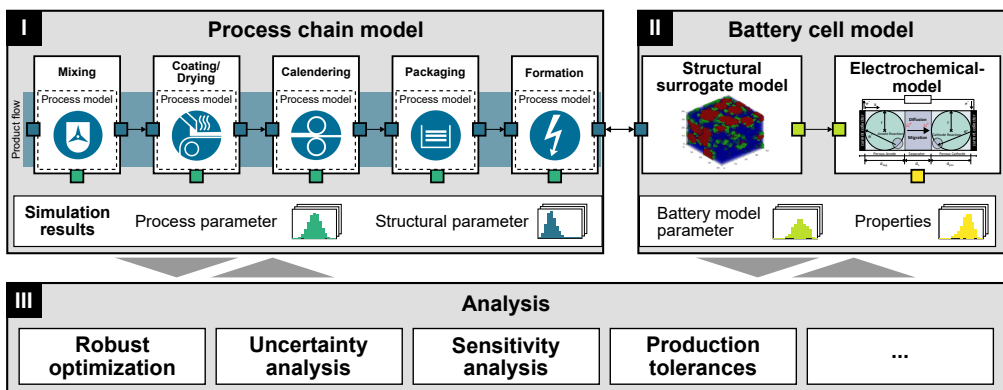


Figure 3.1: Concept of the digitalization platform. It consists of three modules: (I) process chain model, (II) battery cell model, (III) analysis module. [87]

The holistic consideration of various parameters and correlations ensures an *in silico* analysis of process-product interactions. In this thesis, the focus is on uncertainty quantification and propagation. These uncertainties are induced by tolerances in each production step or based on stochastic processes occurring in the steps (e.g., evolving of the porosity). Furthermore, the framework allows for robust design optimization and to identify sensitive parameters. All these aspects are considered in (III) of the analysis module. This module is coupled to (I) and (II) and has access to all parameters.

3.2.1 Process chain model

In Chapter 2.2, it was discussed that the production of lithium-ion batteries consists of single process steps coupled with each other. In the beginning, the raw materials are given into the mixing process. Along with the production steps, an electrode is created, which changes its structure in each step until it reaches its final structure. The electrodes are then assembled into battery cells.

The process chain model (work by Thomitzek [86, 87]) is a mathematical representation of the production process considering the individual steps. For each process, a model is implemented. It describes the correlations between the structural parameters of the input, the process parameters, and the structural parameters of the output. The structural parameters specified here also contain information regarding material properties. Coupling the individual process steps in the process chain model enables studying the propagation of uncertainties, and the interaction between the process steps. It is important to note that not all structural properties of the electrodes are altered in every production process. Structural parameters may remain unchanged over several steps. At the same time, new structural parameters may appear. For example, the porosity of the electrode emerges after the solvent evaporates in the drying process. Figure 3.2 displays an exemplary process chain model for mixing, coating, and drying. The structural parameters are changed depending on the applied process parameters. Furthermore, it is indicated that new structural parameters are created or parameters pass unchanged.

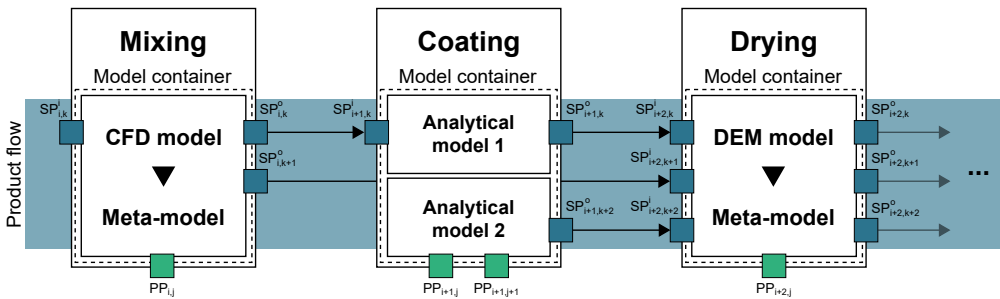


Figure 3.2: Exemplary process chain model implemented by coupled model containers. They are connected via structural parameters. The process chain is reduced and only exemplary models are presented for mixing, coating, and drying. [87]

The process models incorporated in the process chain model are defined as containers. The specific type of models is not defined. The only requirement is that the impact of the production process on the product structure must be described. Depending on the scope and the desired complexity, different models can be implemented. The simplest approach is an analytical model. It is a top-down description of the process mechanisms and can be quickly solved. It can be applied for various processes along the process chain and is either a first principle equation [95]

or derived from experiments [96, 97]. However, the physical correlations are not represented in detail, resulting in poor predictability. Increasing the complexity can be done by applying DEM, CFD, or FEM models for the process steps. DEM simulations are used to understand and optimize the physical processes in the dry mixing and the calendering process [98–100]. The CFD model is used for the electrolyte filling to understand how the wetting time is affected by the electrode microstructure and the cell stack. Implementing FEM models is possible for the stacking process. These highly resolved models have an advantage in terms of predictability. At the same time, however, they have higher computation time, and implementing a wide variety of software in the process chain model is challenging.

In order to correctly predict the influences of the production processes on the electrode structure and also to map the interactions along the process chain, detailed parameterization is necessary. For this purpose, the process models must be validated and parameterized individually. In the next step, however, the process chain model must also be examined and validated to ensure that the interactions between the individual processes are correctly mapped.

3.2.2 Battery cell model

In Chapter 2.3.1, an overview is provided of various modeling approaches suitable for representing the operation of LIBs. In general, all model types can be implemented in the digitalization platform. However, the process chain model calculates various structural parameters, and based on these the battery cell model must estimate the electrochemical performance. The implemented model must predict the impact of the manufactured battery structure on the physical processes and performance. Empirical models are therefore not suitable for the digitalization platform. The battery cell model must be based on physical correlations to enable reliable prediction of performance with varying structural parameters.

In this work, the p2D model is selected and implemented as the battery cell model in the digitalization platform. The model was described in detail in Chapter 2.3.2. In addition, Figure 3.1 indicates that the p2D model can be extended by structural surrogate models. These can be included to improve the predictability of the p2D model by estimating selected effective parameters defining the transport and the reaction kinetics in the electrode. In the p2D model, the impact of the microstructure is modeled with volume averaged effective kinetic parameters (e.g., $D_{e,eff}$, $\kappa_{e,eff}$, a_s). The classical estimation of these effective parameters with the Bruggeman relation lacks in predictability [26, 33]. Implementation of structural surrogate models based on artificial electrode structures can lead to improved prediction of these effective parameters, allowing the effects of deviations in electrode microstructure on kinetic processes to be estimated with higher accuracy [27]. The structural surrogate model is not mandatory in the battery cell model. In Chapter 4, solely the classical p2D model approach is applied. In Chapter 5, the model is extended to include the surrogate models, and therefore they are discussed in detail there.

Nevertheless, the battery cell in the digitalization platform is designed as a container. It is not limited to the p2D model. It could also be a three-dimensional battery model considering the heterogeneous electrode micro structure in detail. However, the estimation of uncertainties and the resulting cumbersome amount of model runs do not support the high-resolution battery model due to high computation times. Furthermore, the full-3D model requires a detailed reconstruction of the electrode microstructure. The implemented process chain model is not able to provide this.

3.2.3 Analysis module

The analysis module consists of several mathematical methods that can be applied to the coupled model approach. It has access to all parameters considered within the digitalization platform. Thereby a knowledge-driven assessment is possible. In particular, the analysis of uncertainties is covered in the analysis module. Methods for sensitivity analysis, uncertainty quantification, and robust optimization can be implemented. That enables the identification of sensitive process parameters, optimization of process-induced tolerances, or a robust design of the LIB to reduce the scrap rate and lower the deviation of the quality-related parameters. However, the analysis module can be used to implement mathematical methods for classical optimization and various other topics depending on the scope of the study.

3.3 Concluding remarks

The digitalization platform couples the model-based consideration of the production steps and the electrochemical modeling of the final product in a single framework. It enables studying the impact of the production on the performance of the LIB directly. The focus of developing that method was on evaluating the impact of uncertainties. Those are induced in the single process steps, propagate along the process chain, and affect the electrochemical performance. Enabling that can only be achieved by computationally efficient modeling approaches. That is the advantage of the method compared to common approaches available in the literature. Considering correlations between various parameters allows quantitative evaluation in terms of parameter sensitivity, uncertainty propagation, and robust optimization. That enables knowledge-driven improvements in battery production. The single models are defined as containers and can be replaced with models of varying complexity. Simple analytical equations, data-driven models, and multidimensional and multiphysics models are possible. Choosing the respective models defines the complexity and computational costs of the platform and must be selected depending on the scope.

Based on the approach presented here, specific analyses will be carried out in the further course of the work. In the following chapters, exemplary models are selected and implemented into the framework, and analysis concerning the uncertainty propagation (see Chapter 4) and robust optimization (see Chapter 5) are conducted and discussed.

4 Impact of Production Induced Uncertainties on Battery Performance³

4.1 Introduction

In this chapter, the digitalization platform introduced in Chapter 3, is applied to study the impact of production-related uncertainties on the electrochemical performance of the LIB. The focus is on coating, drying, and calendaring as consecutive production steps. The chapter provides insights into how the digitalization platform can be used to identify sensitive production steps by considering the process-structure-property relations.

Process-induced tolerances in the production of LIBs result in structural uncertainties on the electrode and cell level [59]. Additionally, natural deviations can be induced by the processes, e.g., the formation of the porous microstructure in the drying process, resulting in local inhomogeneity. The uncertainties in structural parameters lead to deviations of the electrochemical properties, which cause deviations in cell level and affect the lifetime and overall performance. An et al. [12] presented an experimental-based analysis of cell-to-cell deviations. The rate dependence of these deviations was studied with a statistically relevant amount of commercial cells, focusing on the correlation of capacity vs. weight and capacity vs. resistance and kinetics. For low rates of 0.2 C, a nearly linear correlation with the cell weight was identified. Increasing the rate leads to a more non-linear behavior due to the increased effect of the kinetics. Experimental work that investigates process uncertainties is rare since it requires a significant amount of manufactured cells and a high number of electrochemical measurements.

The application of mathematical models can reduce the experimental effort and thus cut costs and time. In literature, several studies exist focusing on the effect of uncertain structural parameters on electrochemical performance. Santhanagopalan et al. [13] analyzed the influence of cell-to-cell deviations on impedance. The effect of structural parameters of different components on the cell impedance was analyzed and the sensitive parameters and components were identified. Nan

³ Part of this chapter has been published in Schmidt, Thomitzek, Röder, Thiede, Herrmann, Krewer, J. Electrochem. Soc.,167(6),060501, 2020 [101]

et al. [79] conducted a polynomial chaos expansion (PCE) based sensitivity analysis with a 3D multiphysics model of a multilayer cell. It was concluded that the cell discharge capacity and the thermal behavior at 1 C are most sensitive to the electrode parameters and their pore structure. Hadigol et al. [16] studied the effect of parametric model uncertainties on the cell capacity, voltage, and concentrations. The focus was on a limited number of structural parameters, e.g., porosity, particle size, Bruggeman coefficient, and various kinetic parameters. Laue et al. [15] studied the influence of cell-to-cell deviations and subcell deviations. It was concluded that subcell deviations, i.e., deviations within a single electrode sheet, have a significant impact on the overall cell behavior. However, the influence of the production processes on the examined structures was not taken into account. This impedes a consecutive consideration of the propagation of uncertainties from the machine-defined process parameters to the evolving structural parameters and the electrochemical properties.

In the previous chapter, the digitalization platform was introduced as a framework considering the process chain and the operation of the LIB by a coupled model approach. This enables studying the impact of process-induced uncertainties and their propagation throughout the process chain and rate the effect on electrochemical performance. Thus, sensitive process parameters can be identified. Studying the propagation of uncertainties requires a computationally efficient framework. In this chapter, the digitalization platform is applied with analytical models and a homogenized p2D model for the operation of the LIB. The analytical process models are widely developed in process engineering, e.g., by Mayer et al. [48] for the mixing and dispersing process and by Jaiser et al. [102] for the drying process. Homogenized battery cell models are frequently applied to study the impact of structural parameters on cell performance, which has been used, e.g., by Lenze et al. [103] to investigate the influence of the calendaring process, by Smekens et al. [104] to analyze the effect of the electrode density on the performance and by Kenney et al. [105] to study the impact of deviations in the structural parameters.

In this chapter, the impact of different uncertainty scenarios are analyzed based on the digitalization platform. Therefore, uncertainties are induced in the process models for coating, drying and calendaring. Due to the coupled approach, it is possible to track the propagation of uncertainties and rate the effect of uncertain process parameters on electrochemical performance. This allows identifying weak points in the production process, which is needed for knowledge-driven optimization.

4.2 Computational methods

In Chapter 3, the digitalization platform was introduced with flexible containers for the process chain model and the battery cell model. Here, analytical models taken from the literature are applied in the process chain model. They are introduced in the following.

The battery cell model is a p2D model which was already introduced in Chapter 2.3.2. The discretization in the electrolyte is only done in x-direction. The structural surrogate models mentioned in Chapter 3 are not applied. Relevant parameters for the battery cell model are estimated in Section 4.3 and listed there.

4.2.1 Process chain model

The process chain model was implemented by Thomitzek (IWF, TU Braunschweig). The process steps represented in the process chain model are the coating, drying and calendaring. The process models describe relevant process-structure relations for the respective process step. The selected process steps are successive. A propagation of uncertainties along the process chain can be determined. The models focus on the structural parameters coating thickness, coating density, porosity and tortuosity. Please see, Chapter 2.2 to get an overview of the production steps and other relevant parameters. Analytical models are applied to describe the single process steps. The models take the impact of single process parameter on changes in the structure of the intermediate product into account. Although reality is much more complex, they are sufficient as a first approximation to describe the cause-effect relations.

4.2.1.1 Coating model

The coating process defines slurry mass loading of the electrodes, e.g. via a blade gap operated process. The process model assumes a direct transfer of the height between the doctor blade gap and the current collector to the coating thickness. Based on the slurry composition the initial wet coating thickness d_0 can be determined (eq. 4.1). Further, the solid mass loading M_{solid} can be deduced (eq. 4.2).

$$d_0 = \frac{\rho_{\text{Slurry}}}{M_{\text{wet}}} \quad (4.1)$$

$$M_{\text{solid}} = M_{\text{wet}} - M_{\text{solvent}} = \frac{M_{\text{wet}}}{1 + X_{\text{solvent},0}} \quad (4.2)$$

ρ_{Slurry} , M_{wet} , M_{solid} , M_{solvent} and $X_{\text{solvent},0}$ are structural parameters of the electrode. They represent the density of the slurry after coating, the mass loading of the wet film after coating, the mass loading of solids and the solvent, and the liquid-to-solid ratio of the coating. d_0 is the process parameter during the coating which sets the initial wet coating thickness.

4.2.1.2 Drying model

In the drying process, the solvent is removed from the coated electrode. The drying process was modeled according to Jaiser et al. [102]. There, the authors assume a linear relation between drying time t and the decrease in coating thickness until the end of film shrinkage due to the constant drying rate \dot{m} . Eq. 4.3 determines the time until the end of film shrinkage is reached. The decreasing coating thickness was modeled using eq. 4.4. The solvent of the slurry evaporates steadily causing a decrease in film thickness. As the coating consolidates, pores start to empty. The coating thickness of the electrode after drying is modeled by eq. 4.5 [106]. The coating density initially increases until the end of film shrinkage is reached due to the decrease in coating volume but eventually decreases due to further solvent evaporation and the development of the porous structure. The coating density of the dry film can be determined by eq. 4.6.

$$t_{\text{EoFS}} = \frac{X_{\text{solvent},0} - X_{\text{solvent,EoFS}}}{\dot{m}} \cdot M_{\text{solid}} \quad (4.3)$$

$$d(t) = d_0 - \frac{d_0 - d_{\text{dry}}}{t_{\text{EoFS}}} \cdot t \quad (4.4)$$

$$d_{\text{dry}} = \frac{M_{\text{solid}}}{\rho_{\text{PM}} \cdot (1 - \epsilon_{\text{dry}})} \quad (4.5)$$

$$\rho_{\text{dry}} = \frac{M_{\text{solid}}}{d_{\text{dry}}} \quad (4.6)$$

t_{EoFS} , t and \dot{m} are process parameters. The parameters represent the time until the end of film shrinkage, the overall drying time and the drying rate. $X_{\text{solvent},0}$, $X_{\text{solvent,EoFS}}$, $d(t)$, d_{dry} , ρ_{PM} , ρ_{dry} and ϵ_{dry} are structural parameters of the coating describing the initial liquid-to-solid ratio after coating, the liquid-to-solid ratio at end of film shrinkage, the coating thickness during drying and after drying, the density of the particulate matter, the density of the dry coating and the initial porosity of the coating.

4.2.1.3 Calendering model

In the calendering process, the rolls of the calender compress the coating in order to reduce the coating thickness and adjust the structure of the porous composite. Meyer et al. [96] investigated the effect of the calendering process on electrode structure. The cause-effect relation between line load q_L and final coating density ρ_c (eq. 4.7) and final porosity ϵ_c (eq. 4.8) was modeled using exponential equations. The equations also require the compaction resistance γ_c of the coating in addition to the line load, the initial and maximum density (ρ_{dry} , ρ_{max}) and the initial and minimum porosity (ϵ_{dry} , ϵ_{min}). The compaction resistance is affected by the used material,

formulations, pore structure and roll temperature and can be fitted directly based on measured values using equations 4.7 or 4.8. Minimum porosity ε_{\min} and maximum density ρ_{\max} are determined according to equation 4.9 and 4.10 with ρ_{ph} being the physical density of the solid material [97, 106].

$$\rho_c(q_L) = \rho_{\max} - (\rho_{\max} - \rho_{\text{dry}}) \exp\left(-\frac{q_L}{\gamma_c}\right) \quad (4.7)$$

$$\varepsilon_e(q_L) = \varepsilon_{\min} + (\varepsilon_{\text{dry}} - \varepsilon_{\min}) \exp\left(-\frac{q_L}{\gamma_c}\right) \quad (4.8)$$

$$\varepsilon_{\min} = p \cdot \varepsilon_{\text{dry}} \quad (4.9)$$

$$\rho_{\max} = (1 - \varepsilon_{\min}) \cdot \rho_{\text{ph}} \quad (4.10)$$

The coating thickness after calendaring d_{el} is modeled using a mass balance approach before and after calendaring (eq. 4.11). The equation requires the coating thickness d_{dry} and the coating density ρ_{dry} before calendaring and coating density ρ_c after calendaring (provided by eq. 4.7).

$$d_{\text{el}} = \frac{\rho_{\text{dry}} \cdot d_{\text{dry}}}{\rho_c} \quad (4.11)$$

The approach assumes there is no elongation in lateral and forward direction during calendaring. Finally, tortuosity of the calendared electrode τ is acquired using the empirical Bruggeman relation (eq. 4.12) [107]. The Bruggeman parameter β_B was identified based on the differential effective medium approximation using a top and cross section electrode image by Ebner and Wood [108].

$$\tau = \varepsilon_e^{-\beta_B} \quad (4.12)$$

4.3 Model parameterization

In this part the implemented models are parameterized and validated. The aim of this step is to determine parameters in such a way that measurements can be mapped. For the process models, the process parameters need to be identified so that the structural parameters of the simulation match the structural parameters of the reference electrode. In the case of the battery model the electrochemical measurements were used to estimate kinetic and effective transport parameters for the battery model by identifying the simulation on the measurements with a least square algorithm approach.

4.3.1 Process chain model

The process chain model uses parameters from Jaiser et al. [102] and Meyer et al. [96, 97] for the coating, drying and calendering processes. The simulation was applied to produce cathodes with a mean coating thickness d_{el} of around $65\ \mu\text{m}$ and a porosity ϵ_{cal} of 0.31. Based on the process models and the parameters of the three processes, an initial wet coating thickness d_0 of $144.90\ \mu\text{m}$ was determined. Table 4.1 shows the process and structural parameters for the individual process steps. The standard deviations for the process parameters are based on data of the machines used in the work by Meyer et al. [96, 97]. The deviations of the drying rate \dot{m} and the drying time t do not affect the structural parameters since they are employed to predict the final film thickness only (see eq. 4.4). Thus, no standard deviations were considered for the drying rate and the drying time. The structural parameters were kept constant except for the porosity of the dried electrode ϵ_{dry} and the compaction resistance γ_c . The standard deviation for both parameters were set according to measurements in the Battery LabFactory Braunschweig.

Table 4.1: Input parameters for the process chain model.

	Process parameters		Structural parameters	
Coating	$d_0 / \mu\text{m}$	144.90 ± 2.04	$\rho_{\text{Slurry}} / \text{g cm}^{-3}$	2.715
			$X_{\text{solvent},0} / \text{kg kg}^{-1}$	1.00
Drying	$\dot{m} / \text{g m}^{-2} \text{s}^{-1}$	1.00 ± 0.00	$X_{\text{solvent,EoS}} / \text{kg kg}^{-1}$	1.00
			t / s	200
Calendering	$q_L / \text{N mm}^{-1}$	160 ± 11	$\epsilon_{\text{dry}} / -$	0.47 ± 0.2
			$\gamma_c / \text{N mm}^{-1}$	193.4 ± 4.3
			$p / -$	0.4
			$\rho_{\text{ph}} / \text{g cm}^{-3}$	4.40
			$\beta_B / -$	0.55

4.3.2 Battery cell model

Electrochemical experiments were conducted with a three-electrode setup. Therefor PAT-Cells from the EL-CELL GmbH were used. They use a cylindrical electrode with a diameter of 18 mm and a separator with an included lithium reference electrode. Graphite and NMC622 were used for the anode and cathode and were produced by the ZSW in Ulm, Germany. For each electrode the OCP curves were measured. The structural data of the electrodes are displayed in Table 4.2. The electrolyte was 1.0M LiPF_6 in EC:EMC (3:7 in weight) with 2wt% VC. The separator is

a glass fiber separator by EL-CELL GmbH (ECC1-00-0210-O/X). All experiments were conducted in an ESPEC SU-642 temperature chamber at $(25.0 \pm 0.3)^\circ\text{C}$. The assembled PAT-Cells were used to measure the electrochemical properties. The MACCOR 4000 test system was used to perform the formation of the cells and a discharge rate capability test. For the formation step, the cells were charged and discharged three times with a constant current step at 0.1 C in the voltage range of 2.9 V to 4.2 V. The discharge rate capability test was performed at three different discharge rates of 0.5 C, 1 C and 2 C in a voltage range from 2.9 V to 4.2 V.

In the first step of the parametrization, the OCP curves for the electrode materials are identified with the following Redlich-Kister approach [74]:

$$E_{\text{ref}}^{\text{eq}} = \frac{\Delta G_{33}^\circ}{F} + \frac{RT}{F} \ln \left(\frac{1 - X_{\text{Li}^+}}{X_{\text{Li}^+}} \right) + \frac{1}{F} \sum_{m=0}^N A_m \left[(2X_{\text{Li}^+} - 1)^{m+1} - \left(\frac{2mX_{\text{Li}^+}(1 - X_{\text{Li}^+})}{(2X_{\text{Li}^+} - 1)^{1-m}} \right) \right] \quad (4.13)$$

A least square algorithm is used to identify the Redlich-Kister coefficients A_m for the anode and cathode. The estimated coefficients are listed in Table A.1 (see appendix). The final set of parameters for the battery model is listed in Table 4.2. The adjusted parameters were defined with a least square based parametrization step. The kinetic model parameters were adjusted to represent the measurements with the simulation. The determined parameters were compared with the literature and are of a similar order of magnitude [27, 74, 105]. The electrical conductivity of the anode is below the usual values, however, in literature comparable results due to different causes in production and sample preparation are estimated [103]. The parameterized model is able to reproduce the electrochemical performance of the assembled lithium-ion batteries for the investigated discharge rates (see Figure A.1, appendix). Minor discrepancies between the simulation and the measurements may result from the homogenization of the electrode structure. This effect increases with an increasing discharge rate. Overall, the parameterized model is considered sufficiently accurate to map the measurements.

The parameterization and validation only apply to the reference point. Small scale deviations around the reference point can be represented, but with a reduced precision. This allows to realize the scope of the work, i.e., to study the general propagation and impact of minor uncertainties around a reference value for lithium ion battery electrode production.

Table 4.2: Battery model parameters used in the applied model. The diffusion coefficient in the electrolyte, ionic conductivity and transference number are dependent on electrolyte concentration.

Parameter	Symbol	Unit	Anode	Separator	Cathode
Layer thickness ^m	d_{el}	m	63.5×10^{-6}	100×10^{-6}	65.1×10^{-6}
Porosity ^m	ϵ	-	0.40	0.5	0.31
Particle size ^m	R_p	m	9.50×10^{-6}	-	5.00×10^{-6}
Tortuosity ^a	τ	-	2.09	1.0	1.896
Maximum concentration solid ^a	$c_{s,max}$	mol m^{-3}	32741	-	44949
Initial concentration solid ^a	c_0	mol m^{-3}	32132	-	17827
Initial concentration electrolyte ^a	c_e	mol m^{-3}	1200	1200	1200
Diffusion coefficient solid ^a	D_s	$\text{m}^2 \text{s}^{-1}$	3.75×10^{-12}	-	2.96×10^{-15}
Diffusion coefficient electrolyte ^c	D_e	$\text{m}^2 \text{s}^{-1}$	$f(c)$ [36]	$f(c)$ [36]	$f(c)$ [36]
Electronic conductivity ^a	κ_s	S m^{-1}	0.0116	-	6.8215
Ionic conductivity ^c	κ_e	S m^{-1}	$f(c)$ [36]	$f(c)$ [36]	$f(c)$ [36]
Transference number ^c	t_p	-	$f(c)$ [36]	$f(c)$ [36]	$f(c)$ [36]
Charge transfer coefficient ^s	α	-	0.5	-	0.5
Reaction rate constant ^a	k	-	1.36×10^{-8}	-	2.72×10^{-11}
Double layer capacity ^s	C_{DL}	F m^{-2}	0.2	-	0.2

^m measured by ZSW (department of production research)

^a adjusted

^s set, from ref. [67]

^c concentration dependence, see eq. in [36]

4.4 Definition of the case study

This section describes the case study applied to the model approach in this work. It was chosen in such a way that the effect of production tolerances, i.e., varying process parameters, on the structural parameters and the electrochemical properties of a lithium-ion battery can be studied. The case study is thus used to reveal the propagation and interactions of uncertain structural parameters along the consecutive process steps and study the influence of varying structural parameters on electrochemical properties. The models presented in section 4.2.1 and 2.3.2 are validated for the parameterized reference cell. The estimated uncertainties for the structural parameters and the electrochemical properties are not validated, but will be compared to literature.

For the case study, the previously presented process chain model with models for the coating, drying and calendaring processes is considered. Uncertainties are only taken into account for the production of the cathode, the anode parameters are kept constant. Four distinct production scenarios, illustrated in Figure 4.1, are discussed where each has a different combination of uncertainties along the production chain. The first scenario is defined as the nominal scenario, as

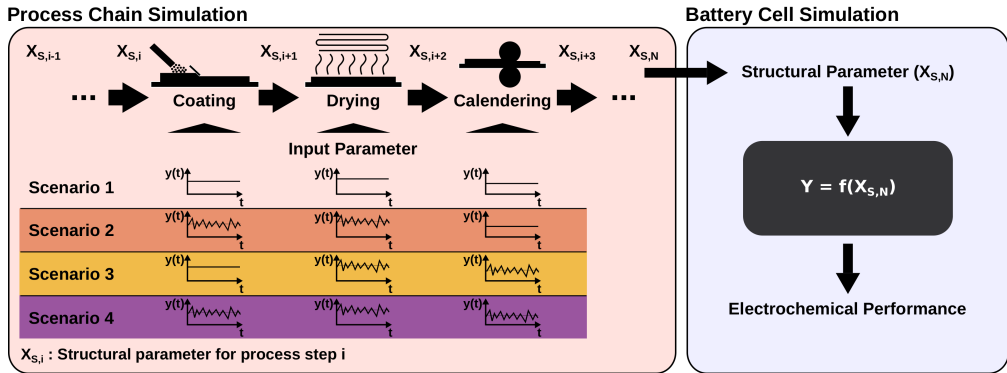


Figure 4.1: Displayed is the basic model approach and the scenarios that were simulated for the case study.

all processes are assumed to be free of process and parameter uncertainties in order to provide a reference scenario. In the other scenarios, the porosity after the drying process always varies because the formation of the electrode structure in the drying process is subject to natural deviation caused by the non-uniform evaporation of the solvent. A constant value of the porosity can not be achieved even with very tight tolerances. In addition, uncertainties occur in at least one other production step. Scenario two assumes uncertain parameters due to the coating and drying processes. The applied mass loading varies, as an uncertain coating thickness is applied on the substrate in the coating process, also the slurry density is an uncertain structural input parameter resulting for example from deviations in the previous mixing and dispersing process. Scenario three considers deviations caused by the drying and calendering process. Here, the minimal porosity $\epsilon_{c,\min}$, the maximal density $\rho_{c,\max}$, the resistance factor γ_c and the line load q_L are assumed to be uncertain. The line load is the varying process parameter for this production step. The other parameters vary due to uncertainties in the material. Finally, scenario four assumes that uncertainties arise from all three production processes. Mean values and standard deviations for the input process and structural parameters for each production step are displayed in Table 4.3.

For each scenario the production process of 500 cells were simulated in the process chain model. The varying input parameters for each cell were estimated with a Monte-Carlo based approach. For each input parameter a Gaussian distribution was assumed. For this study only cell-to-cell deviations are considered, i.e., each parameter is assumed to be constant within a single cell, but parameters vary between cells. Deviations over the thickness and the area of the electrode are not considered. In the work of Laue et al. [15] these aspects were considered and analyzed. The assumed uncertainties in the production process lead to uncertainties in the structural parameters entering the battery model. These are: the thickness, porosity and tortuosity of the cathode. The volumetric energy density is chosen as the main performance property for evaluating the effect of

Table 4.3: Uncertain input parameters for the models in the process chain model for scenarios S1-S4. Mean values are given in scenario four, and deviations in scenario two to four.

Parameter Unit	Coating		Drying		Calendering		
	M_{wet} mg cm^{-2}	ρ_{slurry} g cm^{-3}	ϵ_{dry} -	ϵ_{min} -	$\rho_{\text{c,max}}$ g cm^{-3}	γ_{c} N mm^{-1}	q_{L} N mm^{-1}
S1	39.3	2.72	0.470	0.232	3.38	592	642
S2	± 0.4	± 0.03	± 0.009	-	-	-	-
S3	-	-	± 0.009	± 0.002	± 0.03	± 12	± 44
S4	± 0.4	± 0.03	± 0.009	± 0.002	± 0.03	± 12	± 44

uncertainties in the production on the cell performance, because it contains the effect of a varying discharge capacity and the voltage losses, and thus is capable of evaluating the performance. The energy density depends on the modulus of operation. All simulations are conducted at four different discharge rates: 0.1 C, 0.3 C, 0.5 C and 1 C. Understanding the impact of uncertainties for different C-Rates will also allow to identify and thus to tailor the production process for maximum allowable deviations for a given battery application.

4.5 Discussion of the simulation results

The results part is divided in two parts. In the first section the correlation between the production processes and the electrode structure generated from the process chain model is discussed. In the second part, the influence of the uncertain structural parameters on the electrochemical properties of the cells is evaluated, and the findings are connected to the insights of the first part. This leads to a continuous analysis of the interactions and uncertainties from the process to the structure to the electrochemical properties.

4.5.1 Production impact on structural parameters

In this part the impact of uncertainties in the production processes on the electrode structure will be analyzed. The uncertainties were estimated based on the process models presented in section 4.2.1 and the input parameters listed in Table 4.3. In Table 4.4, the resulting mean values, standard deviations and relative standard deviations for cathode thickness, porosity and tortuosity are listed for each scenario after the calendering process. Based on the data in the table, it can be seen that the mean value of the structural parameters remain relatively constant for all production scenarios. The layer thickness of the cathode shows high deviations for scenario two and four. The standard deviation of the porosity and tortuosity of the cathode is high for scenario three and

four.

Table 4.4: Mean value, standard deviation and relative standard deviation of the resulting structural parameters after calendering for the cathode thickness, porosity and tortuosity with the implemented process models. These structural parameters are used as input parameters for the battery cell simulation.

Parameter Unit	Layer thickness d_{el} μm	Porosity ϵ_e -	Tortuosity τ -
S1	65.09	0.3124	1.896
S2	$65.05 \pm 1.95 (\pm 3\%)$	$0.3122 \pm 0.003 (\pm 1.1\%)$	$1.897 \pm 0.011 (\pm 0.6\%)$
S3	$65.12 \pm 0.76 (\pm 1.2\%)$	$0.3124 \pm 0.007 (\pm 2.3\%)$	$1.897 \pm 0.024 (\pm 1.3\%)$
S4	$65.12 \pm 2.16 (\pm 3.3\%)$	$0.3131 \pm 0.007 (\pm 2.3\%)$	$1.894 \pm 0.024 (\pm 1.3\%)$

In the following paragraphs the determined uncertainties for the layer thickness, porosity and tortuosity are discussed in relation to the production scenarios and compared to literature values. In Figure 4.2a, the distributions of the cathode thickness for the different production scenarios are displayed. The width of the distribution is greatest for scenario two and four and narrowest for scenario three. The second scenario deals with the influence of uncertainties in the coating and drying process, while the fourth scenario is a combination of the second and third scenario (see Table 4.3). The results show that the cathode layer thickness is mainly affected by uncertainties in the coating process. Due to eq. 4.1, the deviation of the layer thickness is based on the uncertain mass loading applied on the substrate. According to the scenarios, the mass loading varies for scenario two and four, but stays constant for scenario three (Figure 4.2b). The distribution of the cathode layer thickness estimated for scenario four can be compared to the results of scenario two. This is supported by the values of the standard deviation and relative standard deviation in Table 4.4. It can be concluded that the cathode layer thickness and the mass loading are sensitive to uncertainties in the coating process. Furthermore, the calendering process is effective at setting a certain electrode thickness even if the calendering process itself is not that accurate, but it cannot maintain or adjust a constant height if a varying mass loading is applied, due to uncertainties in the coating process.

In Figure 4.3a, the distributions of the cathode porosity for the simulated scenarios are displayed. In contrast to Figure 4.2a and b, the width of the distribution is greatest for scenario three and four and narrow for scenario two. In the third scenario, uncertainties arise in the drying and calendering process, while the fourth scenario is a combination of the second and third scenario. Taking the figure and the values for the standard deviation and the relative standard deviation into consideration it can be concluded that the cathode porosity is sensitive against uncertainties in the calendering process. Furthermore, it can be observed that for a constant calendering process (scenario 2) the relative standard deviation of the porosity is lowered from approximately 2% after the drying process (see Table 4.3) to 1.1% after the calendering process. The constant

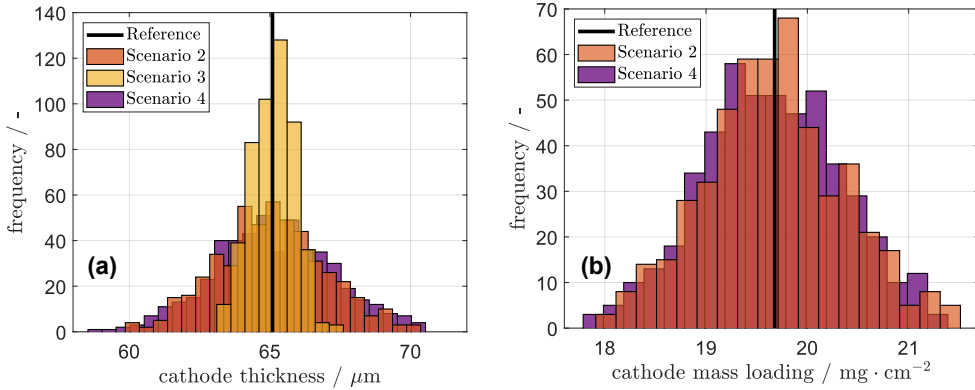


Figure 4.2: Histogram of the cathode thickness (a) and mass loading (b) for the different scenarios.

calendering step led to a homogenization of the porosity within the cathode. This is caused by the process control of the calendering process. Applying a constant line load leads to an evenly adjusted porosity of the electrode after calendering, as thicker electrode sections are compressed with the same force. The effect of the line load on the porosity is discussed in depth by Meyer et al. [97]. This is also the reason why a constant line load in the calendering process does not lead to a homogenization of the layer thickness. The use of a gap-controlled machine would lead to an interaction between the layer thickness and the porosity, since thicker sections of the electrode are also more strongly calendered.

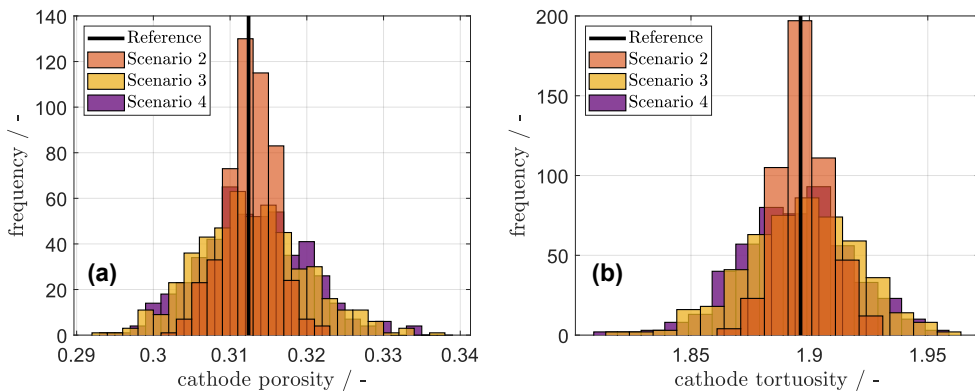


Figure 4.3: Histogram of the cathode porosity (a) and tortuosity (b) for the different scenarios.

The distribution of the cathode tortuosity is displayed in Figure 4.3b. The resulting distributions are comparable to the results of the cathode porosity due to the calculation of the tortuosity based on equation 4.12 with a constant Bruggemann coefficient.

In a study from Hoffmann et al. [59], the deviation of structural parameters for pilot production processes were analyzed. For a double-sided coating process the deviations of the layer thickness for the cathode was approximately $\pm 0.89 \mu\text{m}$. This is slightly above the estimated values for the process chain model. In the study a double-sided coating process was analyzed and the complexity of the applied models in the process chain model are limited. However, the structural parameters generated with the model are comparable to the results of the work. For the porosity of the cathode, Hoffmann evaluated a deviation of $\pm 1.73 \%$ and this can be compared to the results of the process chain model. The tortuosity of the electrodes were not evaluated in the work of Hoffmann.

In summary, it can be stated that the production steps considered in this study have a varying impact on the structural parameters and the effect could be estimated with the model approach. Within the framework of the process models used in this study, the following assumptions arise:

- **Scenario 1:** Reference - no uncertainties in all production steps
- **Scenario 2:** Load dominated - high uncertainties for the mass loading and the cathode thickness due to the uncertainties in the coating process
- **Scenario 3:** Porosity dominated - high uncertainties for the porosity due to uncertainties in the calendering process
- **Scenario 4:** Combination - high uncertainties for the thickness, porosity and tortuosity due to uncertainties in all production steps

Furthermore, it can be concluded that for the applied models in this study no relevant interactions and superposition between the thickness and the porosity occur, due to the process control of the calendering step. Changing the process models and the process control will result in a different outcome.

4.5.2 Battery performance

In this part, the propagation of the uncertainties in structural parameters and the impact on the electrochemical performance properties is analyzed. In combination with the results from the previous section, conclusions can be made on how uncertainties in the production process affect the performance of the simulated battery. The estimated varying structural parameters (see Table 4.4) are taken as an input for the battery model described in section 2.3.2. Also included are the measured, identified and chosen parameters listed in Table 4.2.

Firstly, the distribution of the volumetric energy density is studied in depth as an indicator for the electrochemical performance properties. Simulations were conducted at 0.1 C, 0.3 C, 0.5 C

and 1 C. The results for 0.5 C are not discussed in detail, as they follow the trend of the other discharge rates. In Figure 4.4, the distributions for the different production scenarios are plotted for all considered discharge rates. The mean value, standard deviation and relative standard deviation extracted from these data are listed in Table 4.5. Based on these results it can be stated that the mean value of the volumetric energy density remains approximately constant for a certain discharge rate for all scenarios. Additionally the results show, that an increasing discharge rate leads to a decreasing energy density. The load dominated and the combined scenario (Scenario 2 and 4) show always the widest distribution. The shape of the resulting distribution for the energy density is skewed for low discharge rates and the shape and the width shifts to a Gaussian distribution with increasing discharge rate.

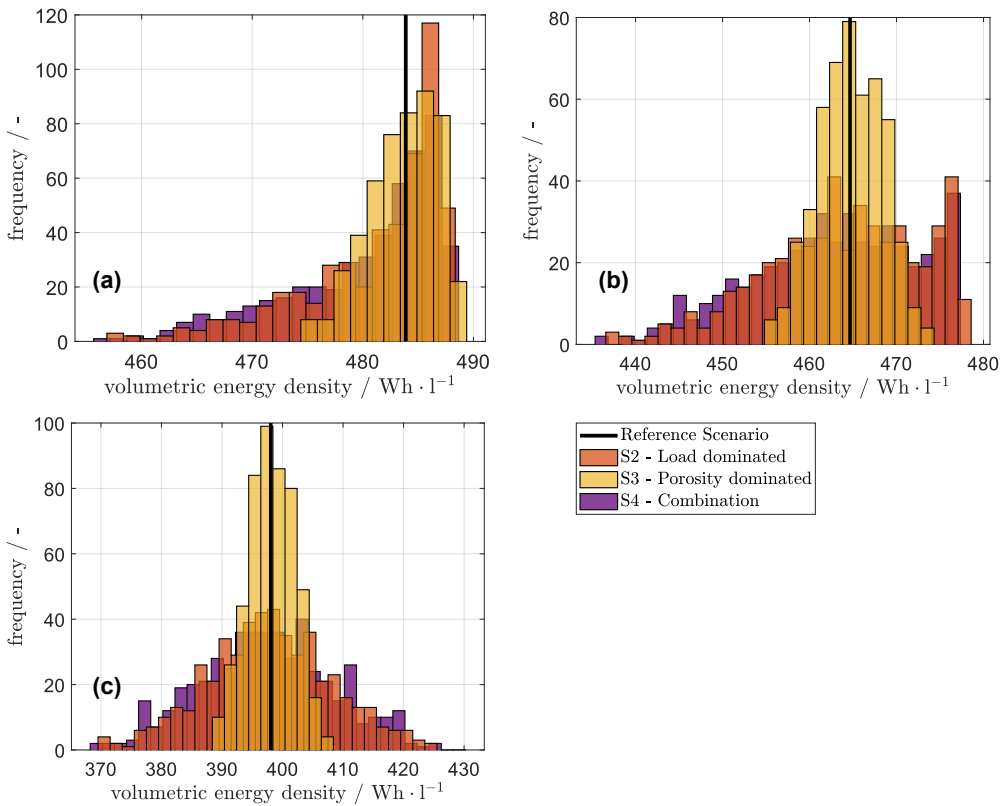


Figure 4.4: Histogram of the volumetric energy density estimated with the battery model. Included are the different scenarios and three different discharge rates 0.1 C (a), 0.3 C (b), 1 C (c).

Table 4.5: Mean value, standard deviation and relative standard deviation for the estimated energy density for each discharge rate.

Property Unit	Energy Density at 0.1 C Wh l^{-1}	Energy Density at 0.3 C Wh l^{-1}	Energy Density at 1 C Wh l^{-1}
S1	483.88	464.66	398.06
S2	$480.97 \pm 6.43 (\pm 1.34 \%)$	$463.81 \pm 9.05 (\pm 1.95 \%)$	$397.91 \pm 10.48 (\pm 2.63 \%)$
S3	$483.64 \pm 3.08 (\pm 0.64 \%)$	$464.78 \pm 3.72 (\pm 0.80 \%)$	$398.21 \pm 3.75 (\pm 0.94 \%)$
S4	$480.38 \pm 6.84 (\pm 1.42 \%)$	$463.34 \pm 9.57 (\pm 2.07 \%)$	$397.54 \pm 11.07 (\pm 2.78 \%)$

Table 4.6: Mean value, standard deviation and relative standard deviation for the estimated discharge capacity for each discharge rate.

Property Unit	Capacity at 0.1 C Ah m^{-2}	Capacity at 0.3 C Ah m^{-2}	Capacity at 1 C Ah m^{-2}
S1	30.09	29.11	25.66
S2	$29.88 \pm 0.65 (\pm 2.2 \%)$	$29.06 \pm 0.84 (\pm 2.9 \%)$	$25.65 \pm 0.91 (\pm 3.6 \%)$
S3	$30.07 \pm 0.24 (\pm 0.8 \%)$	$29.11 \pm 0.28 (\pm 0.97 \%)$	$25.67 \pm 0.28 (\pm 1.1 \%)$
S4	$29.85 \pm 0.69 (\pm 2.3 \%)$	$29.04 \pm 0.89 (\pm 3.1 \%)$	$25.63 \pm 0.96 (\pm 3.8 \%)$

In order to gain a deeper understanding of how uncertainties of structural parameters affect the electrochemical performance properties, three essential aspects of the electrochemical simulations will be analyzed in the following. Firstly, limiting processes of the reference scenario are analyzed. This is used to explain the sensitivity of the uncertainties on the electrochemical performance properties. In the second part, the effect of uncertainties in varying production steps on the volumetric energy density is studied in depth and sensitive parameters and processes are identified. The last part deals with how the different shapes of distributions arise and how they can be interpreted and evaluated.

4.5.2.1 Analysis of the physical limitations of the reference battery

The decrease of the energy density with increasing discharge rates results from slow solid diffusion in the cathode AM particles. The analysis of the results for the reference case shows that for all discharge rates the lithium concentration in the AM particles of the cathode is not uniform (Figure 4.5). Whereas it is uniform for the anode with a maximum lithium concentration difference of 0.5 % at high discharge rates between the inner particle and the area close to the surface. The depletion in the cathode particles happens due to the relatively slow solid diffusion compared to the fast reaction kinetics at the surface of the particle for higher discharge rates. Further

the lithium-ion transport in the electrolyte is not limiting the performance of the battery for the considered discharge rates up to 1 C as the lithium ion concentration in the electrolyte does not drop under 1000 mol m^{-3} . In Figure 4.5, the lithium concentration in the cathodic solid particles at a discharge rate of 0.1 C is close to the maximum lithium concentration of 44949 mol m^{-3} (see Table 4.2) at the surface, thus the utilization of the AM at the cathode is relatively high. The lithium concentration of the anode in the solid particles is relatively low with around 800 mol m^{-3} at 0.1 C. This indicates, that the battery is well balanced at a discharge rate of 0.1 C. Increasing the cathode layer thickness leads to a limitation of the discharge capacity due to an undersized anode, while decreasing the cathode thickness leads to a limiting cathode. This aspect is discussed in depth in section 4.5.2.3.

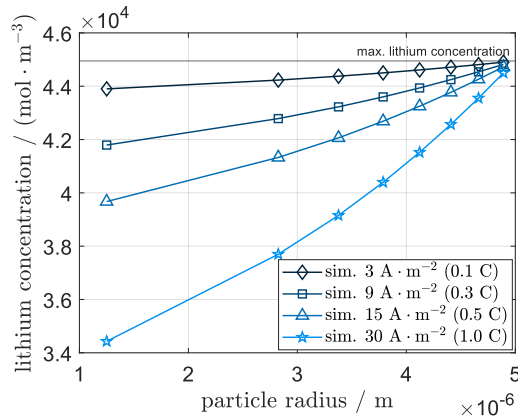


Figure 4.5: Lithium concentration in the solid particles of the cathode averaged over the electrode thickness for the reference scenario at the end of discharge.

4.5.2.2 Impact of the uncertainties in varying production processes on the volumetric energy density

Uncertainties in the the mass loading based on tolerances in the coating process have a significant effect on the distribution of volumetric energy density. From nominal behavior the simulation results show that for all discharge rates the deviation of the energy density is greatest for scenario two (load dominated) and four (combination). Uncertainties in the mass loading lead to similar relative standard deviations for the discharge capacities of the individual cells as for the volumetric energy density (Table 4.6). This behavior is also described by An et al. [12], who showed that the deviation of the discharge capacity is correlated to the deviation of the cell

weight. The third production scenario (porosity dominated) is characterized by uncertain porosity and tortuosity. These deviations mainly affect the kinetics of the electrode. The effective transport coefficients are varying due to both uncertain structural parameters. The effective ionic conductivity and the effective diffusion coefficient in the electrolyte vary around $\pm 2.19\%$, and the effective solid conductivity varies around $\pm 0.64\%$. Additionally the active surface area is changing due to the uncertainties in the porosity of the cathode. The active surface area varies at around $\pm 0.64\%$. Overall the deviations of the effective transport coefficient have a minor effect on the electrochemical performance, due to the non-existent limitation in the transport processes in the electrolyte discussed previously.

In Figure 4.6, the energy densities for every simulated cell for all scenarios are plotted for different discharge rates. Additionally, a surface plot illustrates the dependence of the volumetric energy density on changing thickness and porosity of the cathode. The surface is generated by deterministic simulation using an equidistant deviation of cathode thickness and porosity. Note that although tortuosity deviation is not taken into account the results of the scenarios are located on the surface. This shows the low impact of tortuosity for this surface generation, on the volumetric energy density (max. deviation approx. 0.005 %).

Based on the figure it can also be concluded that the production scenarios lead to differently arranged distributions on the surface. If the deviation induced by the process is oriented in the direction of a steep slope, the process has a significant impact on the volumetric energy density. The load dominated scenario (S2) and the combined scenario (S4) are defined by their wide distribution of the cathode thickness, thus they are oriented towards a steep gradient of the surface. The porosity dominated scenario (S3) is oriented in the direction of a flat gradient of the surface. Hence, S2 has more impact on the battery performance than S3. The combined model approach thus is able to identify the coating process as the most sensitive one. The results indicate to first tackle the tolerances in the coating process, due to the high sensitivity on the volumetric energy density.

4.5.2.3 Shape and width of the distributions for varying discharge rates

The analysis of the distributions for the volumetric energy density shows that for low discharge rates of 0.1 C and 0.3 C, skewed distributions and not Gaussian distributions are obtained for the volumetric energy density (see Figure 4.4). At higher discharge rates of 1 C, the shape of the distribution shifts in the direction of a Gaussian distribution. To evaluate quantitatively whether the estimated distributions are normally distributed, a one-sample Kolmogorov-Smirnov test was conducted. The test statistic is the maximum absolute difference between an empirical cumulative distribution function describing the data and a hypothesized cumulative distribution function. The hypothesis is either accepted or rejected. The one-sample Kolmogorov-Smirnov test leads to the conclusion that the distributions are not Gaussian distributed with a 5 % significance level

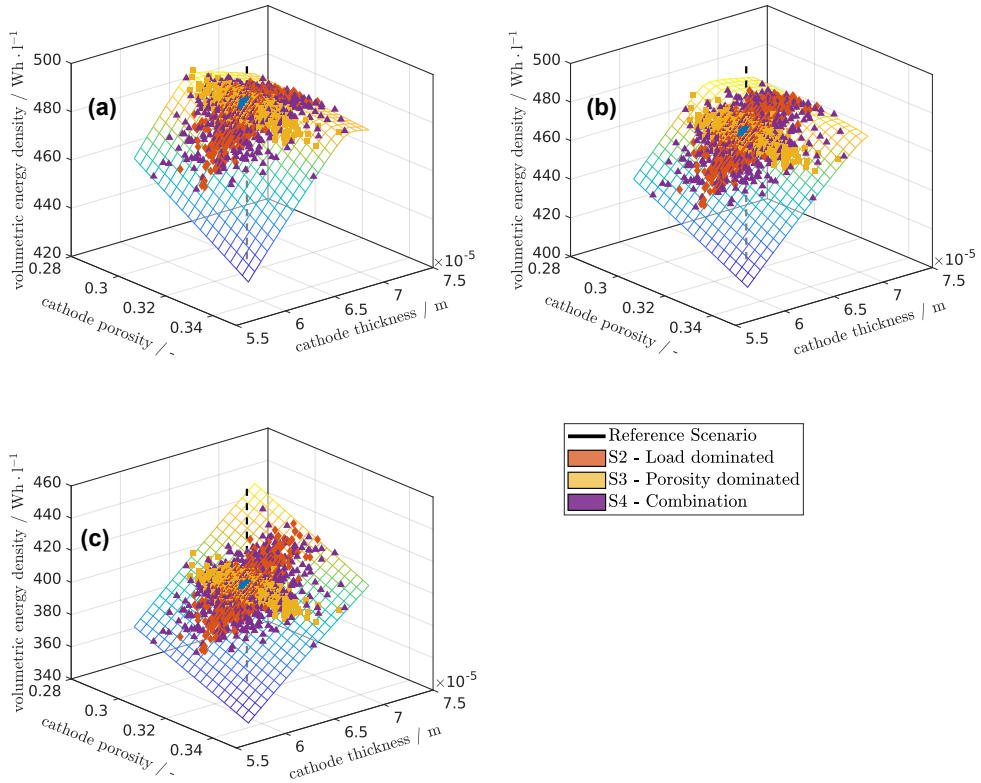


Figure 4.6: Simulated energy densities for three different discharge rates 0.1 C (a), 0.3 C (b), 1 C (c). Grid: model results for equidistant deviation in porosity and thickness, symbols are results of the reference case (\bullet) and scenarios (\triangle). The colours are consistent to the previous plots. Blue: Scenario 1, Red: Scenario 2, Yellow: Scenario 3, Purple: Scenario 4.

for all discharge rates.

The shape and the width of the distribution is mainly affected by the behavior of the volumetric energy density in the considered uncertainty range of the structural parameters. In Figure 4.6, the surface plot visualizes the behavior of the volumetric energy density as a function of layer thickness and porosity for a low discharge rate. Characteristic for the surface plot is the ridge defining an optimal volumetric energy density depending on the cathode layer thickness and the cathode porosity. This is decisively influenced by the utilization of the electrodes as discussed in the part of the physical limitations of the reference battery in section 4.5.2.1. Additionally, it is observed that the slope in front of the ridge, i.e., for low cathode thicknesses, is steeper than behind it. Two different processes can be related to this behavior. For low cathode layer thicknesses the volumetric energy density is increasing with thickness, because the mass loading in the cathode is increased and thus the storage capacity for lithium in the AM is enhanced. Hence,

the cathode is limiting the performance. Behind the ridge, i.e., for thick cathodes, the volumetric energy density is decreasing, because increasing the cathode mass loading leads to a not fully utilized capacity of the cathode, and unused AM is added and the anode is the limiting electrode. Thus the volumetric energy density decreases.

Increasing the mass loading is also achieved by reducing the porosity of the cathode. This leads to an orientation of the ridge non-orthogonal to the varying layer thickness. Furthermore, the surface is slightly tilted. This happens due to the consideration of the volumetric energy density. At lower cathode layer thickness and porosity, the discharge capacity and the overpotentials are almost identical, but the volume of the battery is smaller due to the reduced layer thickness. The impact of the lower porosity could be seen by looking at the gravimetric energy density. In summary, it can be seen that there is a non-linear dependence of the volumetric energy density on the layer thickness and the porosity.

The location and orientation of the uncertainties on the previously described surface is crucial for whether a skewed distribution occurs. This aspect will be illustrated at an simplified example shown in Figure 4.7.

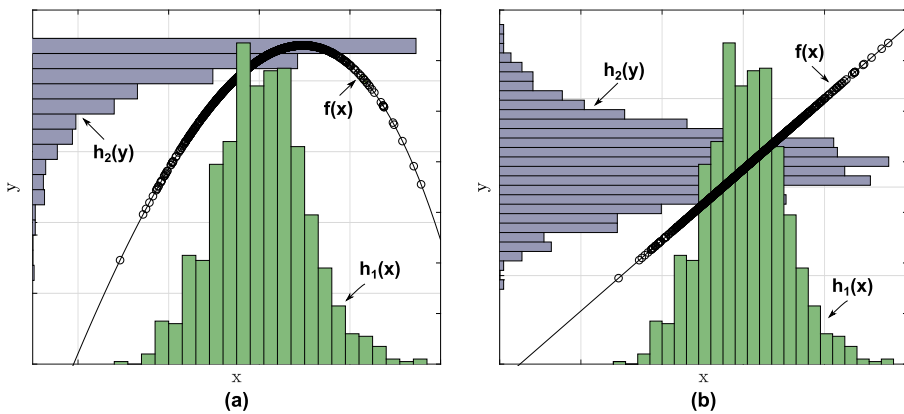


Figure 4.7: Illustration of the impact of an uncertain input parameter x with Gaussian distribution on the output y . This is shown for an arbitrary function with an optimum (a) and an arbitrary linear function (b).

The distribution function $h_1(x)$ represents a deviation of the input x , e.g. the thickness, and is chosen as a Gaussian distribution. The distribution function $h_1(x)$ is transferred to the distribution function $h_2(y)$, which represents the distribution of the output, e.g. the energy density. Distributions are transferred using simple function $f(x)$, e.g. describing the battery performance. We show two examples for the function $f(x)$. A second order polynomial function with a maximum within the distribution of $h_1(x)$ is shown in Figure 4.7a. It can be seen that functions with non linearity yields skewing of the function $h_2(y)$ and the functions maximum yields an upper bound for the output distribution $h_2(y)$. In contrast a linear function only yields transfer of the

variables proportional to the slope, but preserves the distribution shape. With this in mind the results in Figure 4.4 and 4.6 will be discussed in more detail.

In Figure 4.6a, the volumetric energy density for 0.1 C is plotted. It is observed, that the volumetric energy density of the reference battery is located on the ridge of the meshed surface and the deviations cluster around this reference point. The orientation of the deviations arising in Scenario 2 and 4 is mainly arranged in the direction of the cathode thickness and nearly orthogonal to the ridge. This orientation and location lead to the skewed shape of the distribution, analogous to the behavior described in Figure 4.7a.

Increasing the discharge rate up to 0.3 C, the reference battery and the deviations are located further away from the ridge of the meshed area (see Figure 4.6 b). This happens due to the effect of the kinetic limitations in the solid diffusion in the cathode particles illustrated and discussed in section 4.5.2.1 and in Figure 4.5. The optimum shifts in the direction of thicker cathodes, because the increased volume leads to a decrease of the reaction current j^{Li} , and the thicker cathode has the ability to store more lithium despite the limitation of solid diffusion and thus leads to a higher utilization of lithium in the anode. The impact of the optimum is still visible in the histogram of 0.3 C in Figure 4.6b which reveals that a bimodal shape of the distribution exists for this discharge rate.

Increasing the discharge rate up to 1 C, the impact of the kinetics on the volumetric energy density increases and the simulated cells move further away from the ridge and are located in an area of an approximately constant slope (see Figure 4.6c). A Gaussian distribution in an area of a constant slope will lead to a Gaussian distribution. This behavior is analogous to the linear function illustrated in Figure 4.7b. This effect is observed in Figure 4.4: with increasing the discharge rate, the shape of the distributions is close to a Gaussian distribution.

Additionally, it can be observed that the width of the distribution is increasing while increasing the discharge rate. In Table 4.5, it can be seen, that the standard deviation for the volumetric energy density is increasing more rapidly for scenario two and four. This effect also results from the less skewed shape of the distributions at higher discharge rates and the increased slope. While the shape is shifting, the distributions start to spread out, due to the more normalized shape and a steep constant slope.

The values estimated for the capacity displayed in Table 4.6 can be compared to the results generated by Hoffmann et al. [59]. The overall capacity for Hoffmann is at around 39.60 Ah m^{-2} . This is slightly higher than for the cells studied in this study. The standard deviation for Hoffmann is given at around 1.14 Ah m^{-2} . This is also above the values estimated in this study, but overall the range of the deviation can be compared between these two studies. Taking into account the simplifications done in this study, e.g. not considering the whole production chain and the reduced precision of the battery model in terms of the microstructure, a reasonable prediction of the electrochemical performance and the varying performance is achieved.

4.6 Concluding remarks

The chapter contributes to understanding the propagation of uncertainties arising in the production process and quantifying their impact on electrochemical performance. Therefore, the digitalization platform introduced in Chapter 3 was implemented and applied. Studying the propagation of uncertainties was done by analyzing four different uncertainty scenarios. The sets of randomly distributed input parameters were generated with the Monte Carlo method.

The process chain model in the digitalization platform was applied with analytical models for the coating, drying, and calendaring steps. The structural parameters estimated there are forwarded to the p2D electrochemical battery model. It describes the operation of the digital battery and can evaluate the electrochemical performance. The model is parameterized based on measurements conducted for a reference cell. A case study was conducted with the digitalization platform by analyzing four scenarios with varying origins of the uncertainties in the three analyzed production processes. Evaluating these four cases revealed that the model approach can identify the coating process as highly sensitive related to the volumetric energy density. Hence, tight tolerances are required for the layer thickness and mass loading due to their high impact on performance. Analyzing the propagation of uncertainties within the process chain demonstrates that a consistent calendaring process with low tolerances can decrease deviations in the porosity induced by coating and drying. Hence, the calendaring process can homogenize the porosity of the electrode structure. Furthermore, it was observed that uncertainties in the range of a performance optimum lead to skewed distributions. Analyzing the data of production cells and observing skewed distributions could indicate that batteries are produced close to the performance optimum.

It was shown that the digitalization platform can evaluate the effects of uncertainties and describe their propagation. That is accomplished by pointing out relevant parameter correlations. Weaknesses, such as the coating process, can thus be identified. However, generating the sample points with a Monte Carlo method is not suitable for in-depth analysis, and the computational effort is high. Furthermore, the evaluation is based on qualitative descriptions and observations and lacks in the quantitative determination of sensitivities.

In the next chapter, the approach is further extended to investigate the effects of uncertainties in more detail and to enable robust design optimization. Therefore, mathematical methods for uncertainty quantification, metamodeling, and sensitivity analysis are applied to overcome the trial-and-error approach and provide a knowledge-based analysis.

5 Robust Design of Lithium-Ion Battery Cathodes⁴

5.1 Introduction

The digitalization platform was introduced in Chapter 3 and applied in Chapter 4. It was shown that the approach could quantify the impact of uncertainties in the production process. The coating process, and thus the mass loading was identified to have the highest impact on the electrochemical performance. However, uncertainties were used for evaluating only a specific electrode design.

In this chapter, the focus is shifted to the battery cell model and the analysis module of the platform. The scope is to establish a method that enables knowledge-driven optimization under consideration of uncertainties. The process chain model is excluded, but the studied input parameters for the electrochemical model are closely related to the output of the process models. Model-based optimization of the electrode structure for improving the electrochemical performance has already been carried out extensively in the literature. Establishing the p2D model by Doyle, Fuller, and Newman in the early 1990s enabled distinct predictability of the performance by correlating the physical processes with structural features of the electrodes [65, 66]. Thus, optimizing the structure in terms of thickness and porosity was conducted after establishing the model [34, 110, 111]. Constantly increasing the requirements for lithium-ion batteries results in extended and more complex models. These can improve predictability and thus enable enhanced optimization possibilities [26, 27]. Furthermore, new structural features like multi-layer and graded electrodes are in focus for improved performance and need to be studied. Witt et al. analyzed these electrode structures and distinguished between the charge and discharge processes due to their different requirements. That is especially of interest when optimizing the electrode structure for fast charging applications [38]. Thus, knowledge-driven optimization of the electrode microstructure is one main aspect when applying electrochemical models.

⁴ Part of this chapter has been published in Schmidt, Krewer, in preparation [109]

The so far presented literature neglects the impact of structure-related uncertainties in optimization. Therefore, identified design points might not be favorable in terms of robustness. Uncertainties in the identified optimal design parameters might result in significant deviations from the predicted optimal performance. Indeed, Laue et al. [15] stated that robust optimization taking process-related uncertainties into account would be beneficial. Witt et al. [38] discussed that considering uncertainties in the optimization is of high interest for the production process to improve sustainability and production-related performance variances. Thus, implementing robust optimization in the framework of the digitalization platform is of high interest for knowledge-driven optimization to tackle especially the aspects of improve sustainability and performance variances induced by process uncertainties.

The goal of robust optimization is to identify the best performance while reducing the deviation of the model output for an uncertain input. That is achieved by changing the impact of the input parameters [112]. It is mandatory to recognize that the deviation of the input is not changed, as it is assumed to be inherent to the production process. Instead, the mean value is shifted to change the parametric sensitivity. Implementing robust optimization was already successfully applied in various fields, for example, in chemical engineering [113, 114]. In the production of pharmaceutical products, the method was applied to increase the robustness of processes against uncertainties. Optimizing the process under consideration of parametric uncertainties ensures distinct product quality and robustness, for example, against deviations of process temperature [75, 77]. In the field of battery design, the consideration of uncertainties and a robust design has not yet been explored in depth. Yoo et al. [115] introduced a study on reliability-based design optimization for lithium-ion batteries. The impact of uncertainties in thickness, porosity, and particle size on the specific energy and power were analyzed. Establishing the robust design approach resulted in a reduced probability of failure. However, the limitations of different designs and operations were not discussed in-depth, and the selected parameters are not coupled directly to the production processes.

In this chapter, optimizing the cathode structure is done while considering uncertainties. The goal is to identify an optimal design in terms of performance that holds even under uncertain production conditions. The cathode structure is optimized for different operating conditions while reducing the deviation of performance and the scrap rate in production. Therefore, an electrochemical half-cell model is implemented, focusing on the cathode. First, the dependence of electrochemical performance on mass loading and coating density is analyzed. The focus is on identifying limitations in performance due to slow kinetics and transport. In the second part, the mass loading and coating density are adjusted to generate cathodes with a maximized volumetric energy density while providing the desired capacity at a given current density. This is the reference case of optimization, which does not take uncertainties into account yet. Subsequently, uncertainties in the mass loading and coating density are induced on the identified optimal cathode structures, and the impact on the electrochemical performance is studied. In the last part, robust optimization is conducted by considering uncertainties to identify optimal mass loading

and coating density. Hence, the electrochemical performance is robust against uncertainties in the cathode design. Additionally, in the objective function, a penalty term is added for reducing the scrap rate. An efficient optimization algorithm is implemented using metamodels for time-efficient uncertainty quantification.

5.2 Experimental cell setup

The electrochemical model used in this chapter represents a half cell which was measured electrochemically. The cell consisted of an NMC622 cathode as the working electrode and a lithium foil as the counter reference electrode. The half cell was assembled in a coin cell setup. The NMC622 cathode was manufactured and provided by the FPL from the ZSW in Ulm, and the coin cell was assembled and electrochemically measured by Lea Kremer from the ZSW in Ulm. The electrodes were circular with a diameter of 1.2 cm. The separator consisted of two layers of GF/A (Whatman glass fiber) and the electrolyte was a 1.0 M LiPF_6 in EC:EMC (3:7 in weight) with additional 2 wt% VC. Detailed structural and material information concerning the cathode and separator is provided in Appendix A.2. For this experimental cell, the formation was done with three consecutive, galvanostatic constant current cycles at $C/10$ in an operational voltage range between 3 and 4.3 V. The rate capability measurement was performed after the formation, including current densities between 1 and 12 mA/cm^2 in the operational voltage range between 3 and 4.3 V. The lithiation curves of the rate capability measurements are displayed in Figure A.2, in the appendix.

5.3 Electrochemical model

The electrochemical model is based on the p2D model as introduced in Chapter 2.3.2. The discretization in the electrolyte is only done in x-direction. Here, the model is adapted and extended to be applicable for modeling the impact of production on performance with increased accuracy.

The first adaption takes into account that only a half cell battery is evaluated in this chapter, as described in Section 5.2. The cell consists of an NMC622 cathode, a separator, and a lithium foil anode and is used for parameterization and validation of the model. The setup with the ideal, yet not technically relevant lithium metal anode is chosen to solely focus on the cathode to reduce the complexity of the system. This neglects effects such as the impact of electrode balancing, gradients and losses in the anode, and SEI formation. The model uses a coupled PDE system in the cathode and separator. The state variables for the liquid electrolyte (c_e and ϕ_e) are solved in both domains. In the cathodic domain, the variables for the solid (c_s , and ϕ_s) are estimated. The

lithium foil anode is implemented as an infinite lithium source providing the necessary lithium ions for the reaction in the cathode. Therefore, the boundary condition of the species transport in the liquid phase is replaced. The new boundary condition is implemented at the separator on the opposite side of the cathode, i.e., the separator side facing the counter electrode being the lithium foil anode. In detail, eq. 2.17 from Table 2.1 is replaced by

$$\frac{\partial c_e}{\partial x}(0) = \frac{-I_{\text{cell}}}{A_{\text{cell}} \cdot F} (1 - t_p), \quad \frac{\partial c_e}{\partial x}(L_{\text{cell}}) = 0. \quad (5.1)$$

The boundary condition enables the infinite lithium ion supply because the amount of ions entering the separator at the anode interface is equal to the number of lithium ions reacting at the surface of the cathode particles. The open-cell potential of the lithium foil anode is zero, and independent of the state-of-charge [65]. The charge transport in the solid of the lithium anode is neglected, and thus the solid potential of the anode is zero and eq. 2.12 simplifies to

$$U_{\text{cell}} = \phi_s(L_{\text{cell}}). \quad (5.2)$$

Summing up, the cell voltage only depends on the solid phase potential at the current collector of the cathode. The other equations are similar to the full cell model.

The second adaption focuses on the transport processes and the reaction kinetics of the battery. In this chapter, the structure of the porous electrode is changed due to the varying mass loading and coating density of the cathode. Hence, layer thickness, porosity, and tortuosity are affected. In Chapter 2.1.2, an overview is provided on how the micro and macro kinetics of the electrode is affected by the porous microstructure. Therefore, it is of interest to map the impact of structural changes on the effective parameters describing the kinetic processes in the p2D model. Commonly, the Bruggeman relations introduced in Chapter 2.3.2 (eq. 2.23, 2.24, 2.22, 2.21) are implemented. However, these model equations are known to be not accurate enough for predicting the effects of production processes on the electrochemical performance [26, 27, 33].

The correlations between porous microstructure and volume-averaged effective kinetic properties must be represented with increased accuracy. In literature, several solutions are provided for increasing the predictability of the p2D model by calculating the effective transport parameters based on artificial electrode structures [26, 27]. For this work, the approach by Laue et al. [27, 33] is implemented into the p2D model. In the following the main equations are briefly summarized.

In the beginning, effective volume fractions are introduced which are used for the empiric surrogate equations:

$$\epsilon_{\text{AM}}^* = \frac{\epsilon_{\text{AM}} - \epsilon_{\text{crit,s}}}{1 - \epsilon_{\text{crit,s}}}, \quad \forall \epsilon_{\text{AM}} : \epsilon_{\text{AM}} > \epsilon_{\text{crit,s}}, \quad (5.3)$$

$$\epsilon^* = \frac{\epsilon - \epsilon_{\text{crit,e}}}{1 - \epsilon_{\text{crit,e}}}, \quad \forall \epsilon : \epsilon > \epsilon_{\text{crit,e}}, \quad (5.4)$$

$$\epsilon_{\text{CBM}}^* = \epsilon_{\text{CBM}} \frac{\epsilon_{\text{CBM}} + \epsilon_{\text{AM}} - \epsilon_{\text{crit,s}}}{1 - \epsilon_{\text{crit,s}}}, \quad \forall \epsilon_{\text{CBM}} : \epsilon_{\text{CBM}} + \epsilon_{\text{AM}} > \epsilon_{\text{crit,s}} \quad (5.5)$$

The effective volume fractions for the AM ϵ_{AM}^* and the electrolyte ϵ^* take a critical percolation threshold volume fraction $\epsilon_{\text{crit,e}}$ for the electrolyte and $\epsilon_{\text{crit,s}}$ for the solid into account (see eq. 5.3, 5.4). Hence, the surrogate equations implemented in the following allow combining the Bruggeman relations with the existence of a percolation threshold of a conducting network affecting the effective parameters. The critical percolation threshold for the solid phase $\epsilon_{\text{crit,s}}$ is related to the combined volume of the carbon black-binder matrix (CBM) and the active material (AM). For the effective volume fraction of the CBM in eq. 5.5, the strong interaction of the AM and the CBM is taken into account. Thereby the effective volume fraction of the CBM considers that in a dense AM structure the CBM percolates at lower volume fractions compared to a less dense AM structure.

The ionic conductivity calculated with the Bruggeman relation does not take the impact of the CBM into account. The surrogate equation is extended by this effect and thus the new model equation for the effective ionic conductivity is

$$\kappa_{\text{e,eff}} = \kappa_{\text{e}} \cdot (\epsilon^*)^{\beta_1 + \beta_2}. \quad (5.6)$$

That equation is strongly related to Bruggeman, but for representing the effect of the CBM on the tortuosity an empiric term β_2 is added, which is:

$$\beta_2 = \epsilon_{\text{CBM}}^{v_1}. \quad (5.7)$$

It represents the increase of liquid phase tortuosity due to the CBM in the microstructure. The fitting parameters for this equation are $\epsilon_{\text{crit,e}}$, β_1 , and v_1 . The exponent β_1 considers the tortuosity due to the active material like the classical Bruggeman coefficient. However, it deviates due to fitting from the classical value.

The equation for the solid phase conductivity in the empiric surrogate model takes the impact of a percolating CBM network into account. That results in a low solid phase conductivity before a percolating network of CBM is established in the electrode. Increasing the volume fractions results in a steep increase in solid phase conductivity as most of the electrical current is transported via the CBM and its higher electrical conductivity.

$$\begin{aligned} \kappa_{\text{s,eff}} = & \kappa_{\text{CBM}} \cdot (\epsilon_{\text{CBM}}^*)^{\beta_3} \cdot \frac{1}{2} \left(1 + \tanh \left(\frac{1}{v_2} \epsilon_{\text{CBM}}^* - v_3 \right) \right) \\ & + \left(\frac{1}{\kappa_{\text{CBM}} \cdot (\epsilon_{\text{CBM}}^*)^{\beta_3} + 2\kappa_{\text{AM}} \cdot (\epsilon_{\text{AM}}^*)^{\beta_4}} + \frac{1}{2\kappa_{\text{AM}} \cdot (\epsilon_{\text{AM}}^*)^{\beta_4}} \right)^{-1}. \end{aligned} \quad (5.8)$$

The fitting parameters are $\varepsilon_{\text{crit},s}$, β_3 , β_4 , v_2 , and v_3 . In the absence of CBM the equation simplifies to the classical Bruggeman relation.

The effective active surface area relevant for the kinetics of the charge-transfer reaction is introduced by:

$$a_S = \left(1 - v_4 \frac{\varepsilon_{\text{CBM}}^{v_5}}{\varepsilon_{\text{AM}}} \right) v_6 \frac{1 - 4(0.75 - \varepsilon_{\text{AM}})^2 \cdot \varepsilon_e}{R_p}. \quad (5.9)$$

The fitting parameters for this equation are: v_4 , v_5 , and v_6 . The equation takes the blocking of the active surface by the CBM into account and the particle-to-particle contact.

The introduced equations replace the ones stated in Chapter 2.3.2 for the p2D model and result in a more accurate description of the correlation between microstructure and kinetics. The fitting parameters for eqs. 5.3 to 5.9 are taken from Ref. [27]. Those are based on artificial 3D NMC microstructures generated and analyzed in detail in the reference.

The simulations conducted in this chapter are done with the described extended p2D model. The required model parameters can be taken from Tables A.2 and A.3, in the appendix. The parameters were estimated based on the electrochemical measurements conducted with the experimental coin cell (see Chapter 5.2) and parameters taken from the literature. The upper and lower values for the voltage range in all simulations were set to the experimental values of 3-4.3 V.

5.4 Impact of mass loading and coating density

In this part, the impact of mass loading and coating density on the electrochemical performance of the NMC cathode is studied. The coating density describes the proportion of solid material within the electrode volume and thus provides information about the compaction of the electrode. It is mainly adjusted in the calendaring process and influences the coating thickness, porosity, and tortuosity. In particular, the interaction between mass loading and coating density is of interest since both have an impact on the kinetic and transport processes.

First, the mass loading is changed. The coating density is kept constant, which suggests similar line loadings in the calendaring. Thus, the internal microstructure of the electrode, including porosity and effective parameters, is comparable. Subsequently, the coating density for the cathode with the highest mass loading is changed, and its impact on the electrochemical performance is studied. The performance of the cathodes is rated by the areal capacity and volumetric energy density.

Evaluating the impact of mass loading and coating density requires calculating structural input parameters for the battery model, i.e., porosity and thickness of the electrode. Additionally, the specific areal capacity of the electrode based on the specific capacity of the NMC622 is estimated. Calculating these quantities is based on simple geometric and mass fraction calculations

and considers the composition of the electrode and material properties. An overview and short explanation of the equations are provided in the appendix (see eq. B.1-B.7). The electrode composition and materials are based on the experimental cathode and are given in Table B.1, in the appendix.

Table 5.1: Specifications of seven cathodes with varying mass loadings and the coating densities. The data for the experimental electrode are highlighted by the star.

fixed parameters		estimated parameters		
mass loading mg cm^{-2}	coating density g cm^{-3}	thickness μm	porosity -	specific capacity (C/10) mA h cm^{-2}
5	3.0	16.7	0.32	0.8
14.5*	3.0*	48.3*	0.32*	2.4*
25	3.0	83.3	0.32	4.2
35	3.0	116.6	0.32	5.9
45	3.0	150.0	0.32	7.5
45	2.7	166.7	0.39	7.5
45	3.3	136.4	0.25	7.5

* experimental cathode

To see the impact of the mass loading, five cathodes are analyzed with loadings between 5 and 45 mg cm^{-2} and constant coating density of 3.0 g cm^{-3} . In addition, to see the impact of the coating density, besides a coating density of 3.0 g cm^{-3} , two additional coating densities of 2.7 and 3.3 g cm^{-3} were evaluated, where the mass loading was kept constant at 45 mg cm^{-2} . The estimated parameters for all cathodes are provided in Table 5.1. The experimental electrode is highlighted by a star in the table. Kremer et al. [36] analyzed a comparable material system based on an NMC622 cathode within a similar range of mass loadings and coating density in an experimental study. The thicknesses, porosities, and specific areal capacities of the manufactured electrodes match well with the theoretical values estimated here.

In the following simulations, the lithiation of the cathode is analyzed for increasing current densities in the range of 1 to 12 mA/cm^2 . The respective C-rates depend on the mass loading. The cathode with the lowest mass loading will experience up to 15 C, while thick cathodes will barely achieve 2 C. The C-rate can be calculated using the specific areal capacity provided in Table 5.1 and the applied current density.

In Figure 5.1a, the capacities of the seven cathodes are displayed for increasing current densities. In Figure 5.3a, the volumetric energy densities are plotted. Please note that the volumetric energy density is calculated based on the volume of the cathode coating and not the volume of the battery cell.

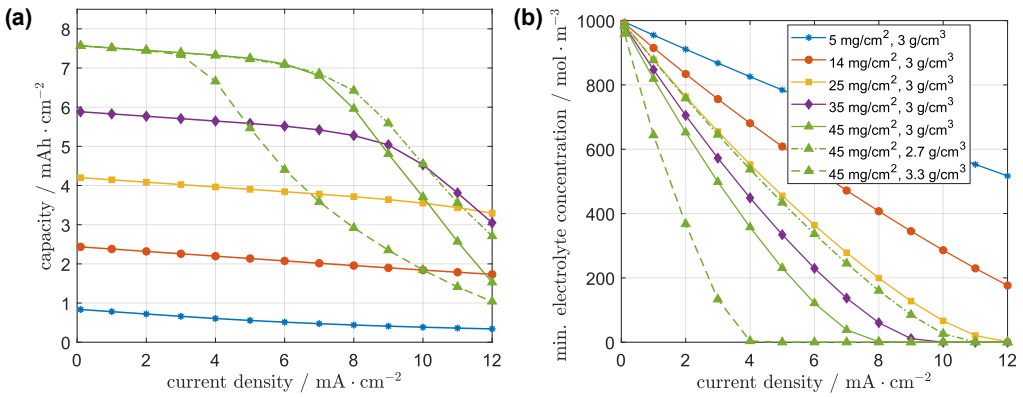


Figure 5.1: (a) areal capacity, and (b) minimal ion concentration ever occurring in the electrolyte during the simulation, for cathodes with varying mass loading (solid lines) and coating density (dashed lines) at increasing current densities. The detailed specifications of the cathodes are listed in Table 5.1

The results for the areal capacity in Figure 5.1a show the rate performance of the cathodes. At first, the focus is on the cathodes with increasing mass loadings (solid lines). At low current densities, all cathodes provide the estimated specific capacity based on material and structural parameters as given in Table 5.1. Increasing the mass loading at low current densities results in an increased capacity, as the absolute amount of active material in the cathode increases and kinetic losses are not relevant. Cathodes with a low mass loading can deliver most of their capacity even for high current densities. The cathodes with mass loadings of 14.5 mg cm^{-2} and 25 mg cm^{-2} can still provide approx. 70% of their initial capacity at a current density of 12 mA cm^{-2} . The cathode with mass loading of 5 mg cm^{-2} can only provide 40% of its initial capacity at this current density, but the absolute capacity loss is in the same order of magnitude as for loadings of 14.5 mg cm^{-2} and 25 mg cm^{-2} . In contrast, cathodes with high mass loadings reveal pronounced performance losses above a specific current density recognized by a steep decrease of the capacity. The cathode with 45 mg cm^{-2} can only provide 20% of its initial capacity at the highest analyzed current density. It is observed that increasing the mass loading shifts the location of the steep capacity decrease to lower current densities. For 35 mg cm^{-2} , it occurs at around 10 mA cm^{-2} , while for 45 mg cm^{-2} the steep decrease starts at a current density of around 8 mA cm^{-2} . The additional performance losses related to the steep decrease in capacity are caused by the relatively slow diffusion of the lithium ions in the liquid electrolyte. In the electrochemical model, the electrolyte concentration is a state variable and solved during the simulation. In Figure 5.1b, the lowest ion concentration ever occurring in the electrolyte close to the current collector is displayed for increasing current densities. Comparing Figure 5.1a and b show that the lithium ion concentration in the electrolyte drops to zero for current densities where the steep decrease in capacity occurs. Increasing the mass loading, and thus the electrode thickness, results in prolonged diffusion lengths, whereas increasing the current density leads to

faster reaction rates at the surface of the particles. Close to the transition to the rapid capacity drop, the fast reaction rate starts to cause the depletion of lithium ions in the electrolyte at the current collector because the diffusion of the ions in the electrolyte is not sufficient to provide enough ions. Further increase of the current density beyond this point shifts the area of depletion in the direction of the separator. In Figure 5.2, the ion concentration in the electrolyte at the end of the discharge is displayed for the cathode with a mass loading of 45 mg cm^{-2} and a coating density of 3.0 g cm^{-3} . It can be observed that increasing the current density results in more pronounced depletion that spread out from the current collector to the separator. Consequently, the discharge capacity decreases. The limitations in performance for thick electrodes due to slow diffusion in the electrolyte were already discussed in literature [32, 116]. The current density causing a depletion of the ion concentration in the electrolyte at the current collector is often described as the diffusion limiting current or maximum working current.

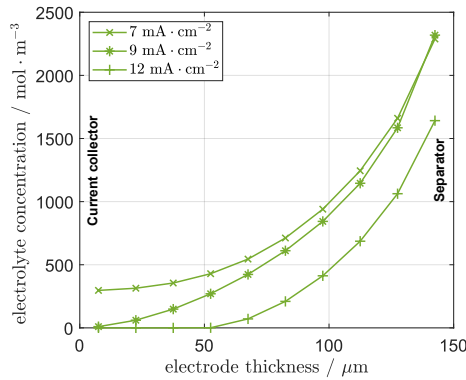


Figure 5.2: Ion concentration in the electrolyte at $U_{\text{Cell}} = 3.0 \text{ V}$ vs. the electrode thickness for three different current densities. The results are displayed for the cathode with a mass loading of 45 mg cm^{-2} and a coating density of 3.0 g cm^{-3} .

In Figure 5.1a, the impact of the coating density on the capacity is shown by the dashed lines. Decreasing the coating density from 3.3 g cm^{-3} to 3.0 g cm^{-3} and then to 2.7 g cm^{-3} results in improved capacities at higher current densities. That is correlated to the increase in porosity from 25 % to 39 % (Table 5.1), which improves the effective diffusion coefficient in the electrolyte. Thus, the depletion of the Li^+ in the electrolyte and the drop in capacity is shifted to higher current densities. The ion concentration in the electrolyte is displayed in Figure 5.1b and it can be observed that decreasing the coating density results in improved ion concentrations during lithiation of the cathode.

In Figure 5.3a, the volumetric energy density is displayed for the seven cathodes for increasing current densities. At first, the effect of varying mass loadings is discussed (solid lines). At low current densities, all cathodes provide the same volumetric energy density. Here, the energy is

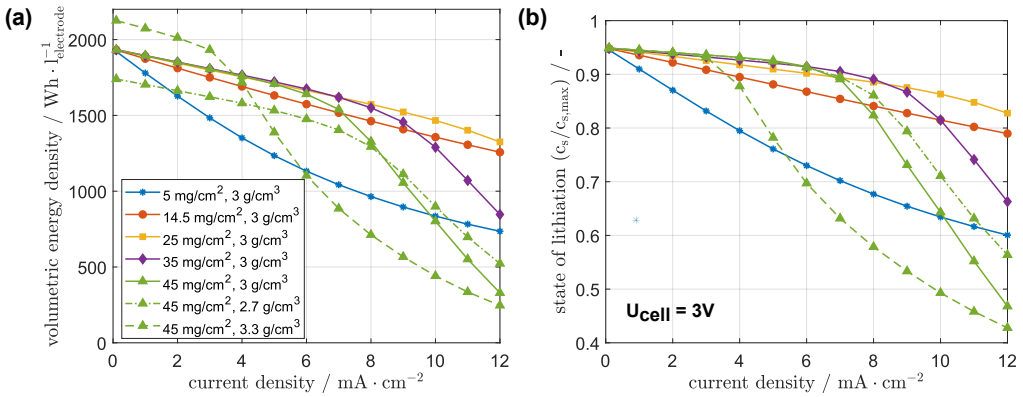


Figure 5.3: (a) volumetric energy density, and (b) the volume averaged state of lithiation in the active material particles at the lower voltage boundary of 3 V for cathodes with varying mass loadings and coating densities.

not affected by the kinetics but solely by the theoretical storage capacity per volume, which is identical for all cells due to the similar coating density and structure. Increasing the current density reveals mainly two transport processes affecting the volumetric energy density. That is the solid diffusion in the active material particles for thin electrodes and the ion diffusion in the liquid electrolyte for thick electrodes as discussed previously. Thin cathodes with a low mass loading of only 5 mg cm^{-2} or 14.5 mg cm^{-2} reveal a decrease in volumetric energy density compared to cathodes with a mass loading above 25 mg cm^{-2} . Due to the low mass loading, high C-rates are already achieved for low current densities. Interactions of the relatively slow solid diffusion in the active material particles and the fast reaction kinetics at the surfaces of the particles worsen the lithiation of the active material particles and thus the utilization of the electrode. This is emphasized by Figure 5.3b. Here, the state of lithiation of the active material particles at the end of the simulation is displayed. Increasing the mass loading results in reduced C-rates and reduced volumetric reaction fluxes at the surface of the particles. The utilization of the active material improves. Cathodes with a mass loading of approx. 25 mg cm^{-2} show overall good lithiation of the active material. Further increasing the mass loading is not beneficial for increasing the volumetric energy density. For high mass loadings and high current densities, additional limitations on the volumetric energy density by diffusion in the electrolyte are visible. The effects are identical to those in Figure 5.1a and thus occur at the same current densities. Again, increasing the mass loading shifts the drop in volumetric energy density in the direction of lower current densities. The impact of the slow diffusion in the liquid electrolyte can also be observed in the lithiation of the active material (see Figure 5.3b). Decreasing the coating density from 3 g cm^{-3} to 2.7 g cm^{-3} results mainly in a decreased volumetric energy density as can be seen in Figure 5.3a. The volume of the electrode increases without providing higher capacities (see Figure 5.1a). However, at very high current densities the improved ion diffusion in the electrolyte results in slightly increased volumetric energy densities as the depletion is hindered. Increasing the coating density

to 3.3 g cm^{-3} results in higher volumetric energy densities at low current densities. The volume is decreased and the cathode can store the same amount of lithium. However, the drop in capacity and energy density occurs already at relatively low current densities.

Kremer et al. [117] analyzed the impact of mass loading and coating density on the volumetric energy density of NMC622 cathodes in an experimental study. It was observed that increasing the mass loading results in a decreasing volumetric energy density at high current densities. Increasing the coating density resulted in an increasing volumetric energy density at lower current densities but a steep decrease in volumetric energy density already at moderate current densities. These results match well with the results obtained with the electrochemical model. Additionally, the model is capable of visualizing the depletion of the lithium ion concentration and thus can give additional insights into the limiting processes.

In summary, mass loading and coating density both affect the ion transport in the electrolyte. As a result, there is a steep decrease in performance at higher current densities, observed in the capacity and the volumetric energy density. However, the capacity is mainly affected by the mass loading. The coating density only influences capacity when there are limitations in the transport of the electrolyte. The coating density, in turn, has a higher impact on the volumetric energy density at lower current densities. At high current densities, the volumetric energy density and the capacity are influenced by both parameters, since they affect the transport in the electrolyte. The interactions between the mass loading and the coating density are of interest to achieve good performance.

5.5 Deterministic optimization of the cathode design

In the previous section, the electrochemical model was used to analyze the impact of mass loading and coating density on the electrochemical performance. It was shown, that varying the mass loading and coating density affects the diffusion of the lithium ions in the electrolyte resulting in relevant performance limitations. Thus, both parameters have to be considered when generating high-energy cathodes. In this section, the mass loading and coating density is adjusted to identify an optimal cathode design using deterministic optimization. The goal is to maximize the volumetric energy density of the cathode.

5.5.1 Implementation

The deterministic optimization is conducted under the constraint that a certain capacity is required at a set current density. Two cathode designs should be identified providing a discharge capacity of 6 mA h cm^{-2} , but at two current densities of 3 mA cm^{-2} for case (I-6-3) and 8 mA cm^{-2} for case (II-6-8). Thus, a high capacity is achieved, but at two different operational points at a low and high current density.

The constrained optimization problem is defined as:

$$\begin{aligned}
 & \underset{M_{\text{solid}}, \rho_C}{\text{maximize}} && Q(M_{\text{solid}}, \rho_C) \\
 & \text{subject to} && C - C_{\text{set}} = 0 \\
 & && 5 \text{ mg cm}^{-2} < M_{\text{solid}} < 50 \text{ mg cm}^{-2} \\
 & && 2.5 \text{ g cm}^{-3} < \rho_C < 3.5 \text{ g cm}^{-3}
 \end{aligned} \tag{5.10}$$

with the volumetric energy density $Q(M_{\text{solid}}, \rho_C)$ as objective function to be maximized. The volumetric energy density depends on the mass loading M_{solid} and coating density ρ_C as adjustable variables. The optimization is conducted under the equality constraint that the cathodes should achieve a capacity C_{set} of 6 mA h cm^{-2} . The mass loading is bound between limits of 10 mg cm^{-2} and 50 mg cm^{-2} . The coating density is bound between 2.5 g cm^{-3} and 3.5 g cm^{-3} . The optimization is conducted twice for the two different current densities.

The optimization is carried out in Mathworks MATLAB vR2018b, and the *fmincon* algorithm, which is a gradient-based method is combined with the *GlobalSearch* algorithm to find a global optimum by repeatedly running the local solver.

5.5.2 Simulation results

The starting point of the deterministic optimization is provided by setting the coating density of an initial cathode to 3.0 g cm^{-3} . The mass loading is calculated following eq. B.8 and the specific capacity of the NMC622. Thus, at a low current density, a specific areal capacity of 6 mA h cm^{-2} is achieved by considering the material properties. Consequently, the initial value is already close to the deterministic optimum. However, the capacity at higher current densities will differ from this theoretical value. The initial values for mass loading and coating density are provided in Table 5.2. The initial cathode design was analyzed with the electrochemical battery model at the current densities of 3 mA cm^{-2} for case (I-6-3) and 8 mA cm^{-2} for case (II-6-8). The estimated capacities and volumetric energy densities are provided in Table 5.2.

Table 5.2: Mass loadings and coating densities, and the respective performance characteristics for the initial cathode design and the values obtained by the deterministic optimization for the two different cases (I-6-3) at low current densities and (II-6-8) at high current densities.

		Case (I-6-3)		Case (II-6-8)	
		Initial	Deterministic	Initial	Deterministic
mass loading	mg cm^{-2}	35.7	36.9	35.7	40.1
coating density	g cm^{-3}	3.0	3.34	3.0	2.95
current density	mA cm^{-2}	3.0	3.0	8.0	8.0
capacity	mAh cm^{-2}	5.8	6.0	5.4	6.0
vol. energy density	WhL^{-1}	1808.9	1966.5	1544.7	1490.4

The results of the deterministic optimization are provided in Table 5.2. For the cathode design at case (I-6-3), the volumetric energy density is increased by approx. 9 % up to 1966.5 WhL^{-1} . The equality constraint of the optimization is fulfilled by achieving a capacity of 6 mAh cm^{-2} . The mass loading is slightly increased by 3 % for reaching the desired capacity. The coating density is increased by 12 % for improving the volumetric energy density. The identified optimal cathode design at case (II-6-8) also fulfills the constraint regarding the capacity. The volumetric energy density decreases by 4 % down to 1490.5 WhL^{-1} compared to the performance of the initial design. It is not possible to achieve a comparable volumetric energy density to the initial design while providing 6 mAh cm^{-2} at 8 mA cm^{-2} by solely changing the mass loading and coating density. The mass loading is increased for achieving the desired capacity by 12 %. The coating density is only slightly affected by the deterministic optimization.

The changes for both designs fit well with the observations described in Section 5.4, as the mass loading is increased for achieving the desired capacity and the coating density is increased for improving the volumetric energy density. However, the limitations in ion diffusion in the electrolyte must be considered to prevent a steep decrease in capacity and volumetric energy density.

The results obtained by the deterministic optimization for the two cases are analyzed by studying the rate capability, similar to Section 5.4. The two identified optimal cathode designs are compared to the initial design. In Figure 5.4a and b, the results for capacity and volumetric energy density are displayed for current densities in the range of 1 to 12 mA/cm^2 by the solid lines for the deterministic optimization. For case (I-6-3) the increase in discharge capacity and volumetric energy density is visible compared to the initial design. Increasing the volumetric energy density is mainly achieved by increasing the coating density. Consequently, the drop in capacity and volumetric energy density due to lithium ion depletion in the electrolyte is close to the applied current of 3 mA cm^{-2} . For case (II-6-8) the discharge capacity is achieved by mainly increasing the mass loading. That results in thick electrodes and the operational point is at high current

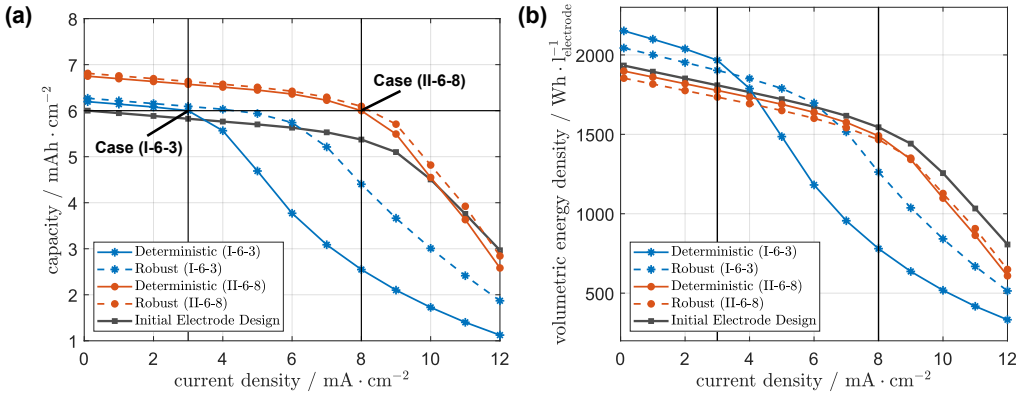


Figure 5.4: (a) capacity, and (b) volumetric energy density for increasing current densities for the initial electrode, and the designs estimated by the deterministic optimization and robust optimization for case (I-6-3) and (II-6-8).

densities where transport of lithium ions in the electrolyte is already a limiting factor. Consequently, it is not possible to maximize the volumetric energy density at that point compared to the initial design as long as the constraint of the desired discharge capacity is mandatory for the optimization. Decreasing the coating density does not result in an increasing volumetric energy density, as it does not significantly improve the transport in the electrolyte and simultaneously decreases the volumetric energy density by increasing the thickness of the cathode. This effect has been discussed in Section 5.4 for the 2.7 g cm^{-3} and 3.0 g cm^{-3} cells. A possible solution for improving the volumetric energy density of these highly loaded cathodes is increasing the lithium salt concentration in the electrolyte, as discussed by Kremer et al. [118].

Overall, the estimated results indicate that the objective function can determine electrode designs that provide the desired capacity at defined current densities. Maximizing the volumetric energy density is achieved but the results strongly depend on the operational point of the cathode. A cathode may be optimized for one operating point but may then not be competitive over a typical full range of operations. For example, cells optimized at high current density may be outperformed by others at lower current density and vice versa. In this regard, it will also be important to understand, how sensitive the results and the optima are to uncertainties, which will be analyzed in the following.

5.6 Influence of uncertainties on optimal cathode design

In the next step, it is assumed that the cathode designs identified by the deterministic optimization are produced, but the coating density and mass loading are affected by uncertainties from the production process. The following analysis reveal how this will affect the electrochemical performance. The aim is to study the impact of uncertainties in mass loading and coating density on capacity and volumetric energy density of highly optimized cathodes.

5.6.1 Implementation

The uncertainty quantification (UQ) is done via metamodels generated by polynomial chaos expansion (PCE) to reduce the computational burden. Mathematical details regarding the PCE are provided in Chapter 2.4.1. In the following, relevant information for the implementation of the PCE is briefly provided. All UQ methods are implemented with UQLab, an open-source MATLAB-based software framework [81].

The non-intrusive generation of the PCE model requires a design of experiment to estimate the polynomial coefficients. The input parameters are the mass loading and coating density. The evaluated outputs are the capacity and volumetric energy density. The random vectors for both input parameters are assumed to be Gaussian distributed. The average values are the parameters at the respective design points and the standard deviation is assumed to be 2 % of the average values. The standard deviation is set based on values provided by Hoffmann et al. [59], as they analyzed the deviation of mass loading and coating density for pilot production processes and estimated a standard deviation in the range of 1.5-2.5 %. The metamodel is generated with the PCE based on a sample size of 1000, and the degree is adapted during the generation. The sample size is selected to achieve an error estimated by the UQLab framework below 0.001 to ensure sufficient accuracy of the metamodel. The coefficients of the PCE are estimated with a least-angle regression. The first order and total order Sobol' indices are estimated in the UQ analysis.

5.6.2 Simulation results

In the following discussion, we assume that a minimum capacity may not be 2 % below the set point. All cells below this value are considered as scrap, i.e., the cells are identified as waste in the end-of-line test. Consequently, all batteries providing a capacity lower than $5.88 \text{ mA h cm}^{-2}$ are defined as scrap. An upper-quality boundary is not implemented in this study. It is assumed

that well-performing electrodes could be used for different applications [119]. The scrap rate is the relative amount of cells providing a capacity lower than the lower quality boundary.

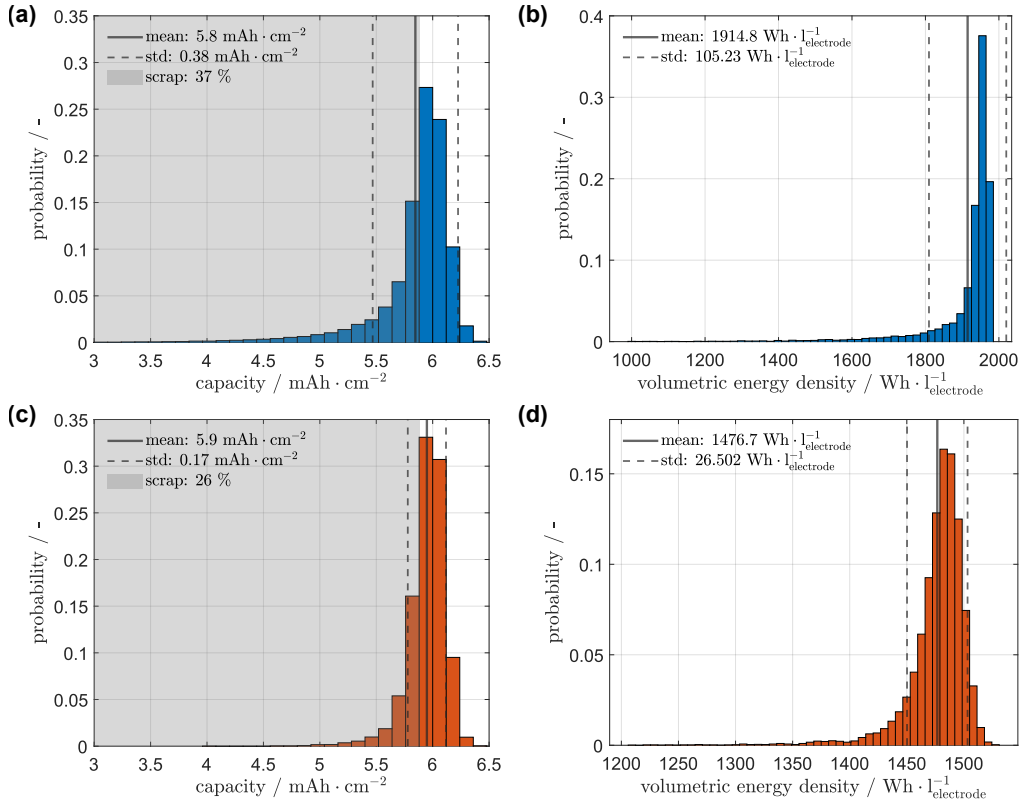


Figure 5.5: Distributions of the performance characteristics after applying uncertainties to the design points estimated in the deterministic design optimization. (a) distribution of the capacity at case (I-6-3), (b) distribution of the volumetric energy density at case (I-6-3), (c) distribution of capacity at case (II-6-8), and (d) distribution of volumetric energy density at case (II-6-8). The grey area in (a) and (c) indicate the region defined as scrap.

In Figures 5.5a and c, the capacity distributions for the designs estimated at optimization cases (I-6-3) and (II-6-8) are displayed. The metamodel was solved for 10000 data points with varying mass loadings and coating densities. The average values and standard deviations are provided in Table 5.3. For both cases, the distributions are skewed to lower values. That results from the non-linear dependence of the capacity on mass loading and coating density. It can be observed, that applying uncertain input parameters results in a reduced average capacity for both cases. The average value is indicated by the solid line and the standard deviation by the dashed lines in the figures. For case (I-6-3) an average capacity of 5.8 mAh cm⁻² is estimated and for case (II-6-8) 5.9 mAh cm⁻². The distribution is thinner for case (II-6-8) with a standard deviation of

$0.17 \text{ mA h cm}^{-2}$, compared to case (I-6-3) with $0.38 \text{ mA h cm}^{-2}$. The grey region highlights the area defined as scrap below a capacity of $5.88 \text{ mA h cm}^{-2}$. Due to the reduced deviation for case (II-6-8), the scrap rate is 26 % and is lower compared to case (I-6-3) with 37 %. In Figure 5.5b and d, the distributions of the volumetric energy density are displayed for cases (I-6-3) and (II-6-8). Similarly as for the capacity, the two distributions show a skewed shape, and the mean values shift to lower values. This results from the optimization of the volumetric energy density in the deterministic optimization. The standard deviation of the volumetric energy density is lower for case (II-6-8) compared to case (I-6-3), as it was already observed for the capacity.

Analyzing the distributions of the capacity and volumetric energy density revealed that case (II-8-6) results in lower standard deviations and scrap rates. Due to the increased current density, this was not expected. Explaining this effect is done by analyzing the total Sobol' indices representing the parametric sensitivities.

Generating the metamodel by the PCE enables estimating the Sobol' indices of the input parameters for no cost. In Figure 5.6a, the total Sobol indices for mass loading and coating density are displayed related to the capacity for the initial design and the designs estimated by the deterministic optimization. The parametric sensitivities shift due to the optimization. For the initial cathode in case (I-6-3), the mass loading was highly sensitive, and after the deterministic optimization, the coating density is more sensitive. That is supported by the results presented in Figure 5.4. The design estimated by the deterministic optimization reveals a steep capacity drop close to the operational point for the case (I-6-3). The coating density is increased for maximizing the volumetric energy density. Consequently, the capacity is not limited by mass loading, but by coating density and thus by slow transport in the electrolyte. The sensitivities of the cathode design in case (II-6-8) also shift, but the difference is not as prominent. In Section 5.4, it was stated that for high current densities, the performance limitations can not solely be related to mass loading or coating density, but the interaction between these two parameters is of interest. This statement is supported by analyzing the parametric sensitivities for case (II-6-8). Optimizing the cathode design for 8 mA cm^{-2} still results in increased sensitivity for the coating density, but the mass loading still has a significant effect on capacity. The impact of the coating density in case (II-6-8) is lower in comparison to the optimized design in case (I-6-3). Hence, uncertainties of the coating density have a lower impact on the discharge capacity, and thus the standard deviation for case (II-6-8) is lower in comparison to (I-6-3). In Figure 5.6b, the total Sobol indices are displayed related to the volumetric energy density. It can be concluded that the coating density has the highest impact on the volumetric energy density for all cases. That is in good agreement with the results obtained in Section 5.4. It was discussed that the mass loading only has a minor impact on the volumetric energy density if the utilization of the active material is sufficient. At higher current densities the mass loading becomes more relevant as the coating thickness increases and the transport in the electrolyte is affected. The coating density has a high impact on the volumetric energy density by changing the volume of the electrode. It can be observed that for case (II-6-8), the mass loading has an increased impact on the volumetric energy

density, as the current density is increased.

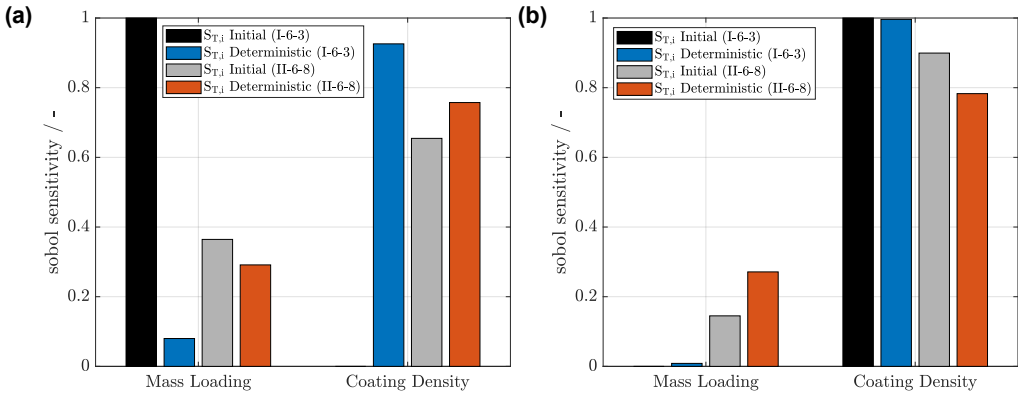


Figure 5.6: Total Sobol' indices for the mass loading and coating density related on: (a) capacity and (b) volumetric energy density for the initial cathode design and the designs estimated in the deterministic optimization.

The results obtained for the parametric sensitivities are in contrast to Chapter 4. It is emphasized that the cathodes used in the two analyses are different. In Chapter 4, a full cell was analyzed. Consequently, the mass loading of the cathode has an impact on the volumetric energy density, especially when considering the balancing with the anode. Furthermore, the cathode has lower thicknesses and mass loadings compared to the cathodes analyzed here. In Section 5.4, it was shown that the mass loading has an impact on the volumetric energy density for thin electrodes by improving the utilization of the active material. The utilization was also an issue described in Chapter 4.5.2.1. For thick electrodes with a high mass loading the utilization of the active material is not an issue, as analyzed in Figure 5.6. The estimated sensitivities and limitations strongly depend on the structure of the electrode, and the operational point. Changing one of these factors might result in different results.

The results generated in this section indicate that considering uncertainties is especially of interest when analyzing the quality and scrap rate of batteries in production. At end-of-line testing, the batteries must fulfill a certain quality gate. In this work, that is represented by a lower quality limit concerning the capacity. Inducing uncertainties on the mass loading and coating densities of optimized electrodes results in rather high scrap rates of 37 % for case (I-6-3) and 26 % for case (II-6-8). The scrap rate in lithium-ion battery production is approx. 10 %. However, the best producers achieve scrap rates of roughly 5 % [57].

In the next chapter, the optimization is repeated, but with consideration of uncertainties. Therefore, the lower quality boundary is already considered during the optimization. The goal is to reduce the scrap rate to improve the sustainability in production already in the design process.

5.7 Robust design optimization of the cathode design

Previously, it was shown that deterministic optimization is capable of estimating designs for cathodes with a maximized volumetric energy density. However, the performance characteristics are not robust against uncertainties resulting in high standard deviations and scrap rates. In the following, the goal is to estimate cathode designs with a maximized volumetric energy density but simultaneously good robustness against uncertainties in performance. Therefore, robust optimization is implemented considering uncertainties.

5.7.1 Implementation

The robust optimization is done using a metamodel generated by the PCE. The uncertainties are estimated based on the metamodel. That enables fast calculation times in the optimization routine. The procedure for the optimization described in the following is based on the work of Xie et al. [120]. The aim is to reduce the number of computationally expensive evaluations of the PCE.

The metamodel is generated with uniformly distributed parameters. The parameter space is defined by a mass loading between 30 mg cm^{-2} and 45 mg cm^{-2} and the coating density is between 2.4 g cm^{-3} and 3.5 g cm^{-3} . The metamodel is sampled in a wider range compared to the boundaries used in the robust optimization. Thus, it is ensured that uncertainties at the upper and lower boundaries of the optimization are not in an undefined parameter region. The sample size for generating the PCE is 1000, and the degree is adapted during the generation. The sample size is selected to achieve an error estimated by the UQLab framework below 0.001 to ensure sufficient accuracy of the metamodel. The coefficients of the PCE are estimated with a least-angle regression. The generated metamodel is used for robust optimization. During each iteration of the optimization, the metamodel is sampled with Gaussian distributed parameters. The average value of the mass loading and coating density is adapted during the optimization, and the standard deviation is assumed to be 2% of the average values. The metamodel provides the average values and standard deviation of the output parameters that can be analyzed in the objective function.

The described procedure allows for a single time-consuming generation of the PCE prior to the optimization. Hence, it is not necessary to generate a metamodel in every iteration. Consequently, fast computing times are achieved.

The objective function used for the robust optimization is closely related to the problem stated for the deterministic optimization, which maximizes the volumetric energy density Q , see eq 5.10. In contrast, the desired capacity is not implemented as a constraint but as a weighted part of the

objective function to allow for more freedom during the optimization. Additionally, the objective function is extended by a term considering the scrap rate S_R . The optimization problem is given by

$$\underset{m_L, \rho_C}{\text{minimize}} \quad a \cdot (\bar{C}(M_{\text{solid}}, \rho_C) - C_{\text{set}})^2 - b \cdot \bar{Q}(M_{\text{solid}}, \rho_C) + c \cdot (S_R(M_{\text{solid}}, \rho_C) - S_{R,\text{set}})^2. \quad (5.11)$$

The first term is minimized by achieving the desired discharge capacity C_{set} on average. The second term maximizes the average value of the volumetric energy density \bar{Q} . The third term is added to minimize the scrap rate. A target for the scrap rate can be defined in the objective function by setting a value for $S_{R,\text{set}}$, and the difference between the estimated and target scrap rate is reduced by the objective function. It was aimed at achieving a scrap rate of approx. 4 % to reach values in the range of the best producers on market. The scrap rate is defined by the lower quality boundary and is defined so that all batteries providing a capacity lower than $5.88 \text{ mA h cm}^{-2}$ are defined as scrap. The single terms of the objective function are weighted by three factors. They are set to $a = 100$, $b = 0.01$, and $c = 5000$. The objective function has to find a trade-off between optimal performance and reduced scrap rate. Changing the weighting factors will result in different results, as the scope of the optimization might shift.

The optimization is carried out in Mathworks MATLAB vR2018b, and the *fmincon* algorithm, which is a gradient-based method is combined with the *GlobalSearch* algorithm to find a global optimum by repeatedly running the local solver. The initial points for the robust design optimization are equal to the initial design of the deterministic design, listed in Table 5.2. The impact of the uncertainties is estimated by sampling 10000 different cathodes with a standard deviation of 2 % for mass loading and coating density.

5.7.2 Simulation results

The results obtained in the robust optimization for cases (I-6-3) and (II-6-8) are provided in Table 5.3. Additionally, the results for the deterministic designs after applying uncertainties are provided for the two cases.

For case (I-6-3) a cathode structure is identified that provides an average capacity of 6.1 mA h cm^{-2} . That is slightly above the desired value of 6 mA h cm^{-2} . The deterministic design provides an average capacity of 5.8 mA h cm^{-2} after considering uncertainties. Consequently, the robust optimization estimates a design with a smaller difference from the desired capacity. The standard deviation of the capacity is $0.13 \text{ mA h cm}^{-2}$ after the robust optimization and is lowered by approx. 35 % compared to the deterministic design. Increasing the capacity and thus increasing the distance between the average value and the lower quality boundary and simultaneously reducing the standard deviation results in a lower scrap rate. Consequently, the scrap rate is reduced from 37 % for the deterministic design down to 4.5 % for the robust design. The desired scrap rate of

Table 5.3: Estimated mean values and standard deviations for the mass loading and coating density and the respective performance characteristics for the deterministic design and the values estimated by the robust design optimization. The values in the brackets indicate the difference to the deterministic optimal value displayed in Table 5.2.

		Case (I-6-3)		Case (II-6-8)	
		Deterministic	Robust	Deterministic	Robust
mean mass loading	mg/cm ²	36.9	37.3	40.2	40.5
std. mass loading	mg/cm ²	0.74	0.75	0.8	0.81
mean coating density	g/cm ³	3.34	3.17	2.98	2.9
std. coating density	g/cm ³	0.07	0.06	0.06	0.058
mean capacity	mAh/cm ²	5.8 (-0.2)	6.1 (+0.1)	5.9 (-0.1)	6.1 (+0.1)
std. capacity	mAh/cm ²	0.38	0.13	0.17	0.11
mean energy density	Wh/L	1914.8 (-51.7)	1901.3 (-65.2)	1476.5 (-13.9)	1460.6 (-29.8)
std. energy density	Wh/L	105.2	31.1	26.74	24.3
scrap rate	%	37	4.5	26	4.4

4 % is not achieved, but the difference is relatively small, and the result is rated sufficient. The capacity distribution for case (I-6-3) after the robust optimization is displayed in Figure 5.7a. The standard deviation is relatively small, and only a minor amount of cathodes are located in the grey region representing the area defined as scrap. The shape of the distribution is close to a normal distribution and not skewed as observed for the deterministic design in Figure 5.5a. The average volumetric energy density after the robust optimization is 1901.3 WhL⁻¹ and is in a similar range as the deterministic design when considering uncertainties. Both values are lower compared to the deterministic optimum of 1966.5 WhL⁻¹, listed in Table 5.2 for case (I-6-3). However, the robust design achieves significantly lower scrap rates while still achieving a competitive volumetric energy density. The standard deviation of the volumetric energy density reduces from 105.2 WhL⁻¹ down to 31.1 WhL⁻¹ due to the implementation of the robust optimization. In Figure 5.7b, the distribution of the volumetric energy density is shown and the average and standard deviation are provided. For case (I-6-3) the performance characteristics are achieved by slightly increasing the mass loading compared to the deterministic design from 36.9 mg cm⁻² up to 37.3 mg cm⁻², thereby the capacity increases. The coating density estimated by the robust optimization is at 3.17 g cm⁻³ and is thus decreased by 0.15 g cm⁻³ compared to the deterministic design. Consequently, the volumetric energy density is not maximized to the upper limit. However, this results in improved transport of the lithium ions in the electrolyte. In Figure 5.4, the rate capability of the average design estimated by the robust optimization is displayed by the dashed lines. It can be observed, that for case (I-6-3), the drop in capacity and volumetric energy density is not close to the design point. Deviations resulting in an increased mass loading or coating density will not result in a steep decrease in capacity and volumetric

energy density, and consequently the standard deviation decreases.

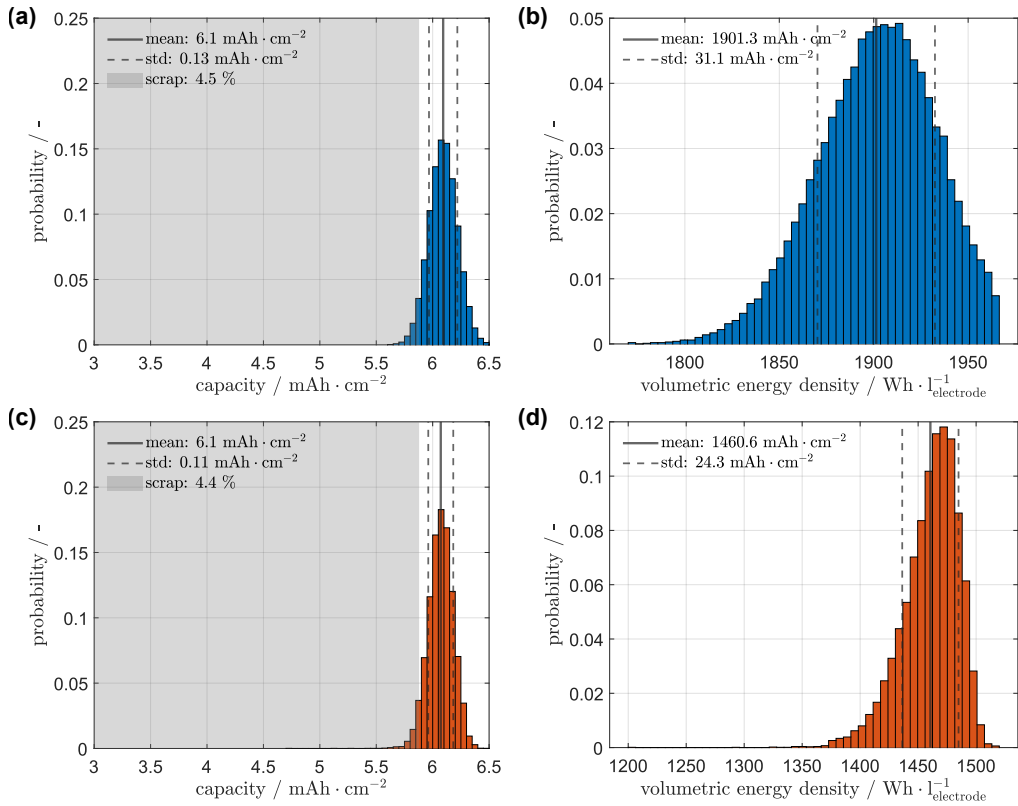


Figure 5.7: Distributions of the performance characteristics after the robust optimization. (a) distribution of the capacity at case (I-6-3), (b) distribution of the volumetric energy density at case (I-6-3), (c) distribution of capacity at case (II-6-8), and (d) distribution of volumetric energy density at case (II-6-8). The grey area in (a) and (c) indicate the region defined as scrap.

The results estimated for case (II-6-8) in the robust optimization are comparable to those for case (I-6-3). The average capacity is increased up to 6.1 mAh cm^{-2} and is thus above the desired capacity. Comparing the deterministic and robust design while considering uncertainties indicates a similar absolute difference between the average capacity and the desired capacity of approx. 0.1 mAh cm^{-2} . The standard deviation of the capacity after the robust optimization is estimated with 0.11 mAh cm^{-2} and is lowered by 35 % compared to the deterministic design. As described previously for case (I-6-3), increasing the average capacity and lowering the standard deviation results in a scrap rate of only 4.3 %. As for case (I-6-3), the scrap rate is rated as sufficient. The capacity distribution is displayed in Figure 5.7c, the mean value shifts to higher values, and the standard deviation is reduced. Consequently, the amount of cells located in the

grey area is reduced, and the shape of the distribution is not skewed compared to Figure 5.5c. The average volumetric energy density is comparable to the results obtained by the deterministic optimization. Compared to the deterministic optimum the volumetric energy density decreases by roughly 30 WhL^{-1} , but still, a relatively high volumetric energy density is achieved. The standard deviation of the volumetric energy density only slightly decreases from 26.7 WhL^{-1} to 24.3 WhL^{-1} . In Figure 5.5d, the volumetric energy density distribution is displayed. The performance characteristics are achieved by slightly increasing the mass loading as already discussed for case (I-6-3) and by lowering the coating density by roughly 0.1 g cm^{-3} . That explains the drop in volumetric energy density as the thickness of the cathode increases without improving the capacity. In Figure 5.4, the rate capability of the average design estimated by the robust optimization is displayed for case (II-6-8). It is shown that for capacity the slope close to the design point is slightly decreased. That is achieved by decreasing the coating density. The volumetric energy density nearly shifts in parallel to lower values due to the increased volume of the electrode without increasing the capacity.

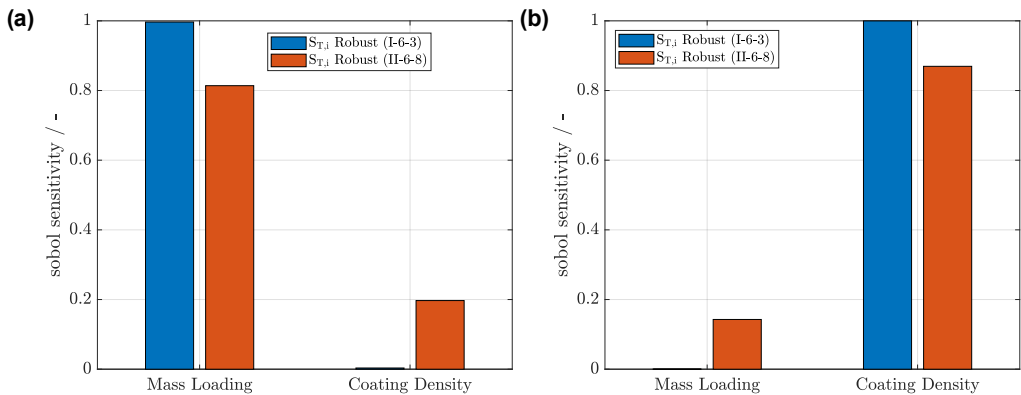


Figure 5.8: Total Sobol' indices for the mass loading and coating density related on: (a) capacity and (b) volumetric energy density for the cathode design estimated in the robust design optimization.

Comparable to the uncertainty quantification for the deterministic design, the parametric sensitivities are studied on the cathode designs estimated by the robust design approach. In Figure 5.8, the parametric sensitivities are displayed related to the capacity and volumetric energy density. They can be compared to the results obtained for the deterministic optimization, plotted in Figure 5.6. In Figure 5.8a, the total Sobol' indices related to the capacity are displayed. It is observed that the mass loading has the highest parametric sensitivity rate on capacity. Contrary, the coating density has a high impact on the volumetric energy density, as displayed in Figure 5.8a. The parametric sensitivities estimated after the robust optimization support the statement that the capacity improves by increasing the mass loading, and the design points are not close to limitations in the transport of ions in the electrolyte. Comparing the cathodes with a coating density

of 3.0 g cm^{-3} , 2.7 g cm^{-3} , and 3.3 g cm^{-3} in Figure 5.1a (dashed lines) indicated that the coating density has no impact on the capacity as long as no limitations occur. That is a central difference from the deterministic optimization, where the coating density had pronounced sensitivity on capacity. The volumetric energy density is mainly affected by the coating density as the volume of the electrode is affected.

The results obtained by the PCE-based metamodel are verified by applying a Monte-Carlo simulation on the electrochemical model. The design points identified in the robust optimization are mapped by 1000 Gaussian distributed input samples. The mean value and standard deviation of capacity and volumetric energy density are estimated directly with the electrochemical model. The difference between the mean values obtained by the electrochemical model and the PCE-based metamodel is below 1 % for capacity and volumetric energy density. The difference in standard deviation is approx. 1 % for capacity and volumetric energy density. The scrap rates estimated directly by the electrochemical model are 4.6 % for case (I-6-3) and 5 % for case (II-6-8). It turns out that slightly higher scrap rates are estimated with the electrochemical model. However, the results obtained in the robust optimization by implementing PCE-based metamodels could be verified by directly sampling the electrochemical model.

The results obtained in the robust design optimization showed that the implemented objective function is able to find a sufficient trade-off between maximizing the volumetric energy density, achieving the desired discharge capacity and reducing the scrap rate. Changing the weighting factor in the objective function could further optimize the results depending on the scope. The high technical relevance of this improved optimization lies especially in the significant reduction of the scrap rate, which was reduced by more than 20 % for this optimization case to economically relevant values below 5 %. As discussed that is achieved by increasing the average capacity and reducing the impact of limitations in transport in the electrolyte to reduce the standard deviation. However, that is only achieved by decreasing the volumetric energy density. The robust optimization helps to reduce the scrap rate while still providing high performance characteristics. Hence, the sustainability in the production increases as the cathode microstructure is designed to be robust against deviations in the production process.

5.8 Concluding remarks

In this chapter, a method was established for identifying a robust optimal cathode design taking structural uncertainties into account. Therefore cathodes with varying mass loadings and coating densities were analyzed in depth. It was shown that both parameters are relevant for improving the electrochemical performance. Their impact depends on the operational point and the electrode structure. Limitations in performance occur due to insufficient transport of the lithium ions

in the electrolyte and slow diffusion in the solid particles. Deterministic optimization of the volumetric energy density of cathodes by changing the mass loading and coating density identified designs are estimated which operational points are close to limitations concerning the transport of the lithium ions in the electrolyte. Applying uncertainties to the identified optimal electrode structures resulted in high standard deviations and scrap rates. Additionally, the average performance characteristics were reduced compared to the deterministic optimum. The standard deviation of the performance is high because of the steep decrease in capacity and volumetric energy density close to the operational point. Applying robust optimization with a flexible objective function allows for reducing the standard deviation and scrap rate drastically. That is mainly achieved by avoiding limitations in the electrolyte transport by estimating cathode designs with a less dense electrode coating. However, reducing the standard deviation and scrap rate is only achieved by slightly reducing the volumetric energy density compared to the deterministic optimum. In general, the objective function shows good results by identifying a trade-off between high volumetric energy density and reduced scrap rate.

In summary, the established methodology of robust optimization demonstrated its power in terms of reducing the standard deviation and scrap rate when considering uncertainties. Future work may target validating the methodology experimentally. Here, also the uncertainties may be specified for the actual production process, similarly to Chapter 4.

The chapter concludes the first part of the dissertation. The influence of uncertainties arising in the production process of lithium-ion batteries were studied in depth. However, the electrode microstructure of a electrode or battery was assumed homogeneous and deviations occurred due to varying properties between cells. In the next part of the dissertation, the average property of electrodes is assumed to be constant but heterogeneous local effects result in uncertainties in performance. That is studied exemplary for varying electrical networks established by the carbon-black binder matrix in the electrode microstructure.

Part 2 - Uncertainties from Electrode Microstructure

6 Uncertainty of Heterogeneous Conductive Networks⁵

6.1 Introduction

In the first part of the thesis a coupled model approach, i.e., the digitalization platform, was introduced and applied for studying the impact of process parameters on electrochemical performance. The focus was on the propagation and optimization of process-induced uncertainties, where uncertainties were defined as cell-to-cell deviations. The electrode microstructure within the battery cell was assumed to be homogeneous. The electrode, however, is a heterogeneous composite microstructure that highly affects kinetic processes related to reaction and transport. Thus, it affects electrochemical properties like performance and aging. The heterogeneous electrode structure leads to local effects. Even with similar average electrode properties the performance characteristics may vary. Thus, the structure needs to be robust for reducing performance uncertainties. In this chapter, the impact of intrinsic structure-related uncertainties is addressed. Using the carbon black-binder matrix (CBM) as an example, the effect of its structure on performance and of structural degradation is studied in depth.

In Chapter 2.1.2, the composite electrode microstructure of LIBs and their impact on physical processes is discussed in detail. The CBM is introduced as an essential part in the structure for transporting electrons and establishing mechanical stability. The conductive additives provide an electrical network in the microstructure that significantly influences the performance of the lithium-ion battery. Dominko et al. [49, 121] showed that the use of small particles of CB can be beneficial for the overall performance of the battery, due to an increased electrical conductivity. Liu et al. [122–124] analyzed the influence of the binder composition and conductive additives and concluded, that a higher binder content leads to an improved CB particle network, resulting in better overall electrical conductivity. They additionally discussed the importance of a percolation threshold for the conductive network and explained that reaching this threshold results in a jump to high conductivity. Mayer et al. [48] investigated the impact of the dispersion process on

⁵ Part of this chapter has been published in Schmidt, Röder, ACS Appl. Energy Mater. 2021, 4, 5, 4845–4860, 2021 [73]

the CB particle size and showed that the structure and the particle size define the electrode properties. They additionally pointed out that a decreased particle size leads to a more cross-linked CBM network. In conclusion, it has been shown that conductive additives and binder need to form a highly linked electrical network that can supply electrons at every spot of the active particle surface [121].

However, the experimental evaluation of the electrical network barely provides mechanistic understanding. Overall, the electrical conductivity of an electrode can be measured by different methods, e.g. with a four-point probe firstly established by Smits in 1958 and since then improved and adapted [125, 126]. However, values being estimated by those method represents only the bulk properties. This allows to estimate if a percolation threshold is exceeded, but a detailed assessment of the network structure is not possible. In a recent study, the method was adapted to study the effect of the local microscopic structure on the electronic impedance. It was shown that strong deviations occur due to structural heterogeneities and it was concluded that these deviations affect the overall performance and degradation [127]. However, the electrical network in terms of the structure and the connectivity was not analyzed in detail, but it is to be expected that the structure of the network has a major effect on the observed phenomena. In contrast to the measurement of the bulk conductivity, a qualitative description of the microstructure and the electrical network is possible using micro- and nanotomography-based electrode reconstruction. Here, focused ion beam - scanning electron microscopy (FIB-SEM) or a coupled approach of Nano-CT, FIB-SEM, and Micro-CT can be used [128, 129]. These methods can give insights into the microstructure and visualize the evolving networks [128]. Additionally, stochastic modeling of electrode microstructure can be used to represent and analyze electrodes in-depth and extract information concerning networks within the structure [130, 131]. However, such a qualitative assessment of electrical network structures does currently not allow a quantitative evaluation of the electrode concerning its electrochemical properties and is also limited for a mechanistic understanding. It can be seen that there is a need for a fundamental theoretical understanding of the impact of the structure of the electrical network on the electrochemical properties of the cell and a more targeted application of the various diagnostic methods.

Mathematical models can be used to gain mechanistic understanding. Electrochemical models of lithium-ion batteries are widely applied. They differ in the level of detail and the computational costs [62]. Models are applied to analyze the influence of different aspects of the microstructure on electrochemical properties, especially in the context of production processes [27, 93, 132]. The works referred to here, take the CBM into account. However, the electrical charge transport is mostly described based on effective transport properties, representing only the bulk. For instance, in the work of Hein et al. [132] the effect of conductive additives and binder on the impedance has been studied. The authors state that the conductive additives and the binder provide a conductive network. However, detailed network structures have not been modeled, but are instead described by the effective coefficient for charge transport. Furthermore, Mistry et al. [26] analyzed network properties of the CBM and examined its influence on the effective electrical

bulk conductivity and ionic conductivity. However, the electrochemical performance was also estimated based on effective transport properties. In fact, only very few approaches in the literature map the transport within the electrode structure by networks. Cocco et al. [133, 134] presented an analytical transport network model, which can rate the effective material transport coefficient based on graph theory and the microstructural network's topology. Besides, they take the channel geometry into account and extended their basic model to be able to show the effect of a reactive flow. Further, Lagadec et al. [135] used a network-based analysis of different separators for lithium-ion batteries to show that microstructural characteristics like porosity and tortuosity are not sufficient to rate the performance. They stated that pore space connectivity is important for high quality separators and that it has an effect on the overall performance. However, to the best of our knowledge, there is no model available that allows to directly assess the impact of electrical networks properties on electrochemical performance.

Hence, in this work, a hybrid model is established that combines a classical battery model based on porous electrode theory [65, 66] with a network-based representation of the electrical network [133]. This enables to investigate the influence of different electrical network structures on the electrochemical performance for the first time. Additionally, the model approach allows studying the impact of the degradation of the CBM. This is one important aging mechanism for cathodes in lithium-ion batteries [40]. To model degradation in lithium-ion batteries, several different approaches are available [136, 137], but a detailed study of how the decomposition of the CBM affects the electrochemical performance does not exist in the literature so far. In this context, a generic simulation study is conducted by generating various artificial electrical networks. These differ in terms of the general structure and the number of nodes and edges. The latter is varied to represent different levels of deagglomeration of the CB agglomerates and thus the resolution of the CBM. The different networks are analyzed concerning the overall cell performance, degradation, and failure, including uncertainties. Here, the degradation of the electrical network is modeled by edge removal, which represents the mechanical degradation of the CB-binder matrix during battery utilization. This enables to determine relevant network properties that lead to a high quality in terms of performance and lifetime of a lithium-ion battery.

6.2 Computational methods

In this chapter, the hybrid model and the applied computational methods are introduced. The hybrid model consists of two sub-models, being a homogeneous electrochemical model and the electrical network model. The combined model, i.e., the hybrid model, is later applied to study the impact of different generic network structures on cell performance, degradation, and failure. The homogeneous electrochemical model implemented in the hybrid model is a p4D model as already described in Chapter 2.3.2 but it is slightly adapted. The model considers a half-cell

with a NMC622 cathode as the working electrode. The separator is neglected. Implementing a half-cell model was already introduced in Chapter 5.3 and is done respectively. For considering the impact of heterogeneity in the porous electrode, periodic boundaries are applied in y- and z-direction to enable mass and charge transport. Please note that the structural surrogate models for the effective kinetic parameters introduced in Chapter 5.3 are not implemented in this chapter. The classical Bruggeman relations are used, as introduced in Chapter 2.3.2.

6.2.1 Hybrid model

In Figure 6.1, the concept for establishing the hybrid model is visualized. The hybrid model includes the complex structure of the electrical network. The starting point for the model development is the electrode structure and the cell design as illustrated on top of the figure. The cell is considered in a half cell setup, while the focus is laid on the cathode. The electrode has a porous structure and consists of three main phases: active material (AM), CBM, and liquid electrolyte (pores). Note that carbon black and binder are defined as one phase as the agglomerates can not clearly be separated, and thus the combined phase is affecting the electron transport, which is a common assumption in the literature [26, 33, 138]. The intercalated lithium can diffuse inside the AM particles. For most cathodes with low electrical conductivity of the AM and sufficient CB content, the electron conduction through the CBM is orders of magnitude higher compared to the AM [27]. In this theoretical study, the contribution of the AM is neglected to focus on the more relevant effect of the CBM. However, in principle a basic conductivity of the AM could be added to the model, as showed by the extended p2D model in Chapter 5. Ionic conductivity and lithium-ion diffusion is ensured by the electrolyte. At points in space where all three phases are present, i.e., at triple-phase boundaries, electrochemical reactions can occur. Instead of modeling all phases and related processes with one modeling approach, two different approaches are applied. The properties of the complex CBM are covered by an electrical network model, while all the other processes are modeled using frequently applied homogeneous porous electrode models [65, 66].

Different CBM structures can be represented by systematically varying structural properties in the electrical network. The electrical potential and current can be calculated within this network. The charge transfer reaction, diffusion in the AM particles, and ionic diffusion and conductivity in the electrolyte are described based on the fully homogeneous electrochemical model approach. Both models are coupled via the current density at the reaction-nodes, i.e., the triple-phase boundaries. This hybrid model enables to directly study the impact of the complex electrical network structure and its degradation on the electrochemical performance of the battery. The combined hybrid model approach is visualized at the bottom of Figure 6.1.

In this work, a change of the transport in the liquid electrolyte phase due to CBM has not been considered, because the volume fraction of CBM is not varied and only a minor impact of this

variation on ion transport is expected. In principle, CBM structure could have an impact on tortuosity and position of the reaction sites. Though, the assessment of this aspect is out of scope for this work. The impact of change in CBM volume fraction and morphology on transport in the electrolyte has been studied, for example, by Mistry et al. [26].

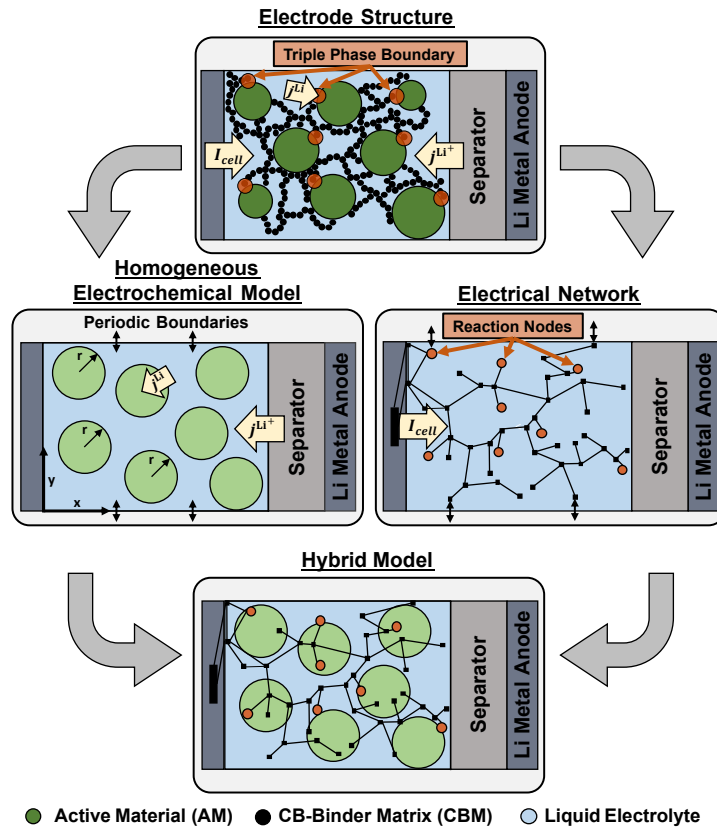


Figure 6.1: The hybrid model is established to represent the complex structure of the CBM in the porous electrode structure. The model consists of two parts: a homogeneous electrochemical model and a network-based model for the electrical charge transport.

6.2.2 Electrical network model

Electrons are transported from the current collector to the surface of the AM particles via a matrix consisting of CB and binder. This matrix forms a network-like structure in the porous electrode. By representing this matrix as an electrical network, the detailed impact of the related structure on the performance and degradation can be evaluated.

As a framework for the mathematical treatment of these networks, graph theory is applied which goes back to the 18th century and the mathematician Leonhard Euler [139, 140]. First, the definitions, notations, and basic quantities to describe the topology of networks are introduced. Then, the generation processes of the different network structures and the evaluation methodology of the electrical properties are briefly introduced.

The electrical network can be represented by a graph. Here, a directed graph $G = (\mathcal{N}, \mathcal{E})$ is used. The graph is defined by two sets \mathcal{N} and \mathcal{E} . The elements of $\mathcal{N} = \{n_1, n_2, \dots, n_N\}$ are the nodes of the graph and the elements of $\mathcal{E} = \{e_1, e_2, \dots, e_E\}$ are the edges. The number of elements in \mathcal{N} and \mathcal{E} are defined by N and E , respectively. The two sets are linked, as each element e_i in \mathcal{E} is defined by an unordered pair of elements n_j and n_k of \mathcal{N} . Here, $j \neq k$ which corresponds to a graph without self-loops. Nodes connected by an edge are referred to as adjacent. This adjacency between the nodes is represented in an adjacency matrix \mathcal{A} . This matrix is a $N \times N$ square matrix whose entries $a_{i,j}$ and $a_{j,i}$ are equal to one when an edge between the nodes n_i and n_j exists, and zero otherwise. The graph $G = (\mathcal{N}, \mathcal{E})$ can be completely described based on this matrix.

The degree or connectivity k_i of the node n_i is the number of its adjacent nodes and can be calculated based on the adjacency matrix \mathcal{A} as

$$k_i = \sum_{j=1}^N a_{i,j}. \quad (6.1)$$

A basic topological feature of a graph G is the degree distribution $P(k)$, which is defined as the fraction of nodes in the graph having the degree k . [141]

The degree distribution is used in this work as the main quantity to describe different topologies of electrical networks. Three fundamentally different distributions are analyzed in depth, introduced as homogeneous, scale-free, and random networks. The distribution of a scale-free network (SF) is described by a power-law defined as

$$P_{\text{SF}}(k) = a \cdot k^b, \quad (6.2)$$

with adjustable coefficients a and $b < 0$. The degree distribution of a random network (RND) is defined by a Gaussian distribution as

$$P_{\text{RND}}(k) = \frac{1}{\sigma\sqrt{2\pi}} e^{-\frac{(k-\mu)^2}{2\sigma^2}}, \quad (6.3)$$

with $\mu(k)$ the mean value and $\sigma^2(k)$ the variance of the degree. In case of the homogeneous network (H) a distinct degree k_H is applied for all nodes. The related degree distribution can be described by the following discontinuous function:

$$P_H(k) = \begin{cases} 1 & , k = k_H \\ 0 & , k \neq k_H \end{cases} . \quad (6.4)$$

Generation of the different network structures is challenging because the electrically conductive matrix has to be transferred into a graph, while spatial conditions must be preserved. The electrical connection between two nodes could be straight or possess some degree of tortuosity. Further, a connection could have a large or small cross-sectional area, which does impact the specific resistance. Here, the model is defined on a more abstract level, where detailed geometry and properties of the connections are lumped by a single homogeneous resistance. We further emphasize that the network topology is not sufficiently described by solely the degree distribution if the resistance is not equal for all edges. In this case, the network needs to be described by the vertex strength distribution. We note that, based on the presented approach, it is not reasonable to make statements concerning the absolute physical length, shape, and material properties of the connections themselves. However, this modeling approach enables to study the general impact of the connection structure without detailed information on the geometry and material properties.

The network generation process starts by distributing nodes in an electrode volume. Firstly, an initial number of nodes N_{RN} is distributed in the volume to divide it into equal cubic sub-volumes. These are the reaction-nodes (RN) and as such these nodes have sink and source terms describing the charge transfer occurring in this sub-volume. In the hybrid model it is required that the number of source and sink points must be equal in the homogeneous and electrical network model. While in the network model the source and sinks are discrete points, within the homogeneous models source and sinks are homogeneously distributed within the corresponding volume element. With this, the minimum number of nodes in the electrical network model is set. The volume correlated to each of these reaction-nodes V_{RN} is defined by

$$V_{RN} = \frac{V_{el}}{N_{RN}} , \quad (6.5)$$

with V_{el} being the electrode volume, and N_{RN} the number of reaction-nodes distributed within the electrode.

Depending on the selected number of reaction-nodes this yields the minimum resolution of the CBM. Fewer nodes correspond to coarser CBMs, i.e., few large CB agglomerates. In order to cover the impact of different agglomerate sizes on the electrochemical properties, the resolution of the electrical network can be varied. This is introduced in the electrical network model and

referred to as level of deagglomeration or resolution. Deagglomeration means that large CB particle agglomerates are broken into smaller segments while keeping a constant volume fraction of CB and binder. As a consequence, more fragmented electron conducting pathways are created. This effect is modeled by increasing the resolution of the network, i.e., increasing the number of nodes and edges. Based on the initial number of reaction-nodes N_{RN} , the sub-volumes are further divided by regular nodes. These nodes do not have sink and sources, but just distribute the current to the adjacent nodes. The total number of nodes N can be calculated based on a factor $L \in \mathbb{N}$, representing the non-dimensional level of deagglomeration, by

$$N = N_{\text{RN}} (2 \cdot L - 1)^3. \quad (6.6)$$

The implemented calculation scheme ensures that the electrode is divided into equal elements while the location of the reaction-nodes stays unaltered. In Figure 6.2, the concept is visualized in two dimensions. On the left, coarse CBM agglomerates are illustrated (top) and they are represented by only reaction-nodes in the network ($L = 1$). On the right, finer CBM agglomerates are displayed, and in the network the initial sub-volumes are further divided by regular nodes ($L = 2$). The number of reaction-nodes and their location is constant and they represent the same initial volume V_{RN} .

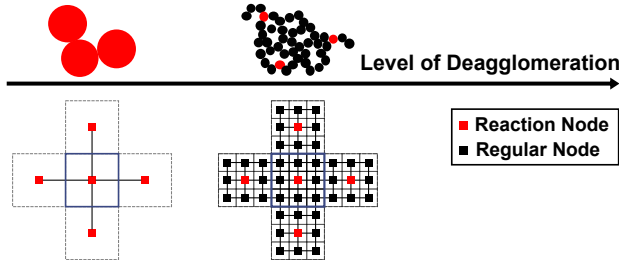


Figure 6.2: Visualization of node distribution. Increasing the level of deagglomeration yields finer CBM agglomerates. In the network this is represented by adding regular nodes, which increases the resolution of the network.

In the next step, regular nodes are added at the current collector ($x = 0$) and separator ($x = d_{\text{el}}$) to define the system boundaries. For these nodes, the same resolution in y - and z -direction is used as for the internal nodes. As such, the set of nodes \mathcal{N} is increased by the number of added boundary-nodes. A subset $\mathcal{N}_{\text{RN}} \subseteq \mathcal{N}$ exists with a number of reaction-nodes N_{RN} , which for all investigated networks corresponds to the initial volume V_{RN} as defined with eq. 6.5.

Edges of the network must be set to correspond to a particular network structure. In case of the homogeneous network, the nodes are connected to their spatial neighbors in the direction of the Cartesian coordinates (x, y, z) . Additionally, periodic boundaries are applied in the y - and z -direction, by connecting the first row with the last row of the nodes in the respective dimension.

In a three-dimensional space this leads to six adjacent nodes for each internal node. Hence, the distinct degree is $k_H = 6$ (see eq. 6.4) for all internal nodes. However, due to spatial boundaries, nodes exist with a distinct degree of five, i.e., the boundary-nodes at the current collector ($x = 0$) or separator ($x = d_{el}$).

Based on the homogeneous network the scale-free and random networks are generated. This is done by pruning and rearranging the existing edges. The locations of the nodes however do not change. The target is to modify the degree distribution to fit power-law distribution and Gaussian distribution for scale-free and random networks, respectively. For scale-free networks, the total number of edges is reduced by removing edges of highly connected nodes. If an edge is removed there is a chance to set a new edge to another close node to generate few highly connected nodes. This procedure is repeated until the target degree distribution is reached. For the random network, a node is picked randomly in the network and the degrees of the neighbor nodes are checked. Comparing the target distribution and local distribution an edge is removed and added. In case of the random network, this procedure is repeated until the global degree distribution of the network is close to the target degree distribution. At this point, it should be noted that the described procedures are realized in rather simple algorithms. Validity will be discussed in the results.

In the last step of the network generation, a master-node (MN) is added, which represents the current collector. The number of nodes N is increased by one, and a subset $\mathcal{N}_{MN} \subseteq \mathcal{N}$ exists representing this single master-node. Through this node, the electrical current is applied or extracted. The master-node is connected to all boundary nodes present at $x = 0$, thereby the current is distributed into the electrical network.

In this study, the electrical networks are analyzed based on different structural parameters, which are defined here. The path length λ , in general, is defined as the average of all possible shortest paths between two sets of nodes, including all possible combinations. This path length is not a physical length, but defined by the number of edges on the path between two nodes. Two different path lengths are analyzed: (I) the transit path length λ_{TP} between all boundary nodes at the current collector and separator, and (II) the path length to the reaction sites λ_{RN} between all reaction-nodes and the master-node. Furthermore, the number of transit edges connecting the current collector with the separator χ_{TP} is analyzed. This quantity is set to be the minimum number of cuts necessary to isolate the separator from the current collector.

In order to describe the conduction of electrons within the network, the resistances of the edges R_{Edge} and the network R_{Net} must be known. Equal resistance is assumed for all edges within a network. Please note that consideration of individual edge resistances due to difference in morphology would be possible. However, in this study this would impede to draw general conclusions about the impact of the network structure. The resistance of the edges connecting the boundary nodes with the master-node, however, is assumed to be very low to not affect the cell potential.

The edge resistance is adjusted to fit the conductivity of the network κ_{Net} according to the effective electrical bulk conductivity, $\kappa_{\text{s,eff}}$, being a parameter in the homogeneous electrochemical model. The resistance of the network R_{Net} can be calculated based on the conductivity of the network, the layer thickness of the electrode d_{el} , and the area of the electrode A_{el} by

$$R_{\text{Net}} = \frac{1}{\kappa_{\text{Net}}} \frac{d_{\text{el}}}{A_{\text{el}}}. \quad (6.7)$$

Furthermore, the resistance of the network is defined by

$$R_{\text{Net}} = \frac{\Delta\phi_{\text{cc-sep}}}{I} = \frac{\phi_{\text{cc}} - \phi_{\text{sep}}}{I}, \quad (6.8)$$

and is proportional to the edge resistance. Here, $\Delta\phi_{\text{cc-sep}}$ is the potential difference between the current collector (cc) and the separator (sep) and I is the applied electrical current. Solving the linear equation system evolving from Ohm's law gives the potential drop in the electrode. For detailed information about solving this, it is referred to Cocco et al. [133]. In order to estimate the network resistance, it is assumed that the applied current is $I = 1 \text{ A}$ and $\phi_{\text{sep}} = 0 \text{ V}$. This assumption simplifies eq. 6.8 to

$$R_{\text{Net}} = \frac{\phi_{\text{cc}}}{1 \text{ A}}. \quad (6.9)$$

Eq. 6.7-6.9 are solely used to identify edge resistance R_{Edge} based on the effective electrical bulk conductivity $\kappa_{\text{s,eff}}$ and thus are not part of the hybrid model.

The electric charge transport in the electrical network is given by

$$J^{\text{tot}} = K \cdot \phi_{\text{s}}, \quad (6.10)$$

with K a $N \times N$ matrix being the conductance matrix, which is given as

$$K = La \cdot \Omega, \quad (6.11)$$

where Ω is a $N \times N$ diagonal matrix whose entries are the reciprocal of the estimated edge resistances R_{Edge} . The Laplacian matrix $La = \mathcal{D} - \mathcal{A}$, with \mathcal{D} a $N \times N$ diagonal matrix whose entries are the respective node degrees k_i [141]. The solid phase potential ϕ_{s} is given by a $1 \times N$ vector, and J^{tot} is the resulting $1 \times N$ vector, describing the total current generated at the nodes. In the hybrid model, this matrix-based definition of Ohm's law, i.e., eq. 6.10, substitutes eq. 2.5 in the homogeneous model. Coupling the two models is done via the reaction-nodes. In the

network model, the absolute currents are considered. According to that, three different cases must be distinguished for the absolute total current generation J^{tot} :

$$J_i^{\text{tot}} = 0 \quad \forall \quad i \notin \mathcal{N}_{\text{RN}} \wedge \mathcal{N}_{\text{MN}} \quad (6.12)$$

$$J_i^{\text{tot}} = I_{\text{cell}} \quad \forall \quad i \in \mathcal{N}_{\text{MN}} \quad (6.13)$$

$$J_i^{\text{tot}} = \int J_i^{\text{tot}} dV_{\text{RN},i} \quad \forall \quad i \in \mathcal{N}_{\text{RN}}. \quad (6.14)$$

The Eqs. 6.12-6.14 cover the already introduced assumptions of the electrical network:

- Eq. 6.12: Electrical current is distributed by regular nodes, but no source and sink terms are present
- Eq. 6.13: Electrical current is applied at the master-node, representing the current collector
- Eq. 6.14: The volume rate of total current generation j^{tot} in a given node calculated in the homogeneous model is integrated over the volume V_{RN}

The last point results in the absolute electrical current entering or leaving the electrical network. This enables to directly couple the electrical network model with the homogeneous electrochemical model, which allows studying the effect of different electrical network structures on the overall electrochemical performance. In this work, the performance is rated by the volumetric energy density Q . The impact of the electrical network on the transport processes in the electrolyte is neglected in this work as discussed previously.

The hybrid model can be applied to evaluate electrical networks with several thousand nodes and edges. Solving the differential equation system of a heterogeneous network is challenging and time-consuming. Especially, at low voltages, i.e., in this study below 3.1 V, the time steps need to be rather short for numerical solution, which yields high computational cost. Small networks with a low level of deagglomeration can be solved in a few minutes while the run time of large networks can take up to a few hours. Further, computational cost depends on the structure of the network. To create a compromise between computational cost and a sufficient number of simulation for statistical evaluation of the networks, the cut-off voltage was set to 3.1 V for all conducted electrochemical simulations. The reference measurements and the model parametrization displayed in Appendix A.3 were done down to a voltage of 3.0 V.

6.3 Results

The hybrid model enables to study how the electrical network affects energy density, degradation, and failure of a lithium-ion battery. The focus is laid on establishing a mechanistic understanding and to identify structural network parameters that are most relevant for optimization of the

CBM. For this purpose, homogeneous, random, and scale-free networks are analyzed. The obtained results are structured as follows. First, the generated network structures and the electrical properties are discussed. In the second part, the performance of the generated networks is rated in terms of the volumetric energy density, and the effect of a varying network structure on performance uncertainties is discussed. Lastly, the degradation of scale-free and random networks is analyzed by rating the impact of a random-based edge removal. The electrochemical simulations and graph analysis are implemented in MATLAB vR2018b.

6.3.1 Structural network properties

Generating the artificial electrical networks is challenging since fundamentally different network structures are aimed at while networks must maintain the spatial allocation. Here, the applied initial settings and the resulting network structures are discussed since they have an impact on cell performance and degradation, investigated in the following.

The assessed electrode volume is assumed to be cubic with spatial extensions equal to the cathode layer thickness d_{el} . Five reaction-nodes are equally distributed in each of the Cartesian directions. Following eq. 6.6, the total number of internal nodes in the network can be calculated. Here, the maximum considered level of deagglomeration is $L = 4$. Scale-free networks are generated by targeting the degree distribution as given with eq. 6.2. The coefficients are set to $a = 0.65$ and $b = -2.5$. The value for b is chosen based on the definition of scale-free networks given by Boccaletti et al. [141]. Random networks are generated based on the distribution function as given with eq. 6.3. The mean value and standard deviation are chosen as $\mu = 5$ and $\sigma = 2$, respectively. Since the generation process for scale-free and random networks is based on a stochastic algorithm, the impact is evaluated by generating multiple networks. For each level of deagglomeration, 100 networks are created.

In Figure 6.3, the degree distributions of homogeneous, random, and scale-free networks at a level of deagglomeration of $L = 1$ are displayed. For random and scale-free networks, values are averaged and the standard deviation is indicated. The targeted degree distributions based on the previously initialized equations are indicated by the solid and dashed lines. For each network an exemplary structure is visualized. It should be noted that the depicted networks display the structure, but the nodes are not spatially aligned as in the electrode volume. This results in rather abstract representations of the networks. For all displayed data and structures the master-node is excluded and periodic boundaries are included. In case of the homogeneous network, the majority of the nodes have a degree of $k = 6$. The nodes with a degree of $k = 5$ are located at the current collector or separator, i.e., these are the boundary nodes. It can be seen that the homogeneous network is characterized by an ordered structure. Based on the generation process it corresponds to a regular cubic structure. Due to the application of periodic boundaries in y- and z-direction a tube-like structure evolves. The scale-free networks reach the specified power-law

degree distribution with good accuracy. The network forms a large number of poorly connected satellites with a degree equal to one. Simultaneously a few important hubs are created with a high degree. This structure is characteristic for scale-free networks [141]. The averaged degree distributions of the random networks show approximately the Gaussian distribution as defined by the target function. The Gaussian degree distribution leads to a randomized structure with a variety of differently connected nodes. As can be seen, the structures can be clearly distinguished from each other.

Increasing the value of L leads to more nodes and edges in the same electrode volume and thus yields higher resolution and more complex structures. This represents more fragmented electron-conducting pathways and smaller CBM agglomerates. Generating networks for higher values of L results in similar distributions. In case of the scale-free and random networks the quality of the generation process improves. The difference between the average degree distributions and the targeted distribution decreases and standard deviation also decreases.

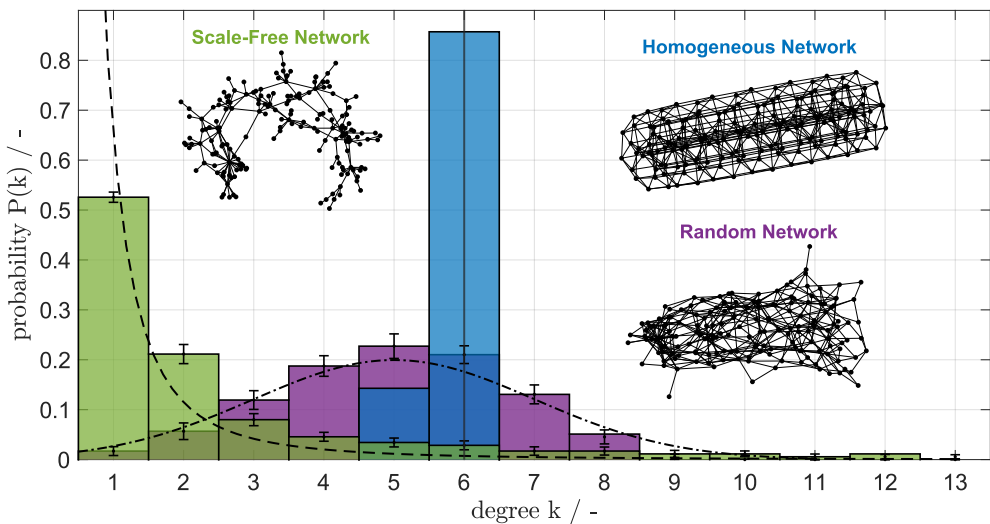


Figure 6.3: The degree distributions of the three generated networks structures compared to the targeted degree distributions initialized by Eqs. 6.2-6.4 for $L = 1$. The degree distributions of scale-free and random networks are averaged and standard deviation is indicated. For each distribution a resulting network structure is displayed.

The generation of the scale-free and random networks has an effect on the respective number of edges, due to the edge pruning. The correlation between the number of nodes and edges for each network structure is displayed in Table 6.1. All structures contain the same number of nodes for the same level of deagglomeration. Comparing the number of edges of the three networks reveals that the homogeneous network has the highest number of edges and the scale-free network the lowest. The standard deviation with respect to the number of edges is relatively small (0.1–3%)

for the random and scale-free networks.

Table 6.1: Correlation between the number of nodes and the number of edges for each network structure at different levels of deagglomeration L . Values for scale-free (SF) and random networks (RND) are averaged, the standard deviation is provided.

L	N	E_H	E_{RND}	E_{SF}
1	176	525	447 ± 12	222 ± 7
2	3826	11475	9635 ± 78	4711 ± 28
3	16876	50625	42306 ± 151	20495 ± 52
4	45326	135975	113278 ± 266	54761 ± 98

To sum up, it can be seen that three network structures have been created based on degree distributions, being clearly qualitatively and quantitatively distinguishable. Further structures with comparable properties have been reproduced in a stochastic process.

6.3.2 Electrical network properties

The electrical properties of the previously generated networks are evaluated and discussed.

The edge resistances of the networks are estimated to reach an average network conductivity for the respective set of networks. This average network conductivity is set to be equal to the effective electrical bulk conductivity introduced in the homogeneous electrochemical model. Each edge resistance for networks with the same level of deagglomeration and same structure are defined as equal. However, individual network conductivity can deviate due to stochastic differences in the network structure as introduced in the previous section.

The electrical network conductivity is strongly dependent on the conductive paths from the current collector to the separator [142]. Therefore, it is of interest to evaluate conductivity with respect to these paths. Here, the focus is set on two structural network properties: (I) the number of transit edges χ_{TP} and (II) the transit path length λ_{TP} . These quantities were defined earlier.

In Figure 6.4, the network conductivity is displayed versus the two network properties. In Figure 6.4a, the conductivity is plotted versus the number of transit edges χ_{TP} and in Figure 6.4b against the transit path length λ_{TP} . The conductivity of the homogeneous electrical network is per definition constant for all number of nodes. Further, the average network conductivity is also constant for random and scale-free networks, which is the consequence of the definitions given above. Therefore, the difference between the networks is concerning the deviation of the conductivity. The scale-free networks in general yield higher deviations for the network conductivity compared to the random networks. In both network types, the deviation decreases with an

increasing number of nodes, i.e., increasing the level of deagglomeration, L .

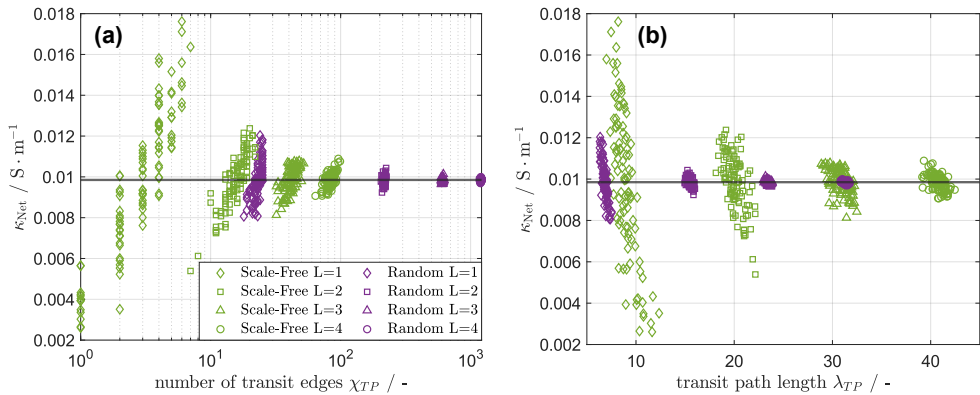


Figure 6.4: In (a) the network conductivity versus the number of transit edges χ_{TP} is shown. In (b) the network conductivity is plotted against the transit path length λ_{TP} . The solid black line indicates the average network conductivity. Single points correspond to one of 500 different network structures for a given L and type.

Comparing scale-free networks to random networks reveals that the number of transit edges χ_{TP} is significantly lower for scale-free networks, as can be seen in Figure 6.4a. In particular at $L = 1$ scale-free networks have only between one and seven transit edges connecting the current collector and the separator. Networks with an increased number of transit edges result in a steep increase in electrical network conductivity. Therefore, the deviation of the conductivity is high for scale-free networks at low level of deagglomeration.

Concerning the transit path length λ_{TP} , it can be seen that random networks establish shorter paths, as can be seen in Figure 6.4b. The satellite nodes formed by scale-free networks yield a disruption of continuous paths. While in case of the random network, only a few nodes exist, which act as dead ends for the transit paths. The deviation of the transit path length is higher for scale-free networks, resulting in increased deviations of the conductivity. The observed correlation between the transit path length and the network structure shows good agreement with literature results comparing small-worlds, and random networks [143].

Increasing the level of deagglomeration results in an increasing number of transit edges for both network structures. Nevertheless, the random network always has higher number of transit edges. The transit path length defined by the number of passed edges also increases. Note that the geometric distance is constant, but more edges are added for higher level of deagglomerations. Random networks always have shorter transit paths and the difference between the two network structures increases. Overall, increasing the resolution of the network, the structures become more uniform and robust, and thus the deviation of the electrical conductivity decreases.

Hence, for achieving high and consistent electrical conductivity it is important to create network structures that yield a high number of independent conductive paths routing from the current

collector to the separator and structures that have preferentially short transit paths. This can be achieved by overall high connectivity. Furthermore, it can be concluded that smaller agglomerates result in an increased resolution of the CBM network. This results in a more consistent network conductivity, due to more and shorter conductive paths between the current collector and the separator. Highly dispersed CBM agglomerates are beneficial to achieve more robust electrical properties because a highly connected electrical network can compensate defects in the network structure, which is quite intuitive and supported by experimental findings [48, 144]. Moreover, Mistry et al. [26] showed that the structure of the CBM network has an impact on the electrical conductivity. They identified that fingerlike morphologies have poor electrical conductivity. This morphology could be related to the scale-free networks analyzed here.

In Table 6.2, the estimated edge resistances for the different levels of deagglomeration and network structures are displayed. The edge resistances for the random networks are slightly lower but similar to the homogeneous network. Here, the edge resistance must compensate for the fact that random networks have in general fewer edges to achieve the same average network conductivity (see Table 6.1). To obtain the same average conductivity the edge resistance of the scale-free network need to be much lower in comparison to the other network structures. However, this can not be explained solely by fewer edges but is a structural effect of the network. Scale-free networks tend to form isolated satellites and only a few highly connected hub nodes. The previously discussed results already showed that this leads to only a few, but very important conductive edges that establish the network conductivity. In order to reach the target network conductivity, edges need to have very low resistances.

Table 6.2: Estimated average edge resistances for each network structure, homogeneous (H), random (RND), and scale-free (SF), at different levels of deagglomeration.

L	$R_{\text{Edge,H}} / \text{M}\Omega$	$R_{\text{Edge,RND}} / \text{M}\Omega$	$R_{\text{Edge,SF}} / \text{M}\Omega$
1	10.47	9.16	1.72
2	31.40	29.59	3.10
3	52.33	50.32	4.66
4	73.26	70.83	6.54

To conclude, several networks have been generated, which have the same average network conductivity but differ concerning the standard deviations. Even more, pronounced different network structures significantly defer for the required edge resistance as a consequence of aligning the effective bulk conductivity. The scale-free network are especially interesting in terms of bottlenecks while the random network do not tend to form these special edges, but are defined by rather short transit paths. It is emphasized that all networks proposed here would result in electrodes

with the same mean effective conductivity, which is commonly used as a quality parameter of electrodes [145].

6.3.3 Influence of percolation on electrical conductivity

In Chapter 5, the electrochemical p2D model was extended by empirical equations for the effective transport parameters. The correlations were estimated by Laue et al. [15, 27] based on artificial electrode structures. Especially for the electrical conductivity, it was identified that changing the volume fraction of the AM and the CBM results in percolation of the CBM. In detail, increasing the volume fraction of the CBM results in a steep increase in electrical conductivity as soon as a continuous path along the CBM is established from one side of the electrode to the other. The electrical current is transported mainly along with the CBM phase, as it has a significantly higher electrical conductivity.

Analyzing the electrical properties of the different network structures revealed that especially the number of transit edges and the length of the transit path have an impact on the electrical network conductivity (see Figure 6.4). Enhancing the number of transit edges results in reproducible and in general higher network conductivity. Consequently, also for the electrical networks analyzed in this chapter the percolation is identified as important for improving the transport of the electrical current. However, in this study, the conductivity of the active material is neglected. Thus, there is no lower limit in the electrical conductivity, which is ensured by the AM. Furthermore, the resolution of the electrical networks analyzed here is significantly lower compared to the artificial electrodes. There, several hundred thousand voxels are considered, which lead to significantly more complex networks with more edges and paths.

Comparing the results estimated by Laue et al. [27, 33] based on artificial electrode structures and the systematical analysis of electrical networks done here indicates that combining the two approaches would be of interest. Generating artificial electrodes with realistic CBM structures could be reduced to networks. Thus, network properties could be analyzed dependent on the structural features of the electrode. Especially, the effect of percolation could be studied. Furthermore, it could be possible to distinguish between the network established by the AM and the CBM and its interaction.

6.3.4 Estimation of uncertainties in the cell performance

The generated network structures are used for the electrochemical simulations with the hybrid model. The electrical properties estimated in the previous section were applied to these simulations. The detailed cell structure, materials, and implemented parameters are given in Table A.2 and A.5, in the appendix. The delithiation process was simulated at a current density of

$i = 6 \text{ mA cm}^{-2}$ (approx. 2.5 C) until a lower cut-off voltage of $V_{\text{cut}} = 3.1 \text{ V}$ is reached. As discussed previously, the cut-off-voltage has been set to this value to reduce the computational cost. Additionally, due to high computing times, the electrochemical simulations were performed for electrical networks up to $L \leq 3$. However, in general, higher resolutions are possible.

The scale-free and random networks, unlike the homogeneous network, do not have a constant volumetric energy density. Due to differences in the structure and electrical properties, deviations occur in the electrochemical performance. The aim is to identify advantages and disadvantages based on the networks investigated. The levels of deagglomeration of $L = 1$ and $L = 3$ are of special interest as the standard deviation of the electrical network conductivity of the random network with $L = 1$ is comparable to the scale-free network with $L = 3$, as can be seen in Figure 6.4. This denotes that those CBMs would not be distinguishable by bulk conductivity measurements.

In Figure 6.5a, the impact of the network conductivity on the volumetric energy density of scale-free networks is depicted. Firstly, the focus is on scale-free networks with $L = 1$. In general, increasing the electrical network conductivity yields an increasing volumetric energy density Q of the simulated half-cell batteries. At the same time, more consistent quality can be seen. This is in good agreement with the literature, as experimental studies have shown that higher electrical conductivity contributes to more consistent battery cell quality [49]. Below a network conductivity of 0.09 S m^{-1} , the volumetric energy density is limited due to overall low network conductivity. Here, the difference in the network conductivity results solely in the structure of the network, as the edge resistance is consistent for all networks at $L = 1$. Previously, the network conductivity was discussed concerning bottlenecks. Therefore, the number of transit edges χ_{TP} is visualized by coloring the markers in the figure. A small number of transit-edges results in low network conductivity and thus in low volumetric energy density. Nevertheless, as can be seen, in particular networks with only one transit edge show strong deviations concerning the volumetric energy density.

Three networks are analyzed that have a pronounced bottleneck, i.e., only one transit edge, but differing volumetric energy densities. In Figure 6.5b, a scale-free network is visualized that has a volumetric energy density of 1236.8 Wh l^{-1} . The reaction-nodes in the network are colored concerning the normalized concentration X_{Li} , which is defined as $X_{\text{Li}} = c_{\text{s}}(R_{\text{P}})/c_{\text{s,max}}$, with $c_{\text{s}}(R_{\text{P}})$ the lithium concentration at the surface of the AM particles and $c_{\text{s,max}}$ as the maximum possible lithium concentration in the AM. X_{Li} is displayed for the end of delithiation. The AM particles close to the current collector and in front of the bottleneck have a high normalized concentration. Behind the bottleneck, X_{Li} is considerably lower. Due to the bottleneck, electrons have high resistance to reach areas close to the separator and this is prohibiting the electrochemical reaction. Overall, this results in inhomogeneous intercalation and explains the drop of the volumetric energy density.

The networks are additionally analyzed concerning the location of the bottleneck and the path

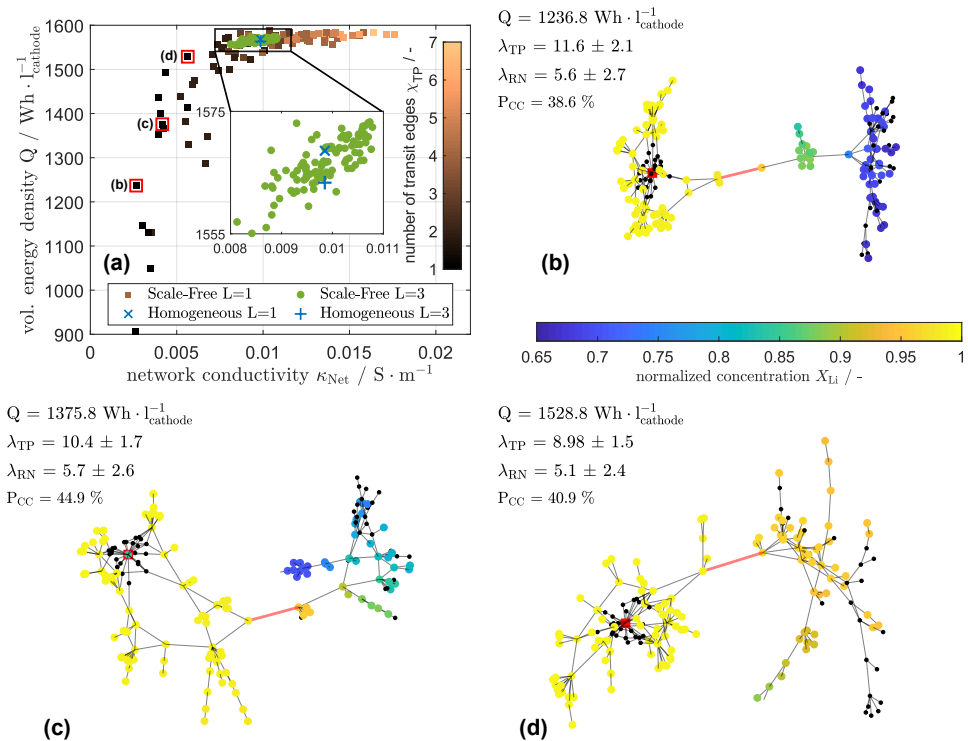


Figure 6.5: In (a) the volumetric energy density Q of scale-free networks with $L = 1$ and $L = 3$ are plotted. The colors of the markers for $L = 1$ indicate the number of transit edges χ_{TP} in the respective network. In (b), (c), and (d) selected networks are examined in more detail. The reaction-nodes are colored concerning the normalized concentration X_{Li} at the end of delithiation. The boundary-nodes at the current collector and separator are the black nodes. The red node is the master-node at the current collector. The red edge is the identified bottleneck edge. Additionally, the percentage of AM close to the current collector P_{CC} , the transit path length λ_{TP} , and the path length to the reaction sites λ_{RN} are provided for the respective networks.

length to the reaction sites. The location was rated by the percentage of AM particles well connected to the current collector and in front of the bottleneck P_{CC} . For the network structure shown in Figure 6.5b this value is 38.6 % and thus most of the AM is poorly connected. The path length to the reaction sites λ_{RN} is given. The quantity was defined earlier. In Figure 6.5b, λ_{RN} is 5.6 and the standard deviation is around 2.7. In Figure 6.5c, a network with a volumetric energy density of 1375.8 Wh l^{-1} is shown. This is slightly higher than for the network shown in Figure 6.5b. This correlates with a higher percentage of AM in front of the bottleneck ($P_{\text{CC}} = 44.9\%$). Nevertheless, a strongly inhomogeneous charge behavior of the cathode is observed due to the effect of the bottleneck. The path length to the reaction sites is comparable to the network in Figure 6.5b.

In Figure 6.5d, a network with a volumetric energy density of 1528.8 Wh l^{-1} is plotted. This is

one of the highest values reached for scale-free networks with only one transit edge. However, the percentage of AM close to the current collector is with 40.9 % slightly lower than for the network in Figure 6.5c. In comparison to the previous networks, the normalized concentration X_{Li} of the different AM particles is nearly uniform and the bottleneck seems to have less of an effect on the volumetric energy density. Compared to the two previous networks, this network only has one edge defining the bottleneck. The rest of the network is overall well connected. In the other networks, several consecutive edges create the bottleneck. Therefore, this is the main reason for the network to still achieve a reasonable volumetric energy density. The path length to reaction sites is with 5.1 edges the lowest value of the three networks. This suggests that the network is comparable well connected and the paths from the nodes where the reactions occur to the current collector, providing the electrons, are rather beneficial for the quality of the battery cell.

Increasing the level of deagglomeration, as shown in Figure 6.5a, results in reduced deviations of the network conductivity and thus in lower deviations of the volumetric energy density. The network structure is more homogeneous and the number of transit edges is relatively high and thus its effect on the electrochemical properties is reduced. The volumetric energy densities of the homogeneous networks for both levels of deagglomeration are indicated and the results presented for the scale-free networks are comparable to the volumetric energy density of the homogeneous networks.

To sum up, the analysis of the scale-free networks already allows first insights into the behavior and effects of the electrical network structure on the performance of lithium-ion batteries. Avoiding bottlenecks is crucial for high-quality batteries. Nevertheless, the intensity and location of the bottleneck have a significant effect. Only one transit edge, like in Figure 6.5d does not have a devastating effect on the volumetric energy density if the rest of the battery is well connected. In Figure 6.6a, the volumetric energy density of lithium-ion batteries with random electrical networks are depicted against their network conductivity. Comparing random networks with scale-free networks, it can be seen that they have considerably lower deviations. More precisely, the random networks at $L = 1$ lead to deviations in the same range as scale-free networks at $L = 3$. This was to be expected, as the deviations of the network conductivity are also comparable between those two (see Figure 6.4).

Due to the overall relatively high network conductivity, no significant effect on the volumetric energy density occurs for random networks. At $L = 1$, the volumetric energy density slightly increases with an increasing network conductivity. Moreover, a lower boundary of the volumetric energy density for a given network conductivity can be seen. Note that in contrast to Figure 6.5a, here the transit path length λ_{TP} is indicated by the colored markers for random networks with $L = 1$. This quantity was analyzed in Figure 6.4b and the network conductivity is sensitive to this quantity. The number of transit edges is not considered because no bottlenecks occur in random networks.

In Figure 6.6b-d, three selected random networks are analyzed in depth, which have comparable network conductivity, but differing volumetric energy densities. All three networks show a homogeneous distribution of the normalized concentration X_{Li} , compared to the results of the scale-free networks shown previously. Areas that cannot be sufficiently supplied with electrons cannot be identified. For all networks, the transit path length λ_{TP} , and the path length to the reaction sites λ_{RN} are provided. Comparing these values it can be concluded, that the transit path length of the electrode is an indicator for a well-connected network and good conductivity. However, even more important is the path length to the reaction sites. This is a good indicator for a good supply of electrons to the reaction sites. Nevertheless, the network structure is complex and multiple structural properties affect the electrochemical properties, and though it is difficult to identify a single important quantity.

Increasing the level of deagglomeration for random networks results in lower deviations of the network conductivity and volumetric energy density. The average energy density of the random networks is slightly lower than for lithium-ion batteries with homogeneous networks.

To sum up, the discussed results concerning the volumetric energy density, reveal that the structure of the electrical network within the electrode is crucial. Understanding the effect of the structural properties can help to design networks with better overall performance. The analyzed random networks show advantageous performance in comparison to the scale-free networks due to a reduced deviation of the volumetric energy density. The comparison reveals that bottlenecks within the electrical network are devastating for the performance of the battery. Therefore, random networks show a more consistent quality because the probability of creating such a bottleneck is very low. Additionally, the results show that solely comparing the network conductivity is not sufficient to rate the electrical network. Additionally, it is important that the various reaction-nodes within the electrode are well and close connected to the current collector. This requires not only good interconnection from the current collector to the separator, but also good interconnection in between the reaction areas, i.e., reaction-nodes. A similar result has been obtained by Nakajo et al. [146]. They studied electrochemical materials and showed that the connection of the triple phase boundary is important to obtain good performances.

6.3.5 Degradation of the electrical network and cell failure

In addition to analyzing the volumetric energy density during the delithiation process, the hybrid model also enables to study the impact of a degrading electrical network on the electrochemical properties of a lithium-ion battery. The degradation of the electrical networks is modeled by an iterative edge removal. Firstly, the volumetric energy density is determined based on the initial state of the electrical network using the hybrid model. Then in each step, approximately 5 % of the initial number of edges are removed and the simulation is repeated with the decomposed electrical network. The edges are picked on a random basis. Edges connecting the boundary

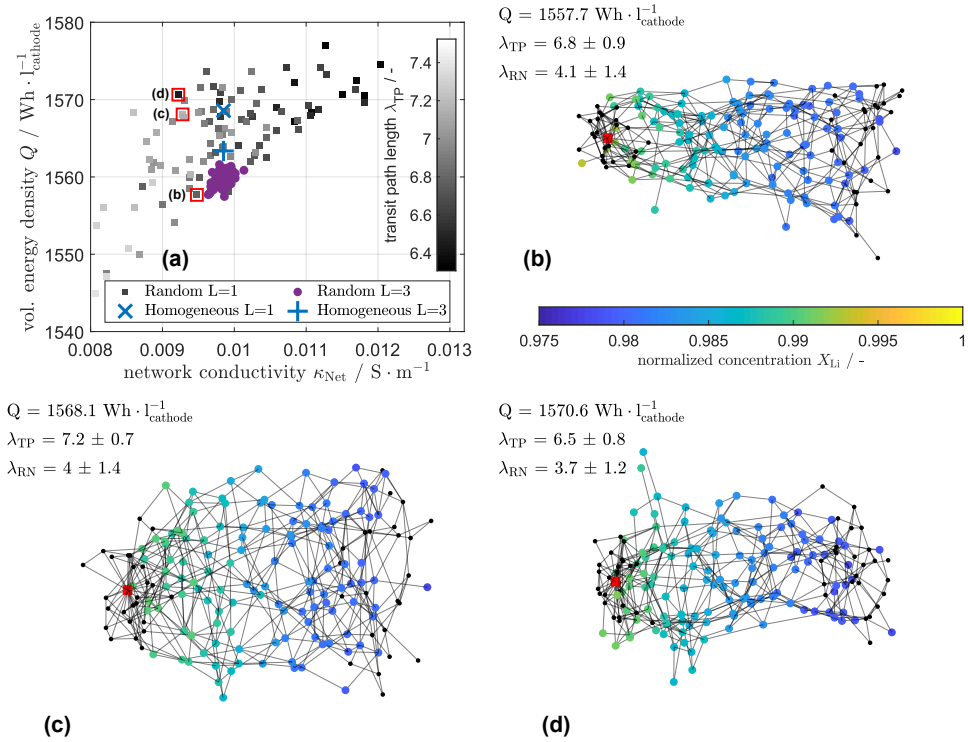


Figure 6.6: In (a) the volumetric energy density Q of random networks with $L = 1$ and $L = 3$ are plotted. The colors of the markers for $L = 1$ indicate the transit path length λ_{TP} in the respective network. In (b), (c), and (d) selected networks are examined in more detail. The reaction-nodes are colored concerning the normalized concentration X_{Li} at the end of delithiation. The boundary-nodes at the current collector and separator are the black nodes. Additionally, the transit path length λ_{TP} , and the path length to the reaction sites λ_{RN} are provided for the respective networks.

nodes and the master-node are excluded. The decomposition of the network is inspired by a cascade failing procedure for complex networks taken from literature [147]. The simulations are performed with the same current density and within the same voltage range as introduced in the previous section. Here, degradation is mainly analyzed for scale-free and random networks with $L = 3$. Ten different electrical networks are randomly picked and simulated to map evolving uncertainties. The relative amount of remaining volumetric energy density q is defined as

$$q(\beta) = \frac{Q(\beta)}{Q_{\text{Initial}}} \cdot 100\%, \quad (6.15)$$

with β being defined as the relative amount of removed edges, $Q(\beta)$ being the remaining volumetric energy density after β amount of edges are removed, and Q_{Initial} being the initial volumetric energy density of the pristine network.

In Figure 6.7a, the effect of the random edge removal on the volumetric energy density is displayed for random and scale-free networks. The two network structures show significantly different robustness to the edge removal. For scale-free networks, even low relative amount of removed edges β leads to a noticeable decrease in volumetric energy density. Removing 10–15 % of the edges, already results in only $q = 80\%$ remaining volumetric energy density. Afterwards, the reduction of energy density of scale-free networks is nearly linear. Towards the end, i.e., after more than 35 % removed edges, the decrease in volumetric energy density is slowing down. In comparison, the volumetric energy density of a lithium-ion battery with a random network remains nearly constant over a longer period of time. Until 20 % of the edges are removed the performance of the battery is almost constant. Moreover, 80 % of the volumetric energy density can be withdrawn when already 40 % of the edges are removed. However, the reduction of volumetric energy density is accelerating when more edges are removed, resulting in a sudden-death-like behavior, which has already been observed for lithium-ion batteries [148]. After removing about 60 % of the edges for both networks, almost no energy can be withdrawn from the batteries. Please note that in this study it was assumed that the AM does not contribute to the electrical conduction. If there is a significant contribution of the active material, the energy densities would not go to zero even for fully degraded CBMs. Instead, a low energy density would remain.

The colored areas show the range of uncertainty, i.e., highest and lowest volumetric energy densities. Further, some lines are added for exemplary degradation progressions for particular networks. It can be seen that the scale-free network also leads to higher deviations in degradation while the random network gives more reproducible results. These results show that the two networks behave very differently during degradation due to edge removal. In the previously discussed results it was already shown that the network conductivity has an impact on the volumetric energy density and that the connection of the reaction-nodes is essential. Therefore, in the following, it will be analyzed how these two aspects change due to edge removal.

The removal of edges in the electrical network decreases the connectivity of the nodes. This can reduce the number of conductive paths, which yields decreasing network conductivity, as shown previously in Figure 6.4. Further, single nodes and parts of the network can be detached. This is in particular important when the separated parts contain reaction-nodes, as thus active material is isolated and capacity is reduced. Using results shown in Figure 6.7b and c, these aspects are studied. Additionally, in Figure 6.8, an exemplary degradation of scale-free and random networks is shown visually for $L = 2$. Note that no fundamental differences in terms of degradation are present between $L = 2$ and $L = 3$. However, for improved visibility the lower level of deagglomeration is plotted. The difference between $L = 2$ and $L = 3$ in terms of the degradation is briefly discussed in Appendix C. In Figure 6.7b and c, the relative amount of isolated reaction-nodes and the network conductivity are shown in correlation to the relative amount of removed edges β for $L = 3$, respectively. As can be seen, with no edges removed, all networks have a comparably high network conductivity and the relative amount of isolated active material is equal to zero.

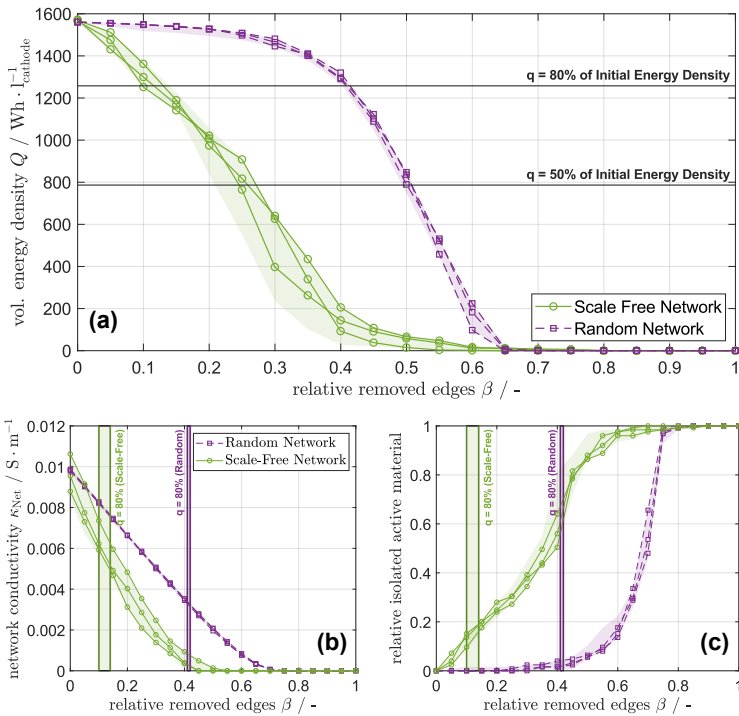


Figure 6.7: In (a) the decrease of the volumetric energy density Q with respect to the relative amount of removed edges β for random and scale-free networks at $L = 3$ is shown. In (b) the effect of the random-based edge removal on the network conductivity is displayed and in (c) the effect on the isolation of the active material due to unconnected reaction nodes is shown by the relative amount of isolated reaction nodes. Areas where the remaining volumetric energy density $q = 80\%$ and $q = 50\%$ is reached are provided for both network types. The colored area represents the deviation of the degradation and always three exemplary degradations are displayed.

In Figure 6.7b, it can be seen that the electrical conductivity of random networks is significantly reduced at a remaining volumetric energy density of $q = 80\%$. In contrast, at this state almost no active material is isolated, as can be seen in Figure 6.7c. This is also confirmed with Figure 6.8. At $q \approx 80\%$ remaining volumetric energy density, i.e., structure shown in the center, only a few reaction-nodes are isolated from the random network. This denotes that the removal of edges mainly yields a thinning of connections and therefore a decrease of the efficient electrical conductivity of the network. Further, it can be seen that electrical conductivity declines linearly with percentage of removed edges. In contrast, the slope of volumetric energy density is not constant, but becomes steeper, which indicates an increasing sensitivity to electrical conductivity. The degradation of scale-free networks is fundamentally different compared to random networks. In Figure 6.7c, it can be seen that a decline of 20% in volumetric energy density, i.e., $q = 80\%$, correlates with a loss of almost 20% of the reaction-nodes. This indicates that for scale-free networks loss of reaction-nodes is the dominant cause for the reduction of energy density. The

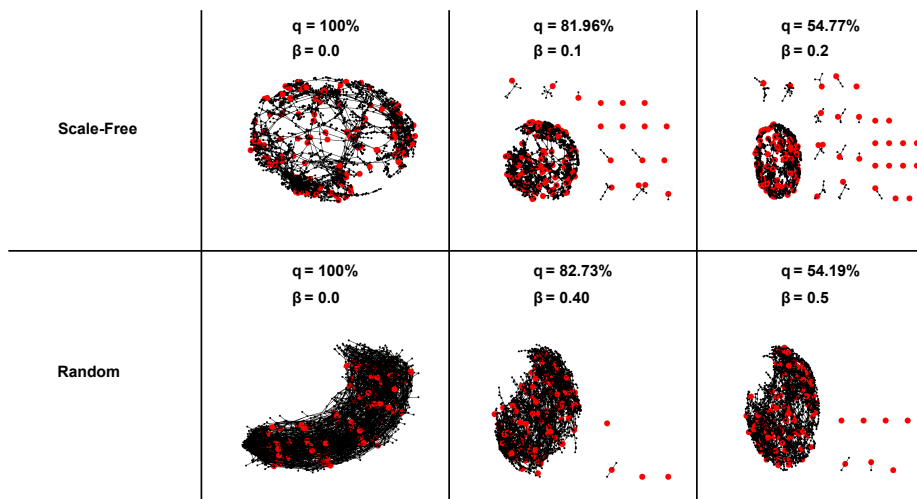


Figure 6.8: Visual degradation of networks at a level of deagglomeration of $L = 2$ is displayed. Networks are displayed in the initial states and at $q \approx 80\%$ and $q \approx 50\%$ remaining volumetric energy density and the relative amount of removed edges β is provided for all networks. The red nodes are the reaction-nodes.

disconnection of nodes yields a fast decomposition of the network, which is also confirmed with the decomposed structures shown in Figure 6.8. The underlying cause for this can be given based on the degree distribution. The degree distribution of scale-free networks indicates that a high amount of nodes with only one edge exists. Removing edges within the network results in an immediate isolation of these nodes. However, also the electrical conductivity is significantly decreasing due to edge removal as can be seen in Figure 6.7b. The slope is even more significant compared to random networks. However, at $q = 80\%$ remaining volumetric energy density the electrical conductivity of scale-free networks is higher compared to random networks.

To sum up, it has been demonstrated that the impact of removal of edges, i.e., conductive pathways, significantly depends on the electrical network structure. Scale-free structures mainly degrade due to loss of reaction-nodes, i.e., isolation of active material. Random networks mainly degrade due to thinning of conductive paths and consequently a decline of electrical conductivity. The major advantage of well connected random network structures is their robustness against isolation of active material, which yields significantly improved degradation behaviour. Moreover, the degradation is subject to less deviations. Most importantly, with the presented results it is demonstrated that neither electrical conductivity and its distribution nor the electrochemical performance of a fresh cell is a useful indicator for robustness against edge removal, i.e., removal of conductive paths, and thus degradation of a cell. Here, more complex structural properties of the electrical network play a major role and need to be considered. Therefore, it is emphasized that novel methods to characterize electrical network structure are needed.

6.4 Concluding remarks

In this chapter, the impact of complex electrical networks on cathode delithiation behavior, degradation, and failure is discussed. Different structures have been evaluated in a simulation study for the first time. For this purpose a novel hybrid model approach have been introduced.

Three fundamentally different network structures are analyzed in detail: homogeneous, random, and scale-free. The degree distributions of these networks differ, and this results in very different structures and properties. Comparing scale-free and random networks shows that the scale-free networks in general yield higher deviations in terms of the electrical properties and the volumetric energy density during the delithiation process. This is due to the special structure of the scale-free networks. They tend to create networks with overall low connectivity and thus the number of conductive paths going from the current collector to the separator is low. In poorly connected scale-free networks, bottlenecks can occur, which have a drastic impact on the performance. Random networks are shown to be much more robust against deviations of the network structure due to overall good connectivity, which compensates single defects in the structure.

In this study, the electrical conductivity was represented by electrical networks with lumped properties of the connections. However, the CBM structure is much more complex and the properties depend on materials, tortuosity and cross-sectional areas of the connections, all of which might influence the degradation behavior. Further, the active material can contribute to the conductivity. Therefore, a complete loss of all reaction surfaces might not occur in the battery, since low conductivity via the active material would remain, even for a fully degraded CBM. Future work should address the micro-scale structure connection within a CBM in more detail, which requires advanced experimental characterization and novel data analysis methods.

Most significant differences are observed for degradation of the network structures. Comparing the degradation due to random edge removal, it can be seen that random networks are favorable because they are more robust against isolation of active material. The scale-free network starts to decompose and isolate active material right from the start, while the random network mainly degrade due to thinning of the network and a consequent reduction of the electrical conductivity. To conclude, this work analyzes different artificial network structures and evaluates them in terms of different electrical and electrochemical aspects. The chapter provides mechanistic understanding and suggestions on how the electrical network should be designed to achieve optimal performance of a lithium-ion battery. Based on this study, it can be concluded that the electrical bulk conductivity of the electrode is not solely sufficient to rate the quality of the network. The results show that a high and consistent conductivity is an indicator for a good network, but the connectivity of the reaction sites can not be analyzed in depth based on this quantity. Therefore the authors emphasize that additional structural properties such as connectivity need to be taken into account to evaluate the quality of the CBM. The presented model enables a knowledge-based design of the electrical network within the electrode and can be used to identify CBMs that have

beneficial structural properties. The results further suggest that robust and high quality structures can be achieved also with lower levels of deagglomeration or lower content of CB by creating favorable network structures.

These aspects should be addressed in future studies because the reduced content of inactive material would increase the pore space and thus ionic conductivity, which enables enhanced rate capability of the lithium-ion battery. Future studies should focus on coupling the model approach with a real 3D reconstructed electrode to gain further insights into the conductive paths and identification of geometrical aspects and materials. Here, the impact of carbon nanotubes (CNT) is of interest as they are known to change the percolation. Furthermore, mixing carbon black and (CNT) might result in hybrid networks combining effects of the random and scale-free networks due to the tube-like structure of CNT.

7 Conclusion

This chapter summarizes the thesis and provides the key results. Subsequently, open questions and required future work is discussed to provide a perspective.

7.1 Summary

The scope of the dissertation is on studying and quantifying the impact of uncertainties in electrode structure on deviations in electrochemical performance. Based on the generated insights, robust electrode microstructures are identified. Structural deviations are studied from two different perspectives. First, the structural properties vary between the electrodes. The single electrode sheet is characterized by a single homogeneous set of structural parameters. That is defined as cell-to-cell deviations. Secondly, the electrode microstructure is not considered homogeneous. Local structural features, e.g., the porosity, vary within the microstructure. That affects the electrochemical performance and results in uncertainties. In this thesis, modeling approaches are established and applied to tackle both types of deviations. By describing and evaluating physical processes, the modeling approaches aim to understand how changing the electrode structure can contribute to an optimal and robust battery cell.

In the first part of the thesis, the focus was on cell-to-cell deviations caused by the production process. Therefore, a coupled model approach was introduced consisting of a process chain model and an electrochemical battery model. The process chain model consists of linked models representing the individual production steps. That enables considering correlations between process and structural parameters. In the physicochemical battery model, the performance of the produced batteries is estimated by considering the impact of the electrode structure on the physical processes. The coupled model approach enables a holistic consideration of correlations between process parameters, structural parameters, and electrochemical performance. The digitalization platform thus forms the foundation for model-based studying of the propagation of uncertainties along with the different types of relevant parameters.

Subsequently, the coupled model approach was applied to study the propagation of uncertainties in the production process. In the process chain model, the coating, drying, and calendaring were considered. The electrode was defined based on structural, material, and process-related input parameters. The operation of battery cells incorporating these electrodes was represented using

a p2D battery model. Studying the impact of uncertainties originating from the production steps was done by inducing deviations to the input parameters of the process models. Four different scenarios were analyzed, differing mainly in the process where uncertainties are induced. For the cells studied, it was identified that deviations in the coating process have the highest impact on the electrochemical performance. Tight tolerances for coating thickness and mass loading are mandatory to produce batteries with consistent volumetric energy density. Analyzing the uncertainty propagation in the process chain revealed that deviations in porosity are reduced by the calendaring. To summarize, the case study showed that the coupled model approach allows investigation of how uncertainties propagate and affect electrochemical performance. Relevant processes and process parameters are identified, and the structural parameters are studied along the process chain. That allows using the coupled model approach for further investigation and identification of optimization.

Consequently, robust optimization was the focus in the last chapter of the first part. It completes the study of cell-to-cell deviations after establishing the general model approach and applying it in a case study. Here, the digitalization platform is applied for identifying cathode designs while considering uncertainties. Thereby, the deviation of the electrochemical performance and the scrap rate is reduced. Cathodes with varying mass loadings and coating densities were analyzed at different current densities. The implemented half-cell model was able to identify performance limitations due to insufficient mass transport in the liquid electrolyte. Based on those initial calculations, optimizations were conducted for identifying cathode structures providing a desired area-related discharge capacity and high volumetric energy densities at a defined current density. Therefore, a deterministic optimization was compared to robust optimization. It was shown that considering the effects of uncertainties in the design process can be beneficial for identifying robust electrode structures in terms of performance. The electrochemical model enables studying the impact of the different physical processes (e.g. diffusion, and reaction kinetics) and allows studying the impact of these on the electrochemical performance. Hence, cathode structures are identified that are more beneficial due to non-limiting transport processes. The objective function implemented in the robust design optimization can identify a trade-off between improving the volumetric energy density and reducing performance deviations and scrap rate. Reducing performance deviations and scrap rate leads to improved cost-efficiency and sustainability in lithium-ion battery production.

In the first part of the thesis, the electrode microstructure was considered homogeneous. In the second part of the thesis, the focus was on the impact of a heterogeneous electrode microstructure. These intrinsic deviations will result in uncertainty in performance and degradation. That is shown exemplary with a modeling approach for analyzing the structure of the carbon black-binder matrix implemented. The inactive component and its impact on the electrical charge transport is often neglected or only studied by considering the effect on ionic transport in the

electrolyte. However, the CBM is crucial for providing the desired electrons to the charge transfer reaction. A hybrid model approach was implemented, coupling a homogeneous electrochemical battery model with an electrical network model. The latter one describes electron transport depending on the topology of a complex electrical network. That is established to represent the CBM in the electrode microstructure. Three different network structures were analyzed, defined as homogeneous, random, and scale-free. Analyzing the initial electrical and electrochemical performance properties revealed that scale-free networks yield high deviations. Those networks tend to create overall low connectivity, with a reduced number of conductive paths in the electrode. Bottlenecks occur that have a critical impact on the performance. Due to increased connectivity, the random network is much more robust in terms of performance. The results indicate that solely rating the established electrical network by the electrical conductivity is not sufficient. That is supported by evaluating the degradation of the networks by random edge removal. Random networks are favorable because they are more robust against the isolation of the active material. The decomposition of the scale-free networks starts early due to the low connectivity. Hence, the active material in the electrode is isolated right from the start. In the case of the random network, the connectivity is first thinned before the reaction sites start to isolate. Due to the implemented modeling approach, it is possible to identify beneficial network structures for the CBM. In the electrode microstructure, electrical networks with features of scale-free networks should be avoided and random networks should be established.

The estimated results indicate that various uncertainties have to be taken into account during the battery design process. For this purpose, different modeling approaches were established and implemented, allowing the influence of deviations and uncertainties to be studied. The main focus of this work is on establishing more robust electrode structures. In the first part, it was shown that considering deviations occurring in the production process leads to the identification of robust electrode designs with reduced uncertainties in performance. A detailed understanding of the interrelationships also leads to adjustments in production to prevent scrap before it occurs. That avoids trial-and-error and establishes knowledge-driven approaches. In the second part, it was shown that the inhomogeneous electrode structure results in deviations in performance. These can be significant and should not be neglected in the production process. The consideration of microstructures concerning their robustness in performance is important to establish robust structures. The focus here is not solely on performance but also degradation and aging. In conclusion, the work shows that it is possible and important to optimize the structure of the electrode while considering uncertainties. It helps to establish suitable and robust operating points and structures through targeted model development.

7.2 Future challenges

The theoretical approach of this work motivates future work mostly related to further model extensions, improvements, and the experimental validation of the applied approaches.

The introduced and applied coupled model approach can describe correlations between the process, structure, and performance in the production of lithium-ion batteries. The digitalization platform was used to study the propagation of uncertainties. That enabled robust design optimization considering these uncertainties. However, the coupled model approach requires a certain level of predictability. Achieving that in the process chain model requires detailed process models describing the correlations between the process parameters and the structural parameters. These bottom-up approaches were briefly introduced and need to be implemented in the process chain model and replace the currently used analytical models. Those models are based on physical processes, and hence improved predictability is provided. That is of interest when the impact of changing input parameters, e.g., structural, material, or process parameters, is studied. In addition, the amount of considered structural parameters increases, extending the digitalization platform. Increasing the complexity of the process chain model would automatically result in an increasing level of detail for the electrochemical battery cell model. The additional structural parameters estimated in the process chain model need to be considered in the battery cell model to map their impact on the electrochemical performance. Hence, increasing the predictability of the battery cell model is of interest in the future. For example, the particle size distribution of the electrodes could be implemented in the battery model. That would result in improved prediction of the kinetic processes particularly at the strongly dynamic operation of the battery. Additionally, the process models could be replaced by data-driven models. If sufficient data can be extracted from a real production environment, then data-driven models can be used to represent correlations that are not yet covered by physical relationships.

The next point to be addressed in the future is the validation of the coupled model approach. That applies to the process chain model and the battery cell model. In the process chain model, the single process models must be parametrized and validated. Additionally, the coupled process chain needs to be validated to ensure reliability in the holistic representation. That is possible if a stable production environment is accessible and the desired data is provided. Extending the battery cell model would also result in further parametrization and validation. Consequently, the currently applied measurement and parametrization routines need to be improved.

In terms of the electrical network model, validation is also the key aspect. The results gained by the theoretical consideration indicate that it is of interest to study the structure of the CBM in detail. First of all, it is of interest to analyze and visualize the CBM in conventional electrodes to analyze the structural features and compare them to the results gained in this work. Additionally, it would be of interest to adapt and establish different electrical network structures in an electrode and analyze the impact on uncertainties in performance and degradation behavior.

Bibliography

- [1] IEA(2019), “Global Energy & CO₂ Status Report 2019,” *IEA*, 2019.
- [2] P. Kurzweil and O. K. Dietlmeier, *Elektrochemische Speicher*. Springer Fachmedien Wiesbaden, 2015.
- [3] M. Yoshio, R. J. Brodd, and A. Kozawa, *Lithium-Ion Batteries*. Springer New York, 2009.
- [4] A. Masias, J. Marcicki, and W. A. Paxton, “Opportunities and Challenges of Lithium Ion Batteries in Automotive Applications,” *ACS Energy Letters*, vol. 6, no. 2, pp. 621–630, 2021.
- [5] N. Nitta, F. Wu, J. T. Lee, and G. Yushin, “Li-ion battery materials: Present and future,” *Materials Today*, vol. 18, no. 5, pp. 252–264, 2015.
- [6] X. Lu, A. Bertei, D. P. Finegan, C. Tan, S. R. Daemi, J. S. Weaving, K. B. O’Regan, T. M. Heenan, G. Hinds, E. Kendrick, D. J. Brett, and P. R. Shearing, “3D microstructure design of lithium-ion battery electrodes assisted by X-ray nano-computed tomography and modelling,” *Nature Communications*, vol. 11, no. 1, pp. 1–13, 2020.
- [7] R. Wagner, N. Preschitschek, S. Passerini, J. Leker, and M. Winter, “Current research trends and prospects among the various materials and designs used in lithium-based batteries,” *Journal of Applied Electrochemistry*, vol. 43, no. 5, pp. 481–496, 2013.
- [8] A. Thielmann, A. Sauer, and M. Wietschel, *Gesamt-Roadmap Lithium-Ionen-Batterien 2030*. Fraunhofer ISI, 2019.
- [9] A. Kwade, W. Haselrieder, R. Leithoff, A. Modlinger, F. Dietrich, and K. Droeder, “Current status and challenges for automotive battery production technologies,” *Nature Energy*, vol. 3, no. 4, pp. 290–300, 2018.
- [10] S. Paul, C. Diegelmann, H. Kabza, and W. Tillmetz, “Analysis of ageing inhomogeneities in lithium-ion battery systems,” *Journal of Power Sources*, vol. 239, pp. 642–650, 2013.

- [11] R. Gogoana, M. B. Pinson, M. Z. Bazant, and S. E. Sarma, "Internal resistance matching for parallel-connected lithium-ion cells and impacts on battery pack cycle life," *Journal of Power Sources*, vol. 252, pp. 8–13, 2014.
- [12] F. An, L. Chen, J. Huang, J. Zhang, and P. Li, "Rate dependence of cell-to-cell variations of lithium-ion cells," *Scientific Reports*, vol. 6, pp. 4–10, 2016.
- [13] S. Santhanagopalan and R. E. White, "Quantifying Cell-to-Cell Variations in Lithium Ion Batteries," *International Journal of Electrochemistry*, vol. 2012, pp. 1–10, 2012.
- [14] D. Beck, P. Dechent, M. Junker, D. U. Sauer, and M. Dubarry, "Inhomogeneities and Cell-to-Cell Variations in Lithium-Ion Batteries, a Review," *Energies*, vol. 14, no. 11, p. 3276, 2021.
- [15] V. Laue, O. Schmidt, H. Dreger, X. Xie, F. Röder, R. Schenkendorf, A. Kwade, and U. Krewer, "Model-based uncertainty quantification for the product properties of lithium-ion batteries," *Energy Technology*, vol. 8, no. 2, p. 1900201, 2020.
- [16] M. Hadigol, K. Maute, and A. Doostan, "On uncertainty quantification of lithium-ion batteries: Application to an LiC₆/LiCoO₂cell," *Journal of Power Sources*, vol. 300, pp. 507–524, 2015.
- [17] R. Korthauer, *Lithium-Ion Batteries: Basics and Applications*. Springer Berlin Heidelberg, 2018.
- [18] H. Lee, M. Yanilmaz, O. Toprakci, K. Fu, and X. Zhang, "A review of recent developments in membrane separators for rechargeable lithium-ion batteries," *Energy & Environmental Science*, vol. 7, no. 12, pp. 3857–3886, 2014.
- [19] A. M. Haregewoin, A. S. Wotango, and B.-J. Hwang, "Electrolyte additives for lithium ion battery electrodes: progress and perspectives," *Energy & Environmental Science*, vol. 9, no. 6, pp. 1955–1988, 2016.
- [20] M. Winter, J. O. Besenhard, M. E. Spahr, and P. Novák, "Insertion Electrode Materials for Rechargeable Lithium Batteries," *Advanced Materials*, vol. 10, no. 10, pp. 725–763, 1998.
- [21] M. S. Whittingham, "Lithium Batteries and Cathode Materials," *Chemical Reviews*, vol. 104, no. 10, pp. 4271–4302, 2004.
- [22] B. L. Ellis, K. T. Lee, and L. F. Nazar, "Positive Electrode Materials for Li-Ion and Li-Batteries," *Chemistry of Materials*, vol. 22, no. 3, pp. 691–714, 2010.

- [23] M. N. Obrovac and V. L. Chevrier, "Alloy Negative Electrodes for Li-Ion Batteries," *Chemical Reviews*, vol. 114, no. 23, pp. 11 444–11 502, 2014.
- [24] J. Newman and K. E. Thomas-Alyea, *Electrochemical systems*. John Wiley & Sons, 2012.
- [25] J. Newman and W. Tiedemann, "Porous-electrode theory with battery applications," *AIChE Journal*, vol. 21, no. 1, pp. 25–41, 1975.
- [26] A. N. Mistry, K. Smith, and P. P. Mukherjee, "Secondary-Phase Stochastics in Lithium-Ion Battery Electrodes," *ACS Applied Materials & Interfaces*, vol. 10, no. 7, pp. 6317–6326, 2018.
- [27] V. Laue, F. Röder, and U. Krewer, "Joint structural and electrochemical modeling: Impact of porosity on lithium-ion battery performance," *Electrochimica Acta*, vol. 314, 2019.
- [28] F. Jiang and P. Peng, "Elucidating the Performance Limitations of Lithium-ion Batteries due to Species and Charge Transport through Five Characteristic Parameters," *Scientific Reports*, vol. 6, no. 32639, pp. 1–18, 2016.
- [29] Y.-H. Chen, C.-W. Wang, G. Liu, X.-Y. Song, V. S. Battaglia, and A. M. Sastry, "Selection of conductive additives in li-ion battery cathodes," *Journal of The Electrochemical Society*, vol. 154, no. 10, p. A978, 2007.
- [30] J. W. Long, B. Dunn, D. R. Rolison, and H. S. White, "3d architectures for batteries and electrodes," *Advanced Energy Materials*, vol. 10, no. 46, p. 2002457, 2020.
- [31] T. Danner, M. Singh, S. Hein, J. Kaiser, H. Hahn, and A. Latz, "Thick electrodes for li-ion batteries: A model based analysis," *Journal of Power Sources*, vol. 334, pp. 191–201, 2016.
- [32] H. Zheng, L. Tan, G. Liu, X. Song, and V. S. Battaglia, "Calendering effects on the physical and electrochemical properties of Li[Ni1/3Mn1/3Co1/3]O2 cathode," *Journal of Power Sources*, vol. 208, pp. 52–57, 2012.
- [33] V. Laue, N. Wolff, F. Röder, and U. Krewer, "Modeling the influence of mixing strategies on microstructural properties of all-solid-state electrodes," *Energy Technology*, vol. 8, no. 2, p. 1801049, 2020.
- [34] V. Ramadesigan, R. N. Methekar, F. Latinwo, R. D. Braatz, and V. R. Subramanian, "Optimal Porosity Distribution for Minimized Ohmic Drop across a Porous Electrode," *Journal of The Electrochemical Society*, vol. 157, no. 12, p. A1328, 2010.

- [35] W. Haselrieder, S. Ivanov, H. Tran, S. Theil, L. Froböse, B. Westphal, M. Wohlfahrt-Mehrens, and A. Kwade, "Influence of formulation method and related processes on structural, electrical and electrochemical properties of LMS/NCA-blend electrodes," *Progress in Solid State Chemistry*, vol. 42, no. 4, pp. 157–174, 2014.
- [36] L. S. Kremer, A. Hoffmann, T. Danner, S. Hein, B. Prifling, D. Westhoff, C. Dreer, A. Latz, V. Schmidt, and M. Wohlfahrt-Mehrens, "Manufacturing process for improved ultra-thick cathodes in high-energy lithium-ion batteries," *Energy Technology*, vol. 8, no. 2, p. 1900167, 2020.
- [37] J. B. Habedank, L. Kraft, A. Rheinfeld, C. Krezdorn, A. Jossen, and M. F. Zaeh, "Increasing the Discharge Rate Capability of Lithium-Ion Cells with Laser-Structured Graphite Anodes: Modeling and Simulation," *Journal of The Electrochemical Society*, vol. 165, no. 7, pp. A1563–A1573, 2018.
- [38] D. Witt, D. Wilde, F. Baakes, F. Belkhir, F. Röder, and U. Krewer, "Myth and reality of a universal lithium-ion battery electrode design optimum: A perspective and case study," *Energy Technology*, vol. 9, no. 6, p. 2000989, 2021.
- [39] M. Broussely, S. Herreyre, P. Biensan, P. Kasztejna, K. Nechev, and R. Staniewicz, "Aging mechanism in li ion cells and calendar life predictions," *Journal of Power Sources*, vol. 97-98, pp. 13–21, 2001.
- [40] J. Vetter, P. Novák, M. Wagner, C. Veit, K.-C. Möller, J. Besenhard, M. Winter, M. Wohlfahrt-Mehrens, C. Vogler, and A. Hammouche, "Ageing mechanisms in lithium-ion batteries," *Journal of Power Sources*, vol. 147, no. 1-2, pp. 269–281, 2005.
- [41] A. Barré, B. Deguilhem, S. Grolleau, M. Gérard, F. Suard, and D. Riu, "A review on lithium-ion battery ageing mechanisms and estimations for automotive applications," *Journal of Power Sources*, vol. 241, pp. 680–689, 2013.
- [42] C. R. Birkl, M. R. Roberts, E. McTurk, P. G. Bruce, and D. A. Howey, "Degradation diagnostics for lithium ion cells," *Journal of Power Sources*, vol. 341, pp. 373–386, 2017.
- [43] X. He, D. Bresser, S. Passerini, F. Baakes, U. Krewer, J. Lopez, C. T. Mallia, Y. Shao-Horn, I. Cekic-Laskovic, S. Wiemers-Meyer, F. A. Soto, V. Ponce, J. M. Seminario, P. B. Balbuena, H. Jia, W. Xu, Y. Xu, C. Wang, B. Horstmann, R. Amine, C.-C. Su, J. Shi, K. Amine, M. Winter, A. Latz, and R. Kostecki, "The passivity of lithium electrodes in liquid electrolytes for secondary batteries," *Nature Reviews Materials*, vol. 6, pp. 1036–1052, 2021.
- [44] T. Waldmann, B.-I. Hogg, and M. Wohlfahrt-Mehrens, "Li plating as unwanted side reaction in commercial Li-ion cells – A review," *Journal of Power Sources*, vol. 384, no. February, pp. 107–124, 2018.

- [45] L. Y. Beaulieu, T. D. Hatchard, A. Bonakdarpour, M. D. Fleischauer, and J. R. Dahn, "Reaction of Li with Alloy Thin Films Studied by In Situ AFM," *Journal of The Electrochemical Society*, vol. 150, no. 11, p. A1457, 2003.
- [46] K. Edström, T. Gustafsson, and J. Thomas, "The cathode–electrolyte interface in the Li-ion battery," *Electrochimica Acta*, vol. 50, no. 2-3, pp. 397–403, 2004.
- [47] Y. Liu, R. Zhang, J. Wang, and Y. Wang, "Current and future lithium-ion battery manufacturing," *iScience*, vol. 24, no. 4, p. 102332, 2021.
- [48] J. K. Mayer, L. Almar, E. Asylbekov, W. Haselrieder, A. Kwade, A. Weber, and H. Nirschl, "Influence of the carbon black dispersing process on the microstructure and performance of li-ion battery cathodes," *Energy Technology*, vol. 8, no. 2, p. 1900161, 2020.
- [49] R. Dominko, M. Gaberšček, J. Drogenik, M. Bele, and J. Jamnik, "Influence of Carbon Black Distribution on Performance of Oxide Cathodes for Li-Ion Batteries," *Electrochimica Acta*, vol. 48, no. 24, pp. 3709–3716, 2003.
- [50] F. Huttner, W. Haselrieder, and A. Kwade, "The influence of different post-drying procedures on remaining water content and physical and electrochemical properties of lithium-ion batteries," *Energy Technology*, vol. 8, no. 2, p. 1900245, 2020.
- [51] M. Haarmann, W. Haselrieder, and A. Kwade, "Extrusion-Based Processing of Cathodes: Influence of Solid Content on Suspension and Electrode Properties," *Energy Technology*, vol. 8, no. 2, p. 1801169, 2020.
- [52] G. Schällicke, I. Landwehr, A. Dinter, K.-H. Pettinger, W. Haselrieder, and A. Kwade, "Solvent-Free Manufacturing of Electrodes for Lithium-Ion Batteries via Electrostatic Coating," *Energy Technology*, vol. 8, no. 2, p. 1900309, 2020.
- [53] B. Ludwig, Z. Zheng, W. Shou, Y. Wang, and H. Pan, "Solvent-Free Manufacturing of Electrodes for Lithium-ion Batteries," *Scientific Reports*, vol. 6, p. 23150, 2016.
- [54] S. J. An, J. Li, Z. Du, C. Daniel, and D. L. Wood, "Fast formation cycling for lithium ion batteries," *Journal of Power Sources*, vol. 342, pp. 846–852, 2017.
- [55] M. B. Pinson and M. Z. Bazant, "Theory of SEI formation in rechargeable batteries: Capacity fade, accelerated aging and lifetime prediction," *Journal of The Electrochemical Society*, vol. 160, no. 2, pp. A243–A250, dec 2012.
- [56] F. Röder, S. Sonntag, D. Schröder, and U. Krewer, "Simulating the impact of particle size distribution on the performance of graphite electrodes in lithium-ion batteries," *Energy Technology*, vol. 4, no. 12, pp. 1588–1597, 2016.

- [57] L. Gaines, Q. Dai, J. T. Vaughey, and S. Gillard, "Direct recycling r&d at the recell center," *Recycling*, vol. 6, no. 2, 2021.
- [58] S. Ahmed, P. A. Nelson, and D. W. Dees, "Study of a dry room in a battery manufacturing plant using a process model," *Journal of Power Sources*, vol. 326, pp. 490–497, 2016. [Online]. Available: <https://www.sciencedirect.com/science/article/pii/S0378775316308199>
- [59] L. Hoffmann, J.-K. Grathwol, W. Haselrieder, R. Leithoff, T. Jansen, K. Dilger, K. Dröder, A. Kwade, and M. Kurrat, "Capacity distribution of large lithium-ion battery pouch cells in context with pilot production processes," *Energy Technology*, vol. 8, no. 2, p. 1900196, 2020.
- [60] F. Font, B. Protas, G. Richardson, and J. Foster, "Binder migration during drying of lithium-ion battery electrodes: Modelling and comparison to experiment," *Journal of Power Sources*, vol. 393, pp. 177–185, 2018. [Online]. Available: <https://www.sciencedirect.com/science/article/pii/S0378775318304464>
- [61] R. Leithoff, A. Fröhlich, and K. Dröder, "Investigation of the influence of deposition accuracy of electrodes on the electrochemical properties of lithium-ion batteries," *Energy Technology*, vol. 8, no. 2, p. 1900129, 2020. [Online]. Available: <https://onlinelibrary.wiley.com/doi/abs/10.1002/ente.201900129>
- [62] V. Ramadesigan, P. W. C. Northrop, S. De, S. Santhanagopalan, R. D. Braatz, and V. R. Subramanian, "Modeling and simulation of lithium-ion batteries from a systems engineering perspective," *Journal of The Electrochemical Society*, vol. 159, no. 3, pp. R31–R45, 2012.
- [63] B. Yann Liaw, G. Nagasubramanian, R. G. Jungst, and D. H. Doughy, "Modeling of lithium ion cells—a simple equivalent-circuit model approach," *Solid State Ionics*, vol. 175, no. 1, pp. 835–839, 2004.
- [64] R. Drees, F. Lienesch, and M. Kurrat, "Fast charging lithium-ion battery formation based on simulations with an electrode equivalent circuit model," *Journal of Energy Storage*, vol. 36, p. 102345, 2021.
- [65] M. Doyle, "Modeling of Galvanostatic Charge and Discharge of the Lithium/Polymer/Insertion Cell," *Journal of The Electrochemical Society*, vol. 140, no. 6, p. 1526, 1993.
- [66] T. F. Fuller, M. Doyle, and J. Newman, "Simulation and Optimization of the Dual Lithium Ion Insertion Cell," *Journal of The Electrochemical Society*, vol. 141, no. 1, pp. 1–10, 1994.

-
- [67] N. Legrand, S. Raël, B. Knosp, M. Hinaje, P. Desprez, and F. Lopicque, “Including Double-Layer Capacitance in Lithium-Ion Battery Mathematical Models,” *Journal of Power Sources*, vol. 251, pp. 370–378, 2014.
- [68] F. Röder, R. D. Braatz, and U. Krewer, “Multi-scale simulation of heterogeneous surface film growth mechanisms in lithium-ion batteries,” *Journal of The Electrochemical Society*, vol. 164, no. 11, pp. E3335–E3344, 2017.
- [69] A. Latz and J. Zausch, “Thermodynamic consistent transport theory of Li-ion batteries,” *Journal of Power Sources*, vol. 196, no. 6, pp. 3296–3302, 2011.
- [70] G. B. Less, J. H. Seo, S. Han, A. M. Sastry, J. Zausch, A. Latz, S. Schmidt, C. Wieser, D. Kehrwald, and S. Fell, “Micro-Scale Modeling of Li-Ion Batteries: Parameterization and Validation,” *Journal of The Electrochemical Society*, vol. 159, no. 6, pp. A697–A704, 2012.
- [71] N. Lin, F. Röder, and U. Krewer, “Multiphysics Modeling for Detailed Analysis of Multi-Layer Lithium-Ion Pouch Cells,” *Energies*, vol. 11, no. 11, p. 2998, 2018.
- [72] F. Röder, V. Laue, and U. Krewer, “Model Based Multiscale Analysis of Film Formation in Lithium-Ion Batteries,” *Batteries & Supercaps*, vol. 2, no. 3, pp. 248–265, 2019.
- [73] O. Schmidt and F. Röder, “Conductive Networks and Their Impact on Uncertainty, Degradation, and Failure of Lithium-Ion Battery Electrodes,” *ACS Applied Energy Materials*, vol. 4, no. 5, pp. 4845–4860, 2021.
- [74] A. M. Colclasure and R. J. Kee, “Thermodynamically Consistent Modeling of Elementary Electrochemistry in Lithium-Ion Batteries,” *Electrochimica Acta*, vol. 55, no. 28, pp. 8960–8973, 2010.
- [75] X. Xie, “Sensitivity analysis and robust design of pharmaceutical manufacturing processes,” Ph.D. dissertation, 2020.
- [76] V. N. Emenike, X. Xie, R. Schenkendorf, A. C. Spiess, and U. Krewer, “Robust dynamic optimization of enzyme-catalyzed carboligation: A point estimate-based back-off approach,” *Computers & Chemical Engineering*, vol. 121, pp. 232–247, 2019.
- [77] X. Xie and R. Schenkendorf, “Robust optimization of a pharmaceutical freeze-drying process under non-gaussian parameter uncertainties,” *Chemical Engineering Science*, vol. 207, pp. 805–819, 2019.
- [78] —, “Robust process design in pharmaceutical manufacturing under batch-to-batch variation,” *Processes*, vol. 7, no. 8, 2019.

- [79] N. Lin, X. Xie, R. Schenkendorf, and U. Krewer, "Efficient Global Sensitivity Analysis of 3D Multiphysics Model for Li-Ion Batteries," *Journal of The Electrochemical Society*, vol. 165, no. 7, pp. A1169–A1183, 2018.
- [80] B. Sudret, "Global sensitivity analysis using polynomial chaos expansions," *Reliability Engineering & System Safety*, vol. 93, no. 7, pp. 964–979, 2008.
- [81] S. Marelli and B. Sudret, *UQLab: A Framework for Uncertainty Quantification in Matlab*, pp. 2554–2563.
- [82] L. N. Marelli, S. and B. Sudret, "UQLab user manual – Polynomial chaos expansions," Chair of Risk, Safety and Uncertainty Quantification, ETH Zurich, Switzerland, Tech. Rep., 2021.
- [83] S. Marelli, C. Lamas, K. Konakli, C. Mylonas, P. Wiederkehr, and B. Sudret, "UQLab user manual – Sensitivity analysis," Chair of Risk, Safety and Uncertainty Quantification, ETH Zurich, Switzerland, Tech. Rep., 2021.
- [84] N. Wiener, "The Homogeneous Chaos," *American Journal of Mathematics*, vol. 60, no. 4, p. 897, 1938.
- [85] G. Blatman and B. Sudret, "Adaptive sparse polynomial chaos expansion based on least angle regression," *Journal of Computational Physics*, vol. 230, no. 6, pp. 2345–2367, 2011.
- [86] M. Thomitzek, O. Schmidt, F. Röder, U. Krewer, C. Herrmann, and S. Thiede, "Simulating Process-Product Interdependencies in Battery Production Systems," *Procedia CIRP*, vol. 72, pp. 346–351, 2018.
- [87] M. Thomitzek, O. Schmidt, G. Ventura Silva, H. Karaki, M. Lippke, U. Krewer, D. Schröder, A. Kwade, and C. Herrmann, "Digitalization Platform for Mechanistic Modeling of Battery Cell Production," *Sustainability*, vol. 14, no. 3, pp. 1–22, 2022.
- [88] H. Bockholt, M. Indrikova, A. Netz, F. Golks, and A. Kwade, "The interaction of consecutive process steps in the manufacturing of lithium-ion battery electrodes with regard to structural and electrochemical properties," *Journal of Power Sources*, vol. 325, pp. 140–151, 2016.
- [89] M. Schmitt, M. Baunach, L. Wengeler, K. Peters, P. Junges, P. Scharfer, and W. Schabel, "Slot-die processing of lithium-ion battery electrodes - Coating window characterization," *Chemical Engineering and Processing: Process Intensification*, vol. 68, pp. 32–37, 2013.

- [90] A. Davoodabadi, J. Li, H. Zhou, D. L. Wood, T. J. Singler, and C. Jin, "Effect of calendaring and temperature on electrolyte wetting in lithium-ion battery electrodes," *Journal of Energy Storage*, vol. 26, p. 101034, 2019.
- [91] A. Shodiev, E. Primo, O. Arcelus, M. Chouchane, M. Osenberg, A. Hilger, I. Manke, J. Li, and A. A. Franco, "Insight on electrolyte infiltration of lithium ion battery electrodes by means of a new three-dimensional-resolved lattice boltzmann model," *Energy Storage Materials*, vol. 38, pp. 80–92, 2021.
- [92] A. C. Ngandjong, A. Rucci, M. Maiza, G. Shukla, J. Vazquez-Arenas, and A. A. Franco, "Multiscale Simulation Platform Linking Lithium Ion Battery Electrode Fabrication Process with Performance at the Cell Level," *The Journal of Physical Chemistry Letters*, vol. 8, no. 23, pp. 5966–5972, 2017.
- [93] M. Chouchane, A. Rucci, T. Lombardo, A. C. Ngandjong, and A. A. Franco, "Lithium ion battery electrodes predicted from manufacturing simulations: Assessing the impact of the carbon-binder spatial location on the electrochemical performance," *Journal of Power Sources*, vol. 444, p. 227285, 2019.
- [94] M. Schönemann, *Multiscale Simulation Approach for Battery Production Systems*. Springer Cham, 2017.
- [95] J. Kumberg, M. Müller, R. Diehm, S. Spiegel, C. Wachsmann, W. Bauer, P. Scharfer, and W. Schabel, "Drying of Lithium-Ion Battery Anodes for Use in High-Energy Cells: Influence of Electrode Thickness on Drying Time, Adhesion, and Crack Formation," *Energy Technology*, vol. 7, no. 11, p. 1900722, 2019.
- [96] C. Meyer, H. Bockholt, W. Haselrieder, and A. Kwade, "Characterization of the calendaring process for compaction of electrodes for lithium-ion batteries," *Journal of Materials Processing Tech.*, vol. 249, pp. 172–178, 2017.
- [97] C. Meyer, M. Kosfeld, W. Haselrieder, and A. Kwade, "Process modeling of the electrode calendaring of lithium-ion batteries regarding variation of cathode active materials and mass loadings," *Journal of Energy Storage*, vol. 18, pp. 371–379, 2018.
- [98] C. Sangrós Giménez, C. Schilde, L. Froböse, S. Ivanov, and A. Kwade, "Mechanical, electrical, and ionic behavior of lithium-ion battery electrodes via discrete element method simulations," *Energy Technology*, vol. 8, no. 2, p. 1900180, 2020.
- [99] D. Schreiner, A. Klinger, and G. Reinhart, "Modeling of the calendaring process for lithium-ion batteries with DEM simulation," *Procedia CIRP*, vol. 93, pp. 149–155, 2020.

- [100] E. Asylbekov, R. Trunk, M. J. Krause, and H. Nirschl, "Microscale Discrete Element Method Simulation of the Carbon Black Aggregate Fracture Behavior in a Simple Shear Flow," *Energy Technology*, vol. 9, no. 6, p. 2000850, 2021.
- [101] O. Schmidt, M. Thomitzek, F. Röder, S. Thiede, C. Herrmann, and U. Krewer, "Modeling the impact of manufacturing uncertainties on lithium-ion batteries," *Journal of The Electrochemical Society*, vol. 167, no. 6, p. 060501, 2020.
- [102] S. Jaiser, J. Kumberg, J. Klaver, J. L. Urai, W. Schabel, J. Schmatz, and P. Scharfer, "Microstructure formation of lithium-ion battery electrodes during drying – An ex-situ study using cryogenic broad ion beam slope-cutting and scanning electron microscopy (Cryo-BIB-SEM)," *Journal of Power Sources*, vol. 345, pp. 97–107, 2017.
- [103] G. Lenze, F. Röder, H. Bockholt, W. Haselrieder, A. Kwade, and U. Krewer, "Simulation-Supported Analysis of Calendaring Impacts on the Performance of Lithium-Ion-Batteries," *Journal of The Electrochemical Society*, vol. 164, no. 6, pp. A1223–A1233, 2017.
- [104] J. Smekens, R. Gopalakrishnan, N. Steen, N. Omar, O. Hegazy, A. Hubin, and J. Van Mierlo, "Influence of Electrode Density on the Performance of Li-Ion Batteries: Experimental and Simulation Results," *Energies*, vol. 9, no. 2, p. 104, 2016.
- [105] B. Kenney, K. Darcovich, D. D. MacNeil, and I. J. Davidson, "Modelling the impact of variations in electrode manufacturing on lithium-ion battery modules," *Journal of Power Sources*, vol. 213, pp. 391–401, 2012.
- [106] C. Meyer, M. Weyhe, W. Haselrieder, and A. Kwade, "Heated calendaring of cathodes for lithium-ion batteries with varied carbon black and binder contents," *Energy Technology*, vol. 8, no. 2, p. 1900175, 2020.
- [107] D. A. G. Bruggeman, "Berechnung verschiedener physikalischer Konstanten von heterogenen Substanzen. III. Die elastischen Konstanten der quasiisotropen Mischkörper aus isotropen Substanzen," *Annalen der Physik*, vol. 421, no. 2, pp. 160–178, 1937.
- [108] M. Ebner and V. Wood, "Tool for Tortuosity Estimation in Lithium Ion Battery Porous Electrodes," *Journal of the Electrochemical Society*, vol. 162, no. 2, pp. A3064–A3070, 2015.
- [109] O. Schmidt and U. Krewer, "Robust design optimization of lithium-ion battery cathodes," in preparation.
- [110] V. Srinivasan and J. Newman, "Design and Optimization of a Natural Graphite/Iron Phosphate Lithium-Ion Cell," *Journal of The Electrochemical Society*, vol. 151, no. 10, p. A1530, 2004.

- [111] T. F. Fuller, M. Doyle, and J. Newman, "Simulation and Optimization of the Dual Lithium Ion Insertion Cell," *Journal of The Electrochemical Society*, vol. 141, no. 1, pp. 1–10, 1994.
- [112] H.-G. Beyer and B. Sendhoff, "Robust optimization – a comprehensive survey," *Computer Methods in Applied Mechanics and Engineering*, vol. 196, no. 33, pp. 3190–3218, 2007.
- [113] Z. Nagy and R. Braatz, "Worst-case and distributional robustness analysis of finite-time control trajectories for nonlinear distributed parameter systems," *IEEE Transactions on Control Systems Technology*, vol. 11, no. 5, pp. 694–704, 2003.
- [114] S. T. F. Mortier, P.-J. Van Bockstal, J. Corver, I. Nopens, K. V. Gernaey, and T. De Beer, "Uncertainty analysis as essential step in the establishment of the dynamic Design Space of primary drying during freeze-drying," *European Journal of Pharmaceutics and Biopharmaceutics*, vol. 103, pp. 71–83, 2016.
- [115] D. Yoo, J. Park, J. Moon, and C. Kim, "Reliability-Based Design Optimization for Reducing the Performance Failure and Maximizing the Specific Energy of Lithium-Ion Batteries Considering Manufacturing Uncertainty of Porous Electrodes," *Energies*, vol. 14, no. 19, p. 6100, 2021.
- [116] C. Heubner, M. Schneider, and A. Michaelis, "Diffusion-Limited C-Rate: A Fundamental Principle Quantifying the Intrinsic Limits of Li-Ion Batteries," *Advanced Energy Materials*, vol. 10, no. 2, 2020.
- [117] L. S. Kremer, "Process-structure-property Relationships of ultra-thick positive Electrodes for High-Energy Lithium-Ion Batteries," 2021.
- [118] L. S. Kremer, T. Danner, S. Hein, A. Hoffmann, B. Prifling, V. Schmidt, A. Latz, and M. Wohlfahrt-Mehrens, "Influence of the Electrolyte Salt Concentration on the Rate Capability of Ultra-Thick NCM 622 Electrodes," *Batteries and Supercaps*, vol. 3, no. 11, pp. 1172–1182, 2020.
- [119] M. Thomitzek, O. Schmidt, T. Abraham, F. Cerdas, F. Röder, U. Krewer, and C. Herrmann, "Model-based identification of production tolerances in battery production," *Procedia CIRP*, vol. 104, pp. 1059–1064, 2021.
- [120] X. Xie, R. Schenkendorf, and U. Krewer, "Robust Design of Chemical Processes Based on a One-Shot Sparse Polynomial Chaos Expansion Concept," in *Computer Aided Chemical Engineering*, 2017, vol. 40, pp. 613–618.

- [121] R. Dominko, M. Gaberscek, J. Drogenik, M. Bele, S. Pejovnik, and J. Jamnik, "The Role of Carbon Black Distribution in Cathodes for Li-Ion Batteries," *Journal of Power Sources*, vol. 119-121, pp. 770–773, 2003.
- [122] G. Liu, H. Zheng, A. S. Simens, A. M. Minor, X. Song, and V. S. Battaglia, "Optimization of Acetylene Black Conductive Additive and PVDF Composition for High-Power Rechargeable Lithium-Ion Cells," *Journal of The Electrochemical Society*, vol. 154, no. 12, p. A1129, 2007.
- [123] G. Liu, H. Zheng, S. Kim, Y. Deng, A. M. Minor, X. Song, and V. S. Battaglia, "Effects of Various Conductive Additive and Polymeric Binder Contents on the Performance of a Lithium-Ion Composite Cathode," *Journal of The Electrochemical Society*, vol. 155, no. 12, p. A887, 2008.
- [124] G. Liu, H. Zheng, X. Song, and V. S. Battaglia, "Particles and Polymer Binder Interaction: A Controlling Factor in Lithium-Ion Electrode Performance," *Journal of The Electrochemical Society*, vol. 159, no. 3, pp. A214–A221, 2012.
- [125] F. M. Smits, "Measurement of Sheet Resistivities with the Four-Point Probe," *Bell System Technical Journal*, vol. 37, no. 3, pp. 711–718, 1958.
- [126] W. Zhou, Y. Tang, R. Song, L. Jiang, K. Hui, and K. Hui, "Characterization of Electrical Conductivity of Porous Metal Fiber Sintered Sheet Using Four-Point Probe Method," *Materials & Design*, vol. 37, pp. 161–165, 2012.
- [127] J. E. Vogel, M. M. Forouzan, E. E. Hardy, S. T. Crawford, D. R. Wheeler, and B. A. Mazzeo, "Electrode microstructure controls localized electronic impedance in li-ion batteries," *Electrochimica Acta*, vol. 297, pp. 820 – 825, 2019.
- [128] L. Almar, J. Joos, A. Weber, and E. Ivers-Tiffée, "Microstructural feature analysis of commercial li-ion battery cathodes by focused ion beam tomography," *Journal of Power Sources*, vol. 427, pp. 1 – 14, 2019.
- [129] S. R. Daemi, C. Tan, T. Volkenandt, S. J. Cooper, A. Palacios-Padros, J. Cookson, D. J. L. Brett, and P. R. Shearing, "Visualizing the carbon binder phase of battery electrodes in three dimensions," *ACS Applied Energy Materials*, vol. 1, no. 8, pp. 3702–3710, 2018.
- [130] D. Westhoff, I. Manke, and V. Schmidt, "Generation of virtual lithium-ion battery electrode microstructures based on spatial stochastic modeling," *Computational Materials Science*, vol. 151, pp. 53–64, 2018.
- [131] O. Stenzel, D. Westhoff, I. Manke, M. Kasper, D. P. Kroese, and V. Schmidt, "Graph-based simulated annealing: a hybrid approach to stochastic modeling of complex

- microstructures,” *Modelling and Simulation in Materials Science and Engineering*, vol. 21, no. 5, p. 055004, may 2013.
- [132] S. Hein, T. Danner, D. Westhoff, B. Prifling, R. Scurtu, L. Kremer, A. Hoffmann, A. Hilger, M. Osenberg, I. Manke, M. Wohlfahrt-Mehrens, V. Schmidt, and A. Latz, “Influence of Conductive Additives and Binder on the Impedance of Lithium-Ion Battery Electrodes: Effect of Morphology,” *Journal of The Electrochemical Society*, vol. 167, no. 1, p. 013546, 2020.
- [133] A. P. Cocco, A. Nakajo, and W. K. Chiu, “Analytical transport network theory to guide the design of 3-d microstructural networks in energy materials: Part 1. flow without reactions,” *Journal of Power Sources*, vol. 372, pp. 297–311, 2017.
- [134] A. P. Cocco and W. K. Chiu, “Analytical transport network theory to guide the design of 3-d microstructural networks in energy materials: Part 2. flow with reactions,” *Journal of Power Sources*, vol. 372, pp. 312–324, 2017.
- [135] M. F. Lagadec, R. Zahn, S. Müller, and V. Wood, “Topological and Network Analysis of Lithium-Ion Battery Components: The Importance of Pore Space Connectivity for Cell Operation,” *Energy Environ. Sci.*, vol. 11, no. 11, pp. 3194–3200, 2018.
- [136] P. Barai, K. Smith, C.-F. Chen, G.-H. Kim, and P. P. Mukherjee, “Reduced order modeling of mechanical degradation induced performance decay in lithium-ion battery porous electrodes,” *Journal of The Electrochemical Society*, vol. 162, no. 9, pp. A1751–A1771, 2015.
- [137] Y. Yang, R. Xu, K. Zhang, S. Lee, L. Mu, P. Liu, C. K. Waters, S. Spence, Z. Xu, C. Wei, D. J. Kautz, Q. Yuan, Y. Dong, Y. Yu, X. Xiao, H. Lee, P. Pianetta, P. Cloetens, J. Lee, K. Zhao, F. Lin, and Y. Liu, “Quantification of Heterogeneous Degradation in Li-Ion Batteries,” *Advanced Energy Materials*, vol. 9, no. 25, p. 1900674, 2019.
- [138] A. Chauhan, E. Asylbekov, S. Kesper, and H. Nirschl, “Influence of carbon binder domain on the performance of lithium-ion batteries: Impact of size and fractal dimension,” *Electrochemical Science Advances*, vol. n/a, no. n/a, p. e2100151.
- [139] B. Bollobás, *Modern Graph Theory*. Springer New York, 1998, vol. 184.
- [140] —, *Random Graphs*. Cambridge University Press, 2001.
- [141] S. Boccaletti, V. Latora, Y. Moreno, M. Chavez, and D.-U. Hwang, “Complex networks: Structure and dynamics,” *Physics Reports*, vol. 424, no. 4, pp. 175–308, 2006.

- [142] C. Sangrós Giménez, L. Helmers, C. Schilde, A. Diener, and A. Kwade, “Modeling the Electrical Conductive Paths within All-Solid-State Battery Electrodes,” *Chemical Engineering & Technology*, vol. 43, no. 5, pp. 819–829, 2020.
- [143] J. Tranquillo, *An Introduction to Complex Systems: Making Sense of a Changing World*. Springer Cham, 2019.
- [144] S. Ahn, Y. Kim, K. J. Kim, T. H. Kim, H. Lee, and M. H. Kim, “Development of High Capacity, High Rate Lithium-Ion Batteries Utilizing Metal Fiber Conductive Additives,” *Journal of Power Sources*, vol. 81-82, pp. 896–901, 1999.
- [145] H. Bockholt, W. Haselrieder, and A. Kwade, “Intensive Dry and Wet Mixing Influencing the Structural and Electrochemical Properties of Secondary Lithium-Ion Battery Cathodes,” *ECS Transactions*, vol. 50, no. 26, pp. 25–35, 2013.
- [146] A. Nakajo, A. Cocco, M. DeGostin, A. Peracchio, B. Cassenti, M. Cantoni, J. Van herle, and W. Chiu, “Accessible triple-phase boundary length: A performance metric to account for transport pathways in heterogeneous electrochemical materials,” *Journal of Power Sources*, vol. 325, pp. 786–800, 2016.
- [147] P. Crucitti, V. Latora, and M. Marchiori, “Model for cascading failures in complex networks,” *Phys. Rev. E*, vol. 69, p. 045104, Apr 2004.
- [148] K. A. Severson, P. M. Attia, N. Jin, N. Perkins, B. Jiang, Z. Yang, M. H. Chen, M. Aykol, P. K. Herring, D. Fraggedakis, M. Z. Bazant, S. J. Harris, W. C. Chueh, and R. D. Braatz, “Data-Driven Prediction of Battery Cycle Life Before Capacity Degradation,” *Nature Energy*, vol. 4, no. 5, pp. 383–391, 2019.

List of Figures

2.1	Structure of the lithium-ion battery (LIB) with its four main components (anode, separator, cathode, and electrolyte). The most relevant physical processes are indicated. The light blue background represents the liquid electrolyte and the spheres the active material (AM) particles in the respective electrode.	6
2.4	Overview of the manufacturing processes for conventional lithium-ion batteries. The figure is reproduced and simplified based on Kwade et al. [9].	13
2.5	Ranking of different models, describing the operation of LIBs. Physical detail and computational costs are displayed for the model types. Adding physical processes and thus increasing model complexity results in improved predictability and higher computational costs.	18
3.1	Concept of the digitalization platform. It consists of three modules: (I) process chain model, (II) battery cell model, (III) analysis module. [87]	33
3.2	Exemplary process chain model implemented by coupled model containers. They are connected via structural parameters. The process chain is reduced and only exemplary models are presented for mixing, coating, and drying. [87]	34
4.1	Displayed is the basic model approach and the scenarios that were simulated for the case study.	47
4.2	Histogram of the cathode thickness (a) and mass loading (b) for the different scenarios.	50
4.3	Histogram of the cathode porosity (a) and tortuosity (b) for the different scenarios.	50
4.4	Histogram of the volumetric energy density estimated with the battery model. Included are the different scenarios and three different discharge rates 0.1 C (a), 0.3 C (b), 1 C (c).	52
4.5	Lithium concentration in the solid particles of the cathode averaged over the electrode thickness for the reference scenario at the end of discharge.	54

4.6	Simulated energy densities for three different discharge rates 0.1 C (a), 0.3 C (b), 1 C (c). Grid: model results for equidistant deviation in porosity and thickness, symbols are results of the reference case (●) and scenarios (△). The colours are consistent to the previous plots. Blue: Scenario 1, Red: Scenario 2, Yellow: Scenario 3, Purple: Scenario 4.	56
4.7	Illustration of the impact of an uncertain input parameter x with Gaussian distribution on the output y . This is shown for an arbitrary function with an optimum (a) and an arbitrary linear function (b).	57
5.1	(a) areal capacity, and (b) minimal ion concentration ever occurring in the electrolyte during the simulation, for cathodes with varying mass loading (solid lines) and coating density (dashed lines) at increasing current densities. The detailed specifications of the cathodes are listed in Table 5.1	68
5.2	Ion concentration in the electrolyte at $U_{\text{Cell}} = 3.0\text{ V}$ vs. the electrode thickness for three different current densities. The results are displayed for the cathode with a mass loading of 45 mg cm^{-2} and a coating density of 3.0 g cm^{-3}	69
5.3	(a) volumetric energy density, and (b) the volume averaged state of lithiation in the active material particles at the lower voltage boundary of 3 V for cathodes with varying mass loadings and coating densities.	70
6.1	The hybrid model is established to represent the complex structure of the CBM in the porous electrode structure. The model consists of two parts: a homogeneous electrochemical model and a network-based model for the electrical charge transport.	93
6.2	Visualization of node distribution. Increasing the level of deagglomeration yields finer CBM agglomerates. In the network this is represented by adding regular nodes, which increases the resolution of the network.	96
6.3	The degree distributions of the three generated networks structures compared to the targeted degree distributions initialized by Eqs. 6.2-6.4 for $L = 1$. The degree distributions of scale-free and random networks are averaged and standard deviation is indicated. For each distribution a resulting network structure is displayed.	101
6.4	In (a) the network conductivity versus the number of transit edges χ_{TP} is shown. In (b) the network conductivity is plotted against the transit path length λ_{TP} . The solid black line indicates the average network conductivity. Single points correspond to one of 500 different network structures for a given L and type.	103

6.5	In (a) the volumetric energy density Q of scale-free networks with $L = 1$ and $L = 3$ are plotted. The colors of the markers for $L = 1$ indicate the number of transit edges χ_{TP} in the respective network. In (b), (c), and (d) selected networks are examined in more detail. The reaction-nodes are colored concerning the normalized concentration X_{Li} at the end of delithiation. The boundary-nodes at the current collector and separator are the black nodes. The red node is the master-node at the current collector. The red edge is the identified bottleneck edge. Additionally, the percentage of AM close to the current collector P_{CC} , the transit path length λ_{TP} , and the path length to the reaction sites λ_{RN} are provided for the respective networks.	107
6.6	In (a) the volumetric energy density Q of random networks with $L = 1$ and $L = 3$ are plotted. The colors of the markers for $L = 1$ indicate the transit path length λ_{TP} in the respective network. In (b), (c), and (d) selected networks are examined in more detail. The reaction-nodes are colored concerning the normalized concentration X_{Li} at the end of delithiation. The boundary-nodes at the current collector and separator are the black nodes. Additionally, the transit path length λ_{TP} , and the path length to the reaction sites λ_{RN} are provided for the respective networks.	110
6.7	In (a) the decrease of the volumetric energy density Q with respect to the relative amount of removed edges β for random and scale-free networks at $L = 3$ is shown. In (b) the effect of the random-based edge removal on the network conductivity is displayed and in (c) the effect on the isolation of the active material due to unconnected reaction nodes is shown by the relative amount of isolated reaction nodes. Areas where the remaining volumetric energy density $q = 80\%$ and $q = 50\%$ is reached are provided for both network types. The colored area represents the deviation of the degradation and always three exemplary degradations are displayed.	112
6.8	Visual degradation of networks at a level of deagglomeration of $L = 2$ is displayed. Networks are displayed in the initial states and at $q \approx 80\%$ and $q \approx 50\%$ remaining volumetric energy density and the relative amount of removed edges β is provided for all networks. The red nodes are the reaction-nodes.	113
A.1	Comparison of the discharge measurements and the respective simulation results generated with the electrochemical model in Chapter 4.	147
A.2	Comparison of the measurements conducted with the NMC622 vs. lithium foil coin cell and the simulation results gained by the extended electrochemical model.	151

A.3 Discharge curve of the parametrized electrochemical hybrid model
with a homogeneous electrical network (solid lines) and the
measurements of the NMC 622 vs. lithium reference anode (dotted). 153

List of Tables

2.1	Governing equations for 3D+1D (P4D) electrochemical model. [67, 74]	21
4.1	Input parameters for the process chain model.	44
4.2	Battery model parameters used in the applied model. The diffusion coefficient in the electrolyte, ionic conductivity and transference number are dependent on electrolyte concentration.	46
4.3	Uncertain input parameters for the models in the process chain model for scenarios S1-S4. Mean values are given in scenario four, and deviations in scenario two to four.	48
4.4	Mean value, standard deviation and relative standard deviation of the resulting structural parameters after calendaring for the cathode thickness, porosity and tortuosity with the implemented process models. These structural parameters are used as input parameters for the battery cell simulation.	49
4.5	Mean value, standard deviation and relative standard deviation for the estimated energy density for each discharge rate.	53
4.6	Mean value, standard deviation and relative standard deviation for the estimated discharge capacity for each discharge rate.	53
5.1	Specifications of seven cathodes with varying mass loadings and the coating densities. The data for the experimental electrode are highlighted by the star.	67
5.2	Mass loadings and coating densities, and the respective performance characteristics for the initial cathode design and the values obtained by the deterministic optimization for the two different cases (I-6-3) at low current densities and (II-6-8) at high current densities.	73
5.3	Estimated mean values and standard deviations for the mass loading and coating density and the respective performance characteristics for the deterministic design and the values estimated by the robust design optimization. The values in the brackets indicate the difference to the deterministic optimal value displayed in Table 5.2.	81

6.1	Correlation between the number of nodes and the number of edges for each network structure at different levels of deagglomeration L . Values for scale-free (SF) and random networks (RND) are averaged, the standard deviation is provided.	102
6.2	Estimated average edge resistances for each network structure, homogeneous (H), random (RND), and scale-free (SF), at different levels of deagglomeration.	104
A.1	Redlich-Kister coefficients for the graphite and NMC622 OCP, implemented in the electrochemical model in Chapter 4.	148
A.3	Fitting parameters for the empiric surrogate models implemented in Chapter 5. The values are taken from Laue et al. [27].	150
A.4	Redlich-Kister coefficients for the NMC622 OCP used in Chapter 5.	151
B.1	Structural and material parameters of the experimental NMC622 cathode composition. The carbon black and conductive carbon are summed up to solely represent the conductive additives by a single value. The cathode and the respective parameters were provided by the ZSW in Ulm, Germany.	156

List of Symbols and Abbreviations

Latin letters

A	area	m^2
A_m	Redlich Kister coefficient	J kmol^{-1}
\mathcal{A}	adjacency matrix	—
a_s	active surface area per volume unit	$\text{m}^2 \text{m}^{-3}$
C	capacity	A s
C_{DL}	double layer capacitance	F m^{-2}
c	concentration in respective phase	mol m^{-3}
c_0	initial concentration	mol m^{-3}
D	diffusion coefficient of respective phase	m s^{-2}
\mathcal{D}	matrix with respective node degrees	—
d	thickness	m
d_{el}	layer thickness of the electrode	m
d_0	initial wet coating thickness	m
$d(t)$	coating thickness during drying	m
d_{dry}	coating thickness after drying	m
d_{cal}	coating thickness after calendering	m
E	number of edges e in the set \mathcal{E}	—
E^{eq}	equilibrium potential of the active material	V
\mathcal{E}	set of edges	—
e	edge	—
F	farraday constant	A s mol^{-1}
f	probability density function	—
G	graph	—
G_{33}°	standard state chemical potential of an intercalated lithium	J

$H(\mathbf{X})$	computational model dependent on random vector	—
$H_{i,j}(x_i, x_j)$	partial function from function decomposition	—
I	electrical current	A
i	current density	A m^{-2}
i_0	exchange current density	A m^{-2}
J^{tot}	absolute total current generation	A
j^{DL}	volume rate of double layer current generation	A m^{-3}
j^{Li}	volume rate of Li^+ current generation	A m^{-3}
j^{tot}	volume rate of total current generation	A m^{-3}
K	conductance matrix	S
k	degree	—
k_{ct}	rate constant for charge-transfer reaction	$\text{m}^{2.5} \text{ kmol}^{-0.5} \text{ s}^{-1}$
L	level of deagglomeration	—
L_{cell}	cell length	m
La	laplacian matrix	—
M_{solid}	mass loading of solid	kg m^{-2}
M_{solvent}	mass loading of solvent	kg m^{-2}
M_{wet}	mass loading of wet film	kg m^{-2}
m	mass	kg
m_{C}	mass of the coating without the current collector	kg
\dot{m}	drying rate	kg s^{-1}
N	number of nodes n in set \mathcal{N}	—
\mathcal{N}	set of nodes	—
n	node	—
$P(k)$	degree distribution	—
P_{CC}	percentage of active material close to current collector	—
Q	volumetric energy density	W s m^{-3}
$Q(\beta)$	volumetric energy density after β amount of edges are removed	W s m^{-3}
Q_{Initial}	initial volumetric energy density with pristine electrical network	W s m^{-3}
q_{L}	line load	N m^{-1}
q	rel. volumetric energy density during network decomposition	—
R	ideal gas constant	$\text{J mol}^{-1} \text{ K}^{-1}$

R_{Edge}	edge resistance	Ω
R_{Net}	network resistance	Ω
R_{P}	particle radius of active material	m
r	radial coordinate	m
S_i	first order Sobol' index	–
S_{ij}	higher order Sobol' index	–
S_i^{T}	total Sobol' index	–
T	temperature	K
t	time	s
t_{p}	transference number	–
t_{EoFS}	time until end of film shrinkage	s
U	voltage	V
V	volume	m^3
V_{C}	volume of the coating without the current collector	m^3
$V_{i,j}$	partial variance from variance composition	–
Var	variance function	–
w	weight fraction	–
X_{Li}	normalized concentration	–
$X_{\text{Solvent},0}$	liquid-to-solid ration of the coating	–
$X_{\text{Solvent},\text{EoFS}}$	liquid-to-solid ration at the end of film shrinkage	–
x	coordinate	m
y	coordinate	m
y_{α}	coefficients of PCE	–
z	coordinate	m
Greek letters		
α	transfer coefficient	–
β	relative amount of removed edges	–
β_{B}	Bruggeman coefficient	–
γ_{c}	compaction resistance	Nm^{-1}
ε_{e}	porosity, liquid phase volume fraction	–
ε_{s}	solid phase volume fraction	–

ε^*	effective volume fraction of the respective phase	—
$\varepsilon_{\text{crit}}$	critical volume fraction of the respective phase	—
ε_{dry}	initial porosity of the coating	—
ε_{min}	minimum porosity	—
η	overpotential	V
Θ	intercalation vacancy	—
κ	bulk conductivity of respective phase	S m^{-1}
λ_{TP}	transit path length	—
λ_{RN}	path length to reaction sites	—
μ	mean value	—
ξ_k	univariate orthonormal polynomials of PCE	—
ρ_i	density of a component i	kg m^{-3}
ρ_c	coating density	kg m^{-3}
ρ_{dry}	density of the dry coating	kg m^{-3}
ρ_{max}	maximum density	kg m^{-3}
ρ_{ph}	physical density	kg m^{-3}
ρ_{PM}	density of the particulate matter	kg m^{-3}
ρ_{slurry}	density of the slurry	kg m^{-3}
σ	standard deviation	—
τ	tortuosity	—
ϕ	potential in respective phase	V
χ_{TP}	number of transit edges	—
Ψ_α	multivariate polynomials of PCE	—
Ω	matrix with the edge conductance	S

Sub- and superscripts

AM	active material
CBM	carbon black-binder domain
cc	current collector
cell	related on battery cell
cut	cut-off
e	electrolyte phase

Edge	edge
eff	effective
el	related on electrode
H	homogeneous
in	input
max	maximum
MN	master-node
neg	negative electrode
Net	network
out	output
pos	positive electrode
RN	reaction-node
RND	random
s	solid phase
sep	separator
SF	scale-free

Abbreviations

AM	active material
ANOVA	ANalysis Of VAriance
ASSB	all solid-state battery
CB	carbon black
CBM	carbon black-binder matrix
CEI	cathode electrolyte interface
CFD	computational fluid dynamics
CT	computed tomography
DEM	discrete element method
EC	ethylene carbonate
EOL	end-of-line
ESA	electrode-separator assemble
FEM	finite element method
FIB	focused ion beam

KIT	Karlsruhe Institute of Technology
kMC	kinetic Monte-Carlo
LCO	lithium cobalt oxide
LFP	lithium iron phosphate
LIB	lithium-ion battery
LMO	lithium metal oxide
MC	Monte-Carlo
NCA	nickel-cobalt-aluminium
NMC	nickel-manganese-cobalt
NMP	N-Methyl-2-Pyrrolidone
p2D	pseudo 2-dimensional
p4D	pseudo 4-dimensional
PCE	polynomial chaos expansion
PDE	partial differential equation
PDF	probability density function
PVDF	polyvinylidene fluoride
SA	sensitivity analysis
SBR	styrene-butadiene rubber
SEI	solid electrolyte interface
SEM	scanning electron microscopy
UQ	uncertainty quantification

A Parameter and Model Validation

A.1 Data for Chapter 4

In Chapter 4, the electrochemical model was validated based on measurements conducted with an EL-CELL PAT-Cell. Graphite and NMC622 were used for the anode and cathode produced by the ZSW in Ulm, Germany. Details regarding the cell setup and structural parameters are provided in Chapter 4.3.2. Additionally, in Table A.1, the estimated Redlich-Kister coefficients for graphite (anode) and NMC622 (cathode) are listed for representing the single OCP curves of the materials. These coefficients are used in the electrochemical model.

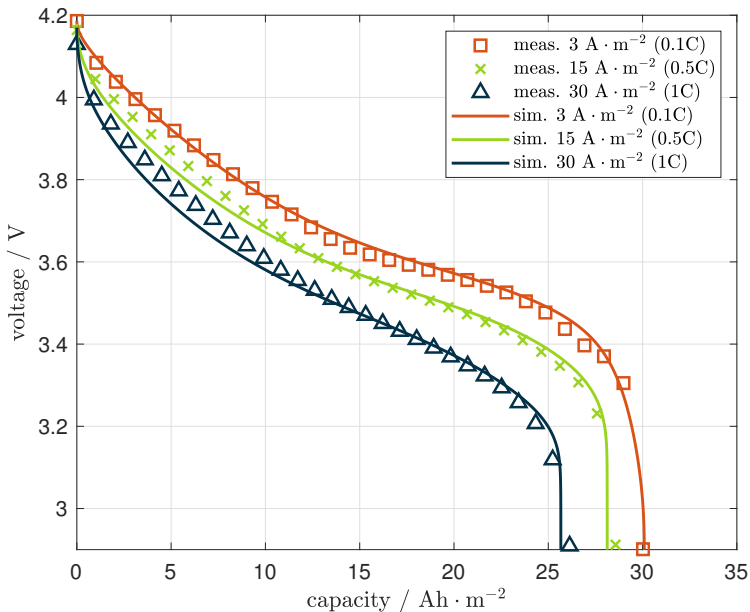


Figure A.1: Comparison of the discharge measurements and the respective simulation results generated with the electrochemical model in Chapter 4.

In Figure A.1, the measured discharge curves for three current densities are displayed by the

markers. The results of the parametrized battery model for these current densities are shown with the solid lines. A good agreement between the measured and simulated curves can be observed.

Table A.1: Redlich-Kister coefficients for the graphite and NMC622 OCP, implemented in the electrochemical model in Chapter 4.

Coefficient Jkmol^{-1}	Grpahite anode Jkmol^{-1}	NMC622 cathode Jkmol^{-1}
$\mu_{\text{Li}^+}^0$	-13623.95	-400702.35
A_0	-3573.16	-68925.68
A_1	5627.51	23521.86
A_2	-4017.09	11647.96
A_3	4545.96	-5984.28
A_4	-4118.16	-7485.09
A_5	4140.82	5098.95
A_6	-4145.24	N/A
A_7	4046.99	N/A
A_8	-4152.91	N/A
A_9	4033.88	N/A
A_{10}	-4166.47	N/A
A_{11}	4070.92	N/A
A_{12}	-4166.68	N/A
A_{13}	4062.00	N/A
A_{14}	-4150.00	N/A
A_{15}	4102.28	N/A
A_{16}	-4166.73	N/A

A.2 Data for Chapter 5

In Chapter 5, the electrochemical model was validated based on a coin cell assembled in a half-cell setup with NMC622 as the working electrode and a lithium-metal anode as the counter electrode. The electrolyte was a 1.0 M LiPF₆ in EC:EMC (3:7 in weight) with 2 wt% VC. Further information regarding the measurements is provided in Chapter 5.2.

The relevant structural data of the cathode are provided in Table A.2. The cathode was manufactured by the ZSW in Ulm, Germany. Structural features of the electrode were measured by the ZSW.

Table A.2: Structural data and battery model parameters used in the extended p2D model in Chapter 5. The diffusion coefficient in the electrolyte, and ionic conductivity are dependent on electrolyte concentration, and are taken from literature.

Parameter	Symbol	Unit	Cathode
Layer thickness ^m	d_{el}	m	48.5×10^{-6}
Porosity ^m	ϵ	-	0.3150
Solid volume fraction	ϵ_s	-	0.68
Particle size ^m	R_p	m	6.0×10^{-6}
Tortuosity ^a	τ	-	5.95
Maximum capacity solid ^a	c_{Max}	mol m ⁻³	43223
Initial capacity solid ^a	c_0	mol m ⁻³	15468
Initial capacity electrolyte ^a	c_e	mol m ⁻³	1000
Diffusion coefficient solid ^a	D_s	m ² s ⁻¹	9.32×10^{-15}
Diffusion coefficient electrolyte ^c	D_e	m ² s ⁻¹	$f(c)$ [36]
Electric bulk conductivity ^a	κ_s	S m ⁻¹	0.0313
Ionic conductivity ^c	κ_e	S m ⁻¹	$f(c)$ [36]
Transference number ^a	t_p	-	0.42
Charge transfer coefficient ^s	α	-	0.5
Reaction rate constant ^a	k	-	7.7529×10^{-10}
Double layer capacity ^s	C_{DL}	F m ⁻²	0.2

^m measured by ZSW (Department of Production Research)

^a adjusted

^s set, from ref. [67]

^c concentration dependence, see eq. in [36]

The parametrization of the electrochemical battery model was conducted as described in Chapter 4.3.2. Additionally, the empiric surrogate models implemented in the extended p2D model

need to be considered in the parametrization. The fitting parameters of the empiric surrogate model were taken from Laue et al. [27] and are provided in Table A.3.

Table A.3: Fitting parameters for the empiric surrogate models implemented in Chapter 5. The values are taken from Laue et al. [27].

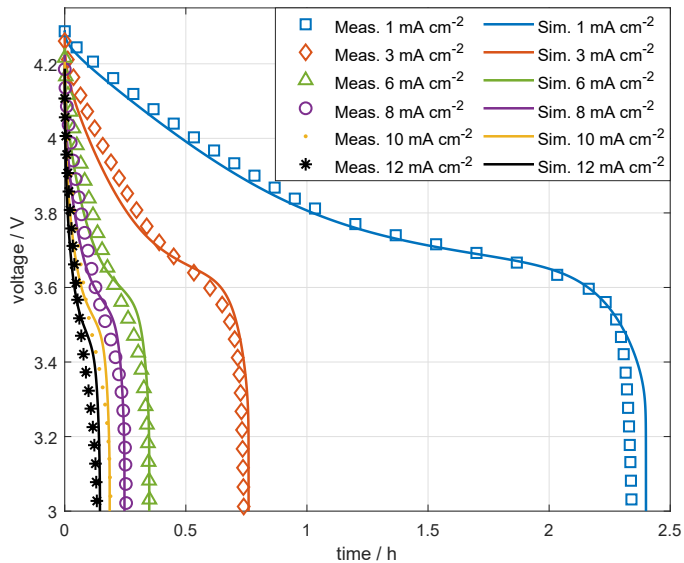
Parameter	Value
$\epsilon_{\text{crit,e}}$	0.127
β_1	1.77
ν_1	0.680
$\epsilon_{\text{crit,s}}$	0.1
β_3	0.023
β_4	2.0
ν_1	0.2
ν_2	1.5
ν_4	0.904
ν_5	1.127
ν_6	4.912

The structural, material, and kinetic parameters implemented in the extended p2D model are provided in Table A.2. Those were provided by measurements and specifications of the assembled NMC622 cathode or estimated by parametrization of the battery model. That is highlighted in the table. The open-cell potential curve is represented by the Redlich-Kister approach as described in Section 4.3. The estimated Redlich-Kister coefficients for the NMC622 cathode are provided in Table A.4.

In Figure A.2, the comparison between the electrochemical measurements and the simulations with the extended p2D battery model is provided. A good agreement between the measured and simulation cells is reached. The parametrization could be improved by assembling the NMC622 cathode in a three-electrode setup to solely measure the potential of the cathode.

Table A.4: Redlich-Kister coefficients for the NMC622 OCP used in Chapter 5.

Coefficient J kmol^{-1}	NMC622 cathode J kmol^{-1}
$\mu_{\text{Li}^+}^0$	-402007.4
A_0	-73714.6
A_1	28842.2
A_2	6695.0
A_3	-2759.7
A_4	-22251.7
A_5	-11542.9
A_6	35612.7
A_7	3164.7
A_8	-29519.0

**Figure A.2:** Comparison of the measurements conducted with the NMC622 vs. lithium foil coin cell and the simulation results gained by the extended electrochemical model.

A.3 Data for Chapter 6

In Chapter 6, the model is based on the same half-cell and electrochemical measurements as described in Chapter 5, and the cell data provided in Appendix A.2.

In comparison to Chapter 5, the relevant kinetic parameters in Chapter 6 are estimated based on a fully homogeneous p2D battery model without the extension of the empiric surrogate models. This model is equal to the hybrid model with a homogeneous network at $L = 1$ implemented in Chapter 6. The detailed procedure for the estimation of the parameters can be taken from Chapter 4.

In Chapter 6, the classical Bruggeman relations are used for the transport processes and the reaction kinetics, and not the empiric surrogate equations (see Chapter 5). Consequently, the estimated parameters differ comparing Chapters 5 and 6. Only the differing parameters are listed in Table A.5. The other model parameters and structural parameters are provided in Table A.2.

Table A.5: Model parameters used for the classical homogeneous p2D model in Chapter 6. Additional parameters are listed in Table A.2 and A.4. The same NMC622 cathode was used as in Chapter 5.

Parameter	Symbol	Unit	Cathode
Tortuosity ^a	τ	-	3.16
Maximum capacity solid ^a	c_{Max}	mol m^{-3}	45859.20
Initial capacity solid ^a	c_0	mol m^{-3}	16432.40
Diffusion coefficient solid ^a	D_s	$\text{m}^2 \text{s}^{-1}$	1.13×10^{-14}
Electric bulk conductivity ^a	κ_s	S m^{-1}	0.0153
Transference number ^a	t_p	-	0.51
Reaction rate constant ^a	k	-	6.576×10^{-6}

^m measured by ZSW (Department of Production Research)

^a adjusted

^s set, from ref. [67]

^c concentration dependence, see eq. in [36]

The parameterized model can reproduce the conducted measurements (see Figure A.3). Discrepancies between the simulation and the measurements may result from the homogenization of the electrode microstructure and thus neglecting local effects. However, the model is rated accurately to represent the assembled battery.

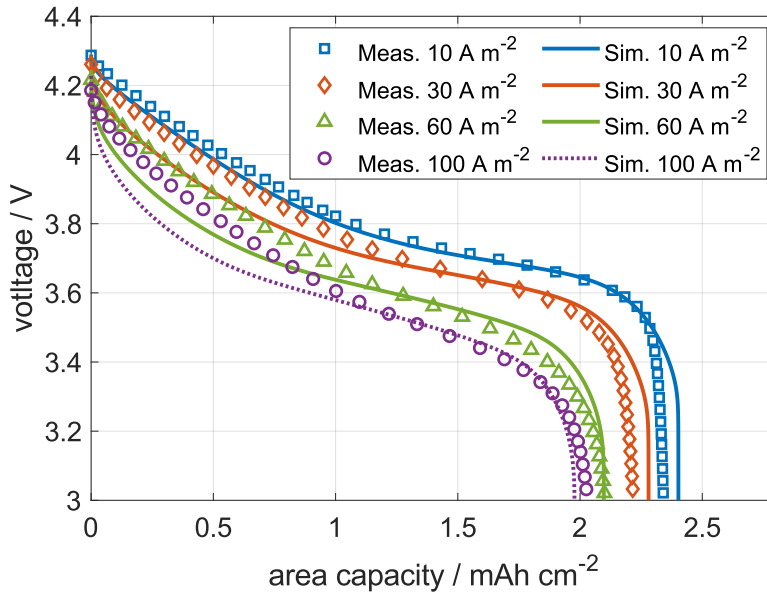


Figure A.3: Discharge curve of the parametrized electrochemical hybrid model with a homogeneous electrical network (solid lines) and the measurements of the NMC 622 vs. lithium reference anode (dotted).

B Estimation of Structural Data of Electrodes

In the production of lithium-ion batteries, the electrodes are often described and rated based on their mass loading and the coating density. The mass loading describes the weight of the coating applied on a defined area of the current collector. The coating density provides information regarding the compaction of the electrode coating, as the coating weight is related to its volume. In Chapter 5, electrodes with varying mass loading and coating density are analyzed with the electrochemical model. However, the input parameters for the model are the thickness and porosity of the cathode coating. Therefore, these quantities must be calculated. The calculation is based on simple geometric and mass fraction correlations. In the following the main equations are briefly introduced.

The coating density is defined as

$$\rho_C = \frac{m_C}{V_C}, \quad (\text{B.1})$$

with m_C as the mass of the coating and V_C the volume of the coating. The mass loading m_L is defined as

$$M_{\text{solid}} = \frac{m_C}{A_{\text{el}}}, \quad (\text{B.2})$$

where A_{el} is the area of the electrode. The mass of a single component m_i can be calculated based on the mass of the coating m_C and the weight fraction w_i of the component i (i.e., active material (AM), binder (B), carbon black (CB), conductive carbon (CC)) with

$$m_i = m_C \cdot w_i. \quad (\text{B.3})$$

Considering the density of the component ρ_i , the volume of the single component V_i in the electrode can be calculated with

$$V_i = \frac{m_i}{\rho_i}. \quad (\text{B.4})$$

The volume fraction of a component ε_i is the volume of a single component related on the volume of the electrode coating V_C

$$\varepsilon_i = \frac{V_i}{V_C}. \quad (\text{B.5})$$

Finally, the electrode thickness d_{el} can be calculated with the total mass of the electrode coating and the coating density

$$d_{\text{el}} = \frac{m_{\text{C}}}{A_{\text{el}} \cdot \rho_{\text{C}}}. \quad (\text{B.6})$$

The porosity of the electrode is defined as one minus the sum of the single volume fractions of the solid components

$$\varepsilon = 1 - \sum_{i=1}^n \varepsilon_i. \quad (\text{B.7})$$

Considering the mass loading, the weight fraction of the active material, and the specific gravimetric capacity of the active material, the specific areal capacity C of the electrode can be estimated by

$$C = m_{\text{L}} \cdot w_{\text{AM}} \cdot C_{\text{AM}}. \quad (\text{B.8})$$

Calculating the thickness, porosity and specific areal capacities for the cathodes in Chapter 5 was done by considering the structural and material parameters provided in Table B.1 and A.2. The parameters are based on an experimental cathode produced and analyzed by the ZSW in Ulm, Germany.

Table B.1: Structural and material parameters of the experimental NMC622 cathode composition. The carbon black and conductive carbon are summed up to solely represent the conductive additives by a single value. The cathode and the respective parameters were provided by the ZSW in Ulm, Germany.

Parameter	Symbol	Unit	Value
weight fraction of active material	w_{AM}	-	0.955
weight fraction of carbon black	w_{CB}	-	0.0225
weight fraction of conductive carbon	w_{CC}	-	0.0075
weight fraction of binder	w_{B}	-	0.015
density of active material	ρ_{AM}	g/cm^3	4.7
density of carbon black	ρ_{CB}	g/cm^3	2
density of conductive carbon	ρ_{CC}	g/cm^3	2.26
density of binder	ρ_{B}	g/cm^3	1.78
specific capacity of NMC622	C_{NMC622}	mAh/g	176

C Comparison of Degradation of Electrical Networks

In Chapter 6, the degradation of networks with a level of deagglomeration $L = 2$ was discussed. In Figure C.1, the impact of the level of deagglomeration is displayed for scale-free and random networks. It can be observed that changing from $L = 2$ to $L = 3$ has a minor impact on the degradation. The decrease in volumetric energy density shifts slightly to a smaller amount of removed edges. However, the difference is not significant, and due to faster calculation times and better visibility mainly $L = 2$ is discussed in Chapter 6.

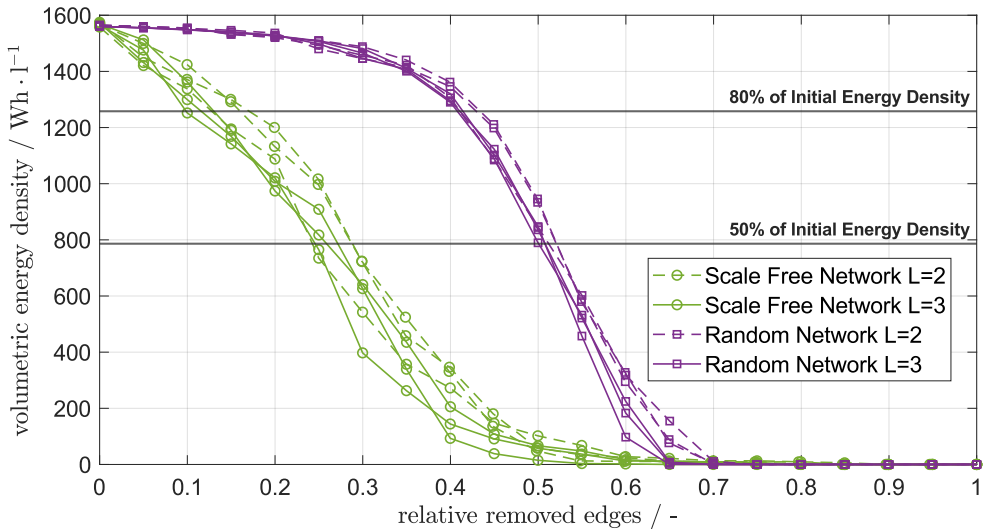


Figure C.1: Difference between degradation of scale-free and random networks with level of deagglomerations of $L = 2$ and $L = 3$.